



DOCTORAL THESIS IN INTERNATIONAL COTUTELLE AGREEMENT

PHD PROGRAM IN CHEMICAL AND ENVIRONMENTAL ENGINEERING

NEW TECHNOLOGY FOR HYDROGENATION PROCESSES IN THE ALIMENTARY INDUSTRY

Submitted by:

German Rodrigo Araujo Barahona

in fulfillment of the requirements for:

PhD degree by the

University of Valladolid (Spain)

and

Doctor of Science (Technology) degree by

Åbo Akademi University (Finland)

Supervised by:

Juan García Serna (University of Valladolid) Tapio Salmi (Åbo Akademi University)



New technology for hydrogenation processes in the alimentary industry

German Rodrigo Araujo Barahona





Johan Gadolin Process Chemistry Centre

Laboratory of Industrial Chemistry and Reaction Engineering
Faculty of Science and Engineering/Chemical Engineering
Åbo Akademi University
Turku/Åbo, Finland, 2025

"While you live, shine, have no grief at all. Life exists only for a short while and Time demands his due."

- Seikilos' epitaph.

PREFACE

They say it is not about the destination but the journey. In this doctoral journey, I have been fortunate to meet many wonderful people who made the achievement of this destination possible.

First, I would like to thank Professor Tapio Salmi for the opportunity to work with him. Tapio is not only a great scientist but also a remarkable person who generously shares his vast knowledge, kindness, and sense of humour with everyone around him. I feel privileged to have learned from him in all these aspects. I am also deeply grateful to my supervisor at the University of Valladolid, Professor Juan García Serna, for his constant guide and support since the very beginning, when I was still a master's student full of questions and dreams.

The experimental work of this thesis would not have been possible without the invaluable help of Docent Dr Kari Eränen. I am thankful not only for his exceptional ability to solve any problem in the lab, but also for everything I have learned from him through his patience and ingenuity. I would also like to thank Professor Dmitry Yu. Murzin for his wise advice on catalyst preparation characterization and kinetics; a visit to his office always brought new ideas and perspectives.

I would like to thank Dr Arne Reinsdorf and Dr Meike Roos from Evonik Operations GmbH for the very successful collaboration that is part of this thesis, for always being available, open, and insightful. I also thank Dr Nataliya Shcherban for the very fruitful collaboration on mesoporous molecular sieve catalysts.

I am extremely grateful to all the wonderful friends I have met along the way, who have made me feel at home despite being so far from my country: Federica, Luca, Christoph, Ole, Zuzana, Álvaro, Lilia, Wander, Matias, Francesco, Antonio, Emiliano, Mark, Pasi, Atte, Tommaso, Mouad, Chris, Ana, Olha, and Enrico. I am also deeply thankful to all the bachelor's and master's students who have contributed to this project over the years: Alberto, Maria, Angela, Miriam, Emilia, Carl, Michele, Guillaume, and Ethan.

Thanks also to those dear friends who accompany me through the distance. Marcela, thank you for being such an amazing friend to me, no matter the distance or the time. Olga, thank you for your friendship, for our constant messages, and for all the laughter we share today and in the future. Jackie, Iveth, Kenia, Alexanda, Karen and Maira, I hope our friendship is forever and that we meet soon again in El Salvador or anywhere else!

Y, por último, pero no por eso menos importante, gracias a mi familia. Ustedes son mi todo y les debo todo lo que soy y lo que tengo: a mi madre Haydeé y a mi padre German, por todo su amor y su lucha; a mi hermana Lilian, por ser la gran hermana que eres e inspirarme cada día a esforzarme con tu ejemplo; y a mis tíos Ruth y Carlos Humberto, muchas gracias por el apoyo incondicional y por siempre creer en mí. Con todo mi corazón, dedico esta tesis a mis sobrinitos Marco y Valeria, no puedo esperar para volver a jugar con ustedes.

A todos: mil gracias, tack så mycket, kiitos paljon!

—German.

ABSTRACT

This doctoral thesis explores novel catalytic technologies for the selective hydrogenation of biomass-derived sugars into sugar alcohols, molecules with high relevance for the alimentary industry. The work focuses on structured catalysts, particularly metallic solid foams, owing to their exceptional properties: high geometrical surface area, thin catalytic layers that suppress internal mass transfer resistance, and open structures that minimize pressure drop in packed-bed reactors. These features make solid foams promising alternatives to conventional catalyst particles and slurry systems, and suitable candidates for enabling the transition from semi-batch to continuous operation.

Three types of catalysts were investigated. First, ruthenium supported on mesoporous molecular sieves (MCM-41, SBA-15, and MCF) were synthesized as silicates and aluminosilicates and tested in xylose hydrogenation. The incorporation of aluminium improved ruthenium dispersion and activity, although stability was limited by metal leaching. Second, Raney-type solid nickel foams, with and without molybdenum promotion, were studied. While active and selective, the typical stability issues of nickel catalysts were mitigated by addition of molybdenum, which doubled the activity and enhanced resistance to deactivation. Third, Ru/C solid foams were synthesized via carbon coating of aluminium foams using poly(furfuryl alcohol) as precursor, with pore tailoring achieved through polyethylene glycol (8 kDa) addition. These catalysts exhibited excellent activity, selectivity, and reusability, making them suitable for both semi-batch and continuous operation.

Extensive kinetic experiments were performed in semi-batch reactors with monomeric sugars and mixtures (xylose, arabinose, galactose). Mechanistic models based on non-competitive and semi-competitive adsorption provided excellent agreement with experimental data. The competitiveness factor ($\alpha \approx 0.74$) of the semi-competitive adsorption model supported the predominance of sugar adsorption while leaving interstitial sites accessible for hydrogen, consistent with molecular size differences.

Continuous hydrogenation studies were conducted in a laboratory scale parallel screening reactor in trickle-bed regime. The effects of temperature, liquid flow rate, and concentration on conversion, selectivity, and space—time yield were quantified. Hydrodynamic measurements (residence-time distribution, liquid holdup) were coupled with kinetic modelling, demonstrating that gas—liquid and liquid—solid mass transfer resistances are of comparable magnitude under the low-interaction regime. At higher sugar concentrations and flow rates, liquid—solid hydrogen transfer emerged as the prevailing limitation.

Overall, this thesis demonstrates that structured foam catalysts overcome the internal diffusion and pressure drop limitations of conventional catalyst particles, while maintaining excellent activity and selectivity in sugar hydrogenation. The combined insights from material development, intrinsic kinetics, and transport modelling provide a robust framework for designing efficient three-phase catalytic systems. Future research should investigate reactor configurations and operating strategies that enhance wetting and interfacial mass transport, thereby unlocking the industrial potential of foambased catalysts in biomass valorization.

REFERAT

Denna doktorsavhandling utforskar nya katalytiska teknologier för selektiv hydrogenering av biomassebaserade sockerarter till sockeralkoholer, med hög relevans för livsmedelsindustrin. Arbetet fokuserar på strukturerade katalysatorer, särskilt metalliska skum, p.g.a. deras exceptionella egenskaper: stor geometrisk ytarea, tunt katalytiskt skikt som minimerar intern massöverföringsmotstånd samt öppna strukturer som minimerar tryckfallet i systemet. Dessa egenskaper gör fasta skum till lovande alternativ till konventionella katalysatorpartiklar och dispergerade system, och till lämpliga alternativ för att möjliggöra övergången från halvkontinuerlig till kontinuerlig drift.

Tre typer av katalysatorer undersöktes. Först syntetiserades och testades ruteniumstödda mesoporösa molekylsiktar (MCM-41, SBA-15 och MCF), silikater och aluminosilikater i hydrogenering av xylos. Inkorporering av aluminium förbättrade ruteniumdispersionen och aktiviteten, även om stabiliteten begränsades av urlakning. För det andra studerades Raney-typ nickelskum, med och utan molybden som promotor. Även om dessa katalysatorer var aktiva och selektiva, mildrades de typiska stabilitetsproblemen för nickelkatalysatorer genom tillsats av molybden, vilket fördubblade aktiviteten och ökade motståndskraften mot deaktivering. För det tredje syntetiserades Ru/C-skum genom beläggning av kol på aluminiumskum. Poly(furfurylalkohol) användes som kolkälla, där porstrukturen justerades genom tillsats av polyetylenglykol (8 kDa). Dessa katalysatorer uppvisade utmärkt aktivitet, selektivitet och återanvändbarhet, vilket gjorde dem lämpliga för både halvkontinuerlig och kontinuerlig drift.

Omfattande kinetiska experiment utfördes i halvkontinuerliga reaktorer med sockermonomerer och blandningar av dem (xylos, arabinos, galaktos). Mekanistiska kinetiska modeller baserade på ickekonkurrerande och semikonkurrerande adsorption gav utmärkt överensstämmelse med experimentella data. Konkurrensfaktorn ($\alpha \approx 0.74$) för den semikonkurrerande modellen bekräftade dominansen av sockeradsorption samtidigt som mellanliggande aktiva säten förblev tillgängliga för vätemolekyler, p.g.a skillnader i molekylstorlek.

Kontinuerliga hydrogeneringsstudier genomfördes i ett parallellt reaktorsystem i laboratorieskala under strömningsområdet trickleflöde. Effekterna av temperatur, vätskans strömningshastig och reaktantens koncentration på omsättning, selektivitet och produktivitet kvantifierades. Hydrodynamiska mätningar (uppehållstidfördelning, vätskeupptag) kombinerades med kinetisk modellering, vilket visade att gas-vätske- och vätske-fastfasöverföringsmotstånd var av jämförbar storleksordning i området av svag växelverkan. Vid högre sockerkoncentrationer var vätske-fastfasväteöverföring den dominerande begränsningen.

Sammanfattningsvis visar denna avhandling att strukturerade skumkatalysatorer kan övervinna de interna diffusions- och tryckfallsbegränsningarna hos konventionella katalysatorpartiklar, samtidigt som de bibehåller utmärkt aktivitet och selektivitet vid hydrogenering av sockerarter. De samlade insikterna från materialutveckling, verklig kinetik och modellering av massöverföring ger en solid grund för utformning av effektiva trefasiga katalytiska system. Framtida forskning bör inriktas på reaktorkonfigurationer och driftstrategier som förbättrar vätningsgraden och massöverföringen mellan faserna, och därmed skapar större industriell potential av skumbaserade katalysatorer för uppgradering av biomassa till värdefulla produkter.

RESUMEN

La presente tesis doctoral explora nuevas tecnologías catalíticas para la hidrogenación selectiva de azúcares derivados de biomasa en polialcoholes, moléculas con gran relevancia para la industria alimentaria. El trabajo se centra en catalizadores estructurados, en particular espumas metálicas sólidas, debido a sus propiedades excepcionales: alta superficie geométrica, capas catalíticas delgadas que minimizan la resistencia a la transferencia de materia interna y estructuras abiertas que reducen la caída de presión. Estas características los convierten en alternativas prometedoras a los pellets convencionales y a los sistemas en suspensión, así como en candidatos adecuados para facilitar la transición de la operación semicontinua hacia procesos continuos.

Se investigaron tres tipos de catalizadores. En primer lugar, se sintetizaron y evaluaron catalizadores de rutenio sobre tamices moleculares mesoporosos (MCM-41, SBA-15 y MCF), como silicatos y aluminosilicatos, en la hidrogenación de xilosa. La incorporación de aluminio mejoró la dispersión y la actividad del rutenio, aunque la estabilidad se vio limitada por lixiviación del metal. En segundo lugar, se estudiaron espumas sólidas de níquel tipo Raney, con y sin molibdeno como promotor. Aunque activas y selectivas, los problemas de estabilidad típicos de los catalizadores de tipo Raney Ni (lixiviación y bloqueo por adsorción de moléculas orgánicas) fueron observados, los cuales se mitigaron con la adición de molibdeno, lo que duplicó la actividad y mejoró la resistencia a la desactivación. En tercer lugar, se sintetizaron espumas sólidas de Ru/C mediante recubrimiento de espumas de Al con carbono, utilizando alcohol furfurílico polimerizado como precursor y con generación de poros a través de la adición de polietilenglicol (8 kDa). Estos catalizadores mostraron excelente actividad, selectividad y estabilidad, siendo adecuados tanto para operación semicontinua como continua.

Se realizaron extensos experimentos cinéticos en reactores semicontinuos con azúcares monoméricos y mezclas (xilosa, arabinosa, galactosa). Modelos mecanísticos basados en adsorción no competitiva y semicompetitiva describieron satisfactoriamente los datos experimentales. El factor de competitividad ($\alpha \approx 0.74$) del modelo semicompetitivo respaldó la predominancia de la adsorción de azúcares, dejando sitios intersticiales accesibles para el hidrógeno, en concordancia con las diferencias de tamaño molecular.

Los estudios en continuo se llevaron a cabo en un reactor de lechos paralelos a escala de laboratorio en régimen *trickle*. Se cuantificaron los efectos de la temperatura, el caudal líquido y la concentración sobre la conversión, la selectividad y la productividad espacio—tiempo. Las mediciones hidrodinámicas (tiempo de residencia, retención de líquido) se acoplaron al modelado cinético, demostrando que las resistencias de transferencia de masa gas—líquido y líquido—sólido son de magnitud comparable en el régimen de baja interacción. A mayores concentraciones y caudales de azúcar, la transferencia de hidrógeno líquido—sólido fue la limitación predominante.

En conjunto, esta tesis demuestra que los catalizadores en espuma estructurada superan las limitaciones de difusión interna y de caída de presión de los pellets catalíticos convencionales, manteniendo al mismo tiempo excelente actividad y selectividad en la hidrogenación de azúcares. Los conocimientos integrados sobre desarrollo de materiales, cinética intrínseca y modelado de transporte proporcionan un marco sólido para el diseño de sistemas catalíticos trifásicos eficientes. Futuras investigaciones deberán centrarse en configuraciones de reactor y estrategias de operación que mejoren el mojado y la transferencia interfacial, permitiendo así acceder al potencial industrial de las espumas catalíticas en la valorización de la biomasa.

LIST OF PUBLICATIONS

Published articles

- I. Araujo-Barahona, G., Eränen, K., Oña, J. P., Murzin, D.Y., García-Serna, J., & Salmi, T. (2022). Solid Foam Ru/C Catalysts for Sugar Hydrogenation to Sugar Alcohols—Preparation, Characterization, Activity, and Selectivity. Industrial & Engineering Chemistry Research, 61(7), 2734-2747. DOI: https://doi.org/10.1021/acs.iecr.1c04501.
- II. Araujo-Barahona, G., Eränen, K., Murzin, D.Y., García-Serna, J., & Salmi, T. (2022). Reaction mechanism and intrinsic kinetics of sugar hydrogenation to sugar alcohols on solid foam Ru/C catalysts–From arabinose and galactose to arabitol and galactitol. Chemical Engineering Science, 254, 117627.
 DOI: https://doi.org/10.1016/j.ces.2022.117627
- III. Araujo-Barahona, G., Goicoechea-Torres, A., Eränen, K., Latonen, R. M., Tirri, T., Smeds, A., Murzin, D.Y., García-Serna, J., & Salmi, T. (2023). Kinetic studies of solid foam catalysts for the production of sugar alcohols: Xylitol from biomass resources. Chemical Engineering Science, 281, 119130.
 DOI: https://doi.org/10.1016/j.ces.2023.119130.
- IV. Araujo-Barahona, G., Shcherban, N., Eränen, K., Kopa, I., Bezverkhyy, I., Martínez-Klimov, M., Vajglová, Z., Aho, A., García-Serna, J., Salmi, T., & Murzin, D. Y. (2024). Ruthenium supported on silicate and aluminosilicate mesoporous materials applied to selective sugar hydrogenation: Xylose to xylitol. Chemical Engineering Journal, 485, 150019. DOI: https://doi.org/10.1016/j.cej.2024.150019.
- V. Salmi, T., Araujo-Barahona, G., Najarnezhadmashhadi, A., Braz, C., Goicoechea-Torres, A., Ciaramella, M., Ares, M., Russo, V., García-Serna, J., Eränen, K., Wärnå, J., Matos, H. & Murzin, D. Y. (2024). Process Intensification via Structured Catalysts: Production of Sugar Alcohols. Chemie Ingenieur Technik, 96(12), 1642-1656.
 DOI: https://doi.org/10.1002/cite.202400087.
- VI. Araujo-Barahona, G., De Simone, M., Brunberg, C., Eränen, K., Reinsdorf, A., Roos, M., García-Serna, J., Russo, V., Murzin, D. Y., Salmi, T. Solid Raney-type Ni Foam Catalysts for Xylitol Production: Continuous and Batch Operation. Applied Catalysis A: General, 701, 120324. DOI: https://doi.org/10.1016/j.apcata.2025.120324.

Submitted articles (presented in Appendix I)

VII. **Araujo-Barahona, G.**, Ciaramella, M., Cavaliere, M., Bricault G, Eränen, K., García-Serna, J., Russo, V., Murzin, D. Y., Salmi, T. Kinetic and Transport Modelling of Continuous Xylose Hydrogenation on Ru/C Solid Foam Catalysts. (Submitted).

German R. Araujo Barahona's contributions to articles I-VII:

- Conceptualization, Methodology, Formal analysis, Writing original draft, Writing review & editing.
- II. Conceptualization, Methodology, Formal analysis, Software, Writing original draft,Writing review & editing.
- III. Conceptualization, Methodology, Formal analysis, Software, Writing original draft,Writing review & editing, Supervision.
- IV. Writing original draft, Investigation, Data curation.
- V. Writing original draft, Investigation
- VI. Writing original draft, Visualization, Validation, Methodology, Investigation, Funding acquisition, Formal analysis, Data curation, Conceptualization.
- VII. Conceptualization, Methodology, Formal analysis, Software, Writing original draft, Writing review & editing, Supervision.

Other publications related to the topic

- Salmi, T., **Araujo-Barahona, G**, Mastroianni, L. Strukturerade katalysatorer och reaktorelement revolution i kemisk teknologi, Annales Academiae Scientiarum Fennicae (2025) (in press)
- Araujo-Barahona, G., Salmi, T., García-Serna, J. (2025). Valorization of Banana Waste through Hydrothermal Extractions: Polyphenolic Compounds, Sugars and Sugar Alcohols. Book of Abstracts, ERASMUS + BIOP ESS-HPT 2025 "The European Summer School in High Pressure Technology" (Vol. 6).

CONFERENCE CONTRIBUTIONS

- I. Araujo-Barahona, G., Eränen, K., García-Serna, J., Murzin, D. Y. Solid Foam Catalysts A Clean and Green Pathway to the Production of Sweet Sugar Alcohols (Oral Presentation).
 5th International Symposium on Green Chemistry, La Rochelle, France, 2022.
- II. Araujo-Barahona, G., Goicoechea-Torres, A., Eränen, K., Murzin, D. Y., García-Serna, J., Salmi, T. New Development of Solid Foam Catalysts for the Production of Sugar Alcohols (Oral Presentation). 18th International Conference on Renewable Resources and Biorefineries, Bruges, Belgium, 2022.
- III. Araujo-Barahona, G., Goicoechea-Torres, A., Eränen, K., García-Serna, J., Murzin, D. Y., Salmi, T. Ru/C Solid Foam Catalysts for Production of Sugar Alcohols: From Catalyst Development to Kinetic Modelling (Poster Presentation). 15th European Congress on Catalysis, Prague, Czech Republic, 2023.
- IV. Araujo-Barahona, G., Goicoechea-Torres, A., Eränen, K., García-Serna, J., Murzin, D. Y., Salmi, T. Ru/C Solid Foam Catalyst for Hydrogenation of Sugars: Catalyst Development and Kinetic Study (Oral Presentation). 11th World Congress of Chemical Engineering (WCCE11), Buenos Aires, Argentina, 2023.
- V. Araujo-Barahona, G., Shcherban, N., Barakov, R., Kopa, I., Martinez-Klimov, M. Ru, Ni and Pd Catalysts Deposited onto Zeolites and Mesoporous Molecular Sieves for Hydrogenation and Hydrocracking of Biomass-Derived Compounds (Oral Presentation).
 28th North American Catalysis Society Meeting, Providence, Rhode Island, United States, 2023.
- VI. Araujo-Barahona, G., Goicoechea-Torres, A., Ciaramella, M., Cavaliere, M., Eränen, K., Murzin, D. Y., García-Serna, J., Russo, V., Salmi, T. Solid Foam Catalysts for Hydrogenation of Sugars (Oral Presentation). 50th International Conference of the Slovak Society of Chemical Engineers, Tatra Mountains, Slovakia, 2024.
- VII. Araujo-Barahona, G., Goicoechea-Torres, A., Ciaramella, M., Cavaliere, M., Eränen, K., Murzin, D. Y., García-Serna, J., Russo, V., Salmi, T. Sugar Hydrogenation on Solid Foam Catalysts: Catalyst Development and Kinetic Studies From Batch to Continuous Operation (Poster Presentation). 18th International Congress on Catalysis, Lyon, France, 2024.
- VIII. Araujo-Barahona, G., Goicoechea-Torres, A., Ciaramella, M., Cavaliere, M., Eränen, K., Murzin, D. Y., García-Serna, J., Russo, V., Salmi, T. Solid Foam Catalysts Applied to Sugar Hydrogenation: Towards Continuous Production of Sugar Alcohols (Oral Presentation). ISCRE 28 International Symposium on Chemical Reaction Engineering, Turku, Finland, 2024.

- IX. Araujo-Barahona, G., Goicoechea-Torres, A., Ciaramella, M., Cavaliere, M., Eränen, K., Murzin, D. Y., García-Serna, J., Salmi, T. Solid Foam Catalysts: Paving the Way for Efficient Sugar Alcohol Production (Keynote Presentation). 27th International Congress of Chemical and Process Engineering, Prague, Czech Republic, 2024.
- X. Araujo-Barahona, G., Eränen, K., Ciaramella, M., García-Serna, J., Russo, V., Murzin, D. Y., Salmi, T. Development of a Parallel Screening Gas-Liquid-Solid Reactor System for Kinetic, Mass Transfer, and Flow Studies (Oral Presentation). 16th International Conference on Gas-Liquid and Gas-Liquid-Solid Reactor Engineering, Dresden, Germany, 2024.
- XI. Araujo-Barahona, G., Goicoechea-Torres, A., Ciaramella, M., Cavaliere, M., Eränen, K., Murzin, D. Y., García-Serna, J., Russo, V., Salmi, T. Solid Foam Catalyst for Three-Phase Sugar Hydrogenation: Semi-Batch and Continuous Operation (Oral Presentation). 12th International Symposium on Catalysis in Multiphase Reactors and the 11th International Symposium on Multifunctional Reactors (CAMURE12-ISMR11), Ghent, Belgium, 2024.
- XII. Araujo-Barahona, G., Goicoechea-Torres, A., Ciaramella, M., Cavaliere, M., Eränen, K., Murzin, D. Y., García-Serna, J., Russo, V., Salmi, T. Ru/C Foam Catalysts: Towards Continuous Production of Sugar Alcohols (Oral Presentation). 5th Ibero-American Congress on Biorefineries, Jaén, Spain, 2024.
- XIII. Araujo-Barahona, G., Ciaramella, M., Eränen, K., Murzin, D. Y., Russo, V., García-Serna,
 J., Salmi, T. Continuous Production of Xylitol on Solid Foam Catalysts (Oral Presentation).
 29th Biennial ORCS Meeting, Myrtle Beach, North Carolina, United States, 2025.
- XIV. Araujo-Barahona, G., Hachhach, M., Mastroianni, L., Simakova, I., García-Serna, J., Russo, V., Di Serio, M., Murzin, D., Wärnå, J., Eränen, K., Salmi, T. Catalytic hydrogenation and oxidation of monomeric sugars: the great valorisation of hemicelluloses with the aid of structured catalysts (Oral presentation). International Symposium on Green Chemistry, La Rochelle, France, 2025.
- XV. Araujo-Barahona, G., García-Serna, J., Salmi, T. From waste to wealth: Hydrothermal biorefining of banana residues (Oral presentation). International Conference on Renewable Resources & Biorefineries, Turku, Finland, 2025.

TABLE OF CONTENTS

PREFACE	V
ABSTRACT	vii
REFERAT	ix
RESUMEN	xi
LIST OF PUBLICATIONS	xiii
1. INTRODUCTION	19
1.1. The biorefinery concept and sugar alcohols	19
1.2. Solid foam catalysts	21
1.3. Objective and research strategy	22
2. EXPERIMENTAL (Articles I-VI and Appendix I)	23
2.1. Chemicals and materials	23
2.2. Synthesis of Ru/mesoporous molecular sieves catalysts	23
2.3. Synthesis of Ru/C solid foam catalysts	24
2.4. Catalyst and material characterization techniques	25
2.5. Kinetic experiments in semi-batch operation	27
2.6. Continuous hydrogenation experiments	28
2.7. Residence Time Distribution (RTD) experiments	30
2.8. Liquid holdup experiments	31
3. RESULTS AND DISCUSSION	33
3.1. Ru on mesoporous molecular sieves (Article IV)	34
3.1.1. Primary catalyst characterization	34
3.1.2. Catalyst screening	38
3.1.3. Process parameters and stability	39
3.2. Raney-type solid foam catalysts (Article VI)	41

3.2.1. Semi-batch experiments and catalyst characterization	41
3.2.2. Deactivation modelling	46
3.2.3. Continuous hydrogenation experiments	51
3.3. Ru/C solid foam catalysts (Articles I–III and Appendix I)	55
3.3.1. Catalyst synthesis results	55
3.3.2. Semi-batch experiment results	63
3.3.3. Intrinsic kinetic modelling	65
3.3.4. Modelling of sugar mixtures	72
3.3.5. Continuous xylose hydrogenation	75
3.3.6. Modelling of continuous xylose hydrogenation	79
4. CONCLUSIONS AND FUTURE PERSPECTIVES	94
REFERENCES	96
NOTATION	106
ACKNOWLEDGMENTS	110

1. INTRODUCTION

1.1. The biorefinery concept and sugar alcohols

The transition towards a sustainable society relies on the development of efficient processes that minimize energy consumption and waste generation, while simultaneously enabling the transformation of residues into valuable resources such as fuels, chemicals, and food ingredients [1–3]. Lignocellulosic biomass, the most abundant renewable material on Earth, consists of 40–50 wt.% cellulose (a glucose-based polymer linked by β -1,4-glycosidic bonds), 16–33 wt.% hemicelluloses (heteropolymers containing sugar monomers such as arabinose, galactose, glucose, mannose, and xylose), and 15–30 wt.% lignin (a cross-linked aromatic polymer composed of coniferyl, coumaryl, and sinapyl alcohols) [4–6] (Figure 1). Hemicelluloses are particularly attractive because they yield a wide variety of sugar monomers upon hydrolysis and separation, which can serve as building blocks for a broad portfolio of value-added products [7, 8].

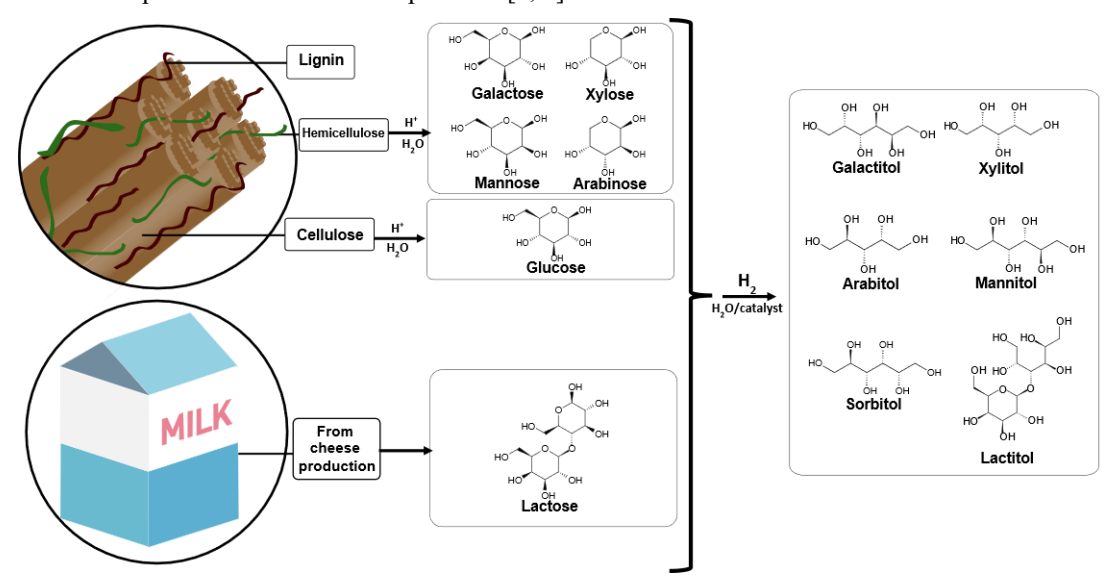


Figure 1. Production of sugar alcohols from lignocellulosic biomass and cheese by-products via catalytic hydrogenation.

Sugar alcohols represent an emblematic case of biomass valorisation, obtained by selective hydrogenation of monomeric sugars (glucose, xylose, galactose, arabinose) [9] or from lactose streams generated as by-products of cheese production, yielding lactitol [10,11]. Figure 1 illustrates these routes.

Polyols such as sorbitol, mannitol, arabitol, galactitol, lactitol, and xylitol are widely applied in the food, pharmaceutical, and cosmetic industries. Their sweetening capacity combined with low caloric content has made them attractive alternatives to sucrose [12]. Furthermore, health-promoting properties—anticaries, antioxidant, and anti-inflammatory—have consolidated their market demand. Xylitol stands out due to its relevance in oral health [13], osteoporosis prevention [14], and even respiratory therapies [15]. The global market of sugar alcohols exceeded 3.6 billion euros in 2019 and is projected to approach 6 billion euros by 2027, with an annual growth rate of approximately 5%.

Conventionally, sugar alcohols are manufactured via acid hydrolysis of hemicellulose to monomeric sugars, followed by separation and purification, and subsequent catalytic hydrogenation in semibatch reactors using finely dispersed Raney-type nickel catalysts [16]. Despite being industrially established, this process suffers from drawbacks: Raney Ni is pyrophoric, prone to deactivation [17,18] and in its powdered form restricts operation to semi-batch mode due to elevated pressure drop, complicating integration with continuous downstream processes.

Alternative catalytic systems have thus been extensively investigated. Among conventional metals, ruthenium has emerged as the most promising one, showing the highest intrinsic activity for sugar hydrogenation of the conventional metals used in heterogeneous catalysis (Ru > Ni > Rh > Pd) [19]. Numerous studies confirm that Ru catalysts can deliver high activity, selectivity, and stability under typical sugar hydrogenation conditions [20]. However, the choice of support is crucial, as it determines the dispersion and electronic environment of Ru nanoparticles and the accessibility of relatively large sugar molecules in aqueous solution.

1.2. Solid foam catalysts

In heterogeneous catalysis, a long-standing dilemma persists. Slurry reactors with finely dispersed catalysts maximize effectiveness factors and allow intrinsic kinetic studies, but they are limited to batch operation and require costly downstream separation. In contrast, packed-bed reactors enable continuous operation but suffer from intraparticle diffusion limitations and substantial pressure drops, particularly when small catalyst particles are used [21].

Structured catalysts such as fibers, monoliths, open-cell foams, and 3D-printed structures meet the needs in the development of new catalytic technologies for continuous operation. Solid foam catalyst stands out among structure catalysts. Metallic open-cell foams combine large geometric surface areas $(700-7000~\text{m}^2\cdot\text{m}^{-3}$ depending on porosity), and thin catalyst layers (<100 μ m) suppressing the internal diffusion resistance in the catalyst pores, while the open structure minimizes pressure drop [22]. In addition, metallic foams exhibit excellent mechanical stability and a tortuous flow path that enhances heat transfer in three-phase systems [23]. As a result, foam-based catalytic systems integrate the benefits of both slurry and packed-bed technologies.

A key limitation of metallic foams is their intrinsically low surface area for active phase deposition. This drawback can be overcome by applying suitable coatings that enhance the available surface for anchoring the catalytic material [24]. In this context, furfuryl alcohol (FA) has been widely investigated as a carbon precursor for structured catalysts [25–29]. The use of furfuryl alcohol (FA) offers several advantages, including a relatively high carbon yield (approximately 50%), high reactivity toward the formation of resinous carbon compounds, and its origin from renewable biomass. [30].

1.3. Objective and research strategy

The general objective of this doctoral thesis is to develop and evaluate novel catalysts, particularly solid foams, for the selective hydrogenation of biomass-derived sugars into sugar alcohols. The work combines intrinsic kinetic studies and transport modelling under both semi-batch and continuous operation, with the aim of providing a scientific and technological framework that supports the transition from conventional semi-batch processes toward efficient and scalable continuous hydrogenation processes for the alimentary industry.

The research strategy is illustrated in Figure 2. The strategy was structured around three main pillars:

- Catalyst synthesis and characterization to establish structure-property relationships. Three
 types of catalytic systems were investigated: Ru catalysts supported on mesoporous molecular
 sieves (MCM-41, SBA-15, MCF), Raney-type solid nickel foams (both unpromoted and Mopromoted), and Ru/C solid foam catalysts.
- Intrinsic kinetic studies to evaluate the activity and stability of the catalysts. These studies
 involved semi-batch hydrogenation experiments, kinetic modelling, and deactivation
 analysis.
- 3. Mass transport and reactor modelling to assess catalytic performance under continuous operation. A combination of residence time distribution (RTD) measurements, liquid hold-up experiments, and mass transport and reaction kinetic modelling was used to evaluate continuous sugar hydrogenation.

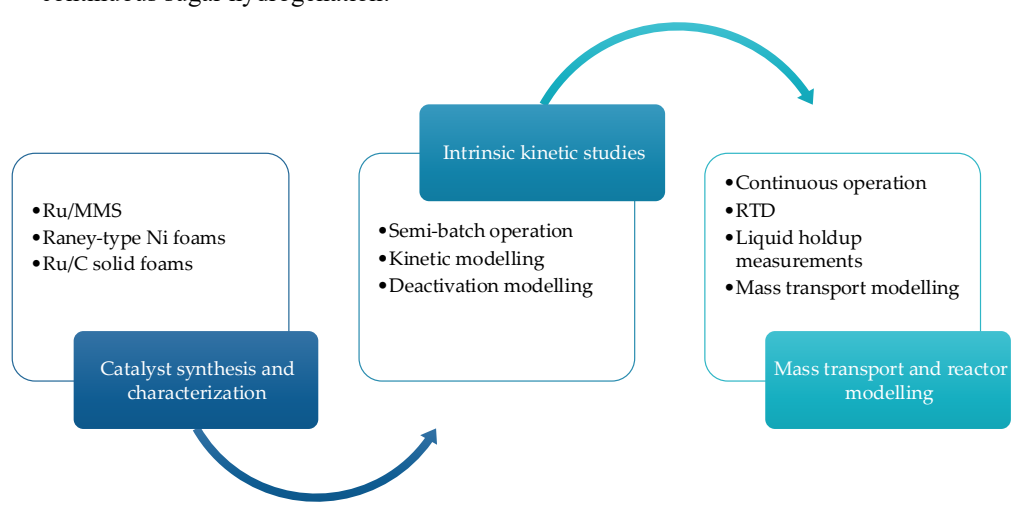


Figure 2. Research structure and strategy.

2. EXPERIMENTAL (Articles I-VI and Appendix I)

2.1. Chemicals and materials

The chemicals used in this work are the following: D-xylose (≥99.0%, Sigma-Aldrich), xylitol (≥99.0%, Sigma-Aldrich), D-arabitol (99.0%, Sigma-Aldrich), meso-erythritol (≥99.0%, Sigma-Aldrich), D-xylulose (≥95%, Sigma-Aldrich), L-arabinose (≥99.0%, Sigma-Aldrich), D-galactose (≥99.0%, Sigma-Aldrich), furfuryl alcohol (98.0%, Sigma-Aldrich), oxalic acid dihydrate (95.0%, Sigma-Aldrich), sulfuric acid (96 wt%, Sigma-Aldrich), nitric acid (65 wt%, Sigma-Aldrich), hydrochloric acid (35 wt%, VWR), ammonium hydroxide solution (25 wt%, Supelco), ammonium fluoride (≥98.0%, Sigma-Aldrich), aluminium sulfate hexadecahydrate (98 wt%, Fluka), aluminium isopropoxide (≥98.0%, Sigma-Aldrich), tetraethyl orthosilicate (≥99.0%, Sigma-Aldrich), cetyltrimethylammonium chloride (CTACl, 25 wt% in water, Sigma-Aldrich), Pluronic P-123 (98.0%, (Sigma-Aldrich), 1,3,5-trimethylbenzene Sigma-Aldrich), N.Obis(trimethylsilyl)trifluoroacetamide (BSTFA, Sigma-Aldrich), trimethylsilyl chloride (TMCS, Sigma-Aldrich), poly(ethylene glycol) (8 kDa, Sigma-Aldrich), quartz sand (SiO₂, ≥ 99.99 %, Sigma-Aldrich), ruthenium(III) nitrosyl nitrate solution (1.4 wt.% Ru, Sigma-Aldrich), ruthenium(III) chloride hydrate (ReagentPlus®, Merck), and commercial Ru/C catalyst (6 wt% Ru). Aluminium foams (40 PPI or 93% porosity) were purchased from Goodfellow Cambridge Ltd. Two solid Ni foam catalysts were provided by Evonik: Metalyst® MC 911, a Raney-type nickel foam catalyst containing 80-95 % Ni (hereinafter named Ev-F-Ni), and Metalyst® MC 981, a Raney-type nickel foam catalyst containing 80-95 % Ni and promoted with molybdenum (hereinafter named Ev-F-NiMo).

2.2. Synthesis of Ru/mesoporous molecular sieves catalysts

To investigate the influence of the support on the performance of Ru-based catalysts for sugar hydrogenation, a series of catalysts were prepared by depositing Ru nanoparticles onto silicate and aluminosilicate mesoporous molecular sieves (MMS): MCM-41, SBA-15 and MCF. The supports were synthesized via sol–gel methods using surfactant templates (CTACl or Pluronic P-123) followed by hydrothermal treatment at 100 °C (24–72 h), filtration, drying (100 °C, overnight), and calcination at 550 °C for 5 h. The aluminosilicate analogues were obtained by introducing aluminum isopropoxide during the synthesis (Si/Al = 50), in some cases combined with pH adjustment to 7.5 before a second hydrothermal step. The final solids were isolated as well-ordered mesoporous

powders with high surface area. Ruthenium nanoparticles were then incorporated by wet impregnation with RuCl₃ solution (nominal loading 2 wt.%), followed by rotary evaporation, drying at 60–120 °C, and reduction under H₂ at 350 °C for 3 h.

2.3. Synthesis of Ru/C solid foam catalysts

Solid foam catalysts were synthesised through the sequence of steps illustrated in Figure 3, comprising cutting, anodic oxidation pretreatment, carbon coating, acid functionalization, ruthenium incorporation, and catalyst reduction.

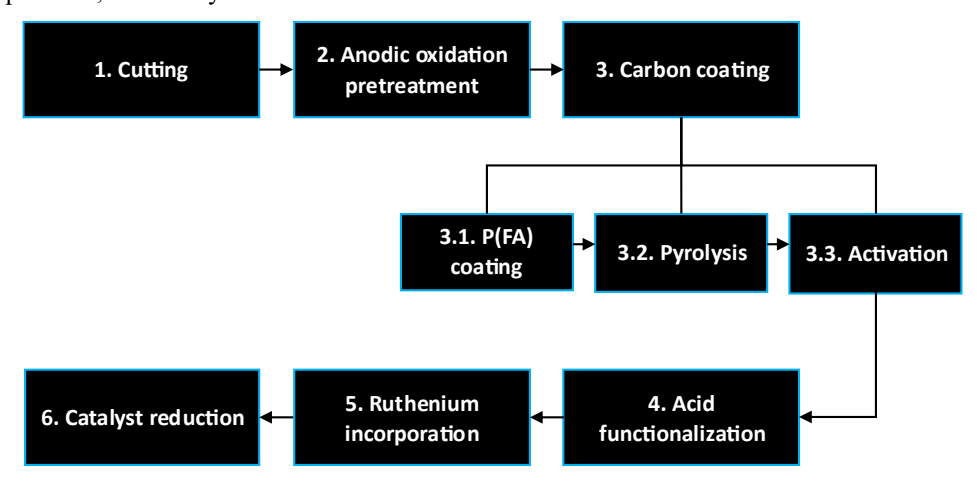


Figure 3. Overview of the preparation process of the Ru/C solid foam catalysts.

Cylindrical pieces, 33 mm in length and with diameters of 11 or 8 mm, were cut from an aluminium foam sheet (40 pore per inch, PPI) using a diamond hole saw. The foams were then sonicated for 15 min in deionised water and 15 min in acetone and subsequently dried for 2 h at 70 °C followed by overnight drying at room temperature.

To improve carbon adhesion, the aluminium foams were subjected to anodic oxidation to form a thin oxide layer. A clean foam was attached to a platinum strip and connected as the anode, while a rectangular aluminium plate (4 × 9 cm, immersed area 18 cm²) served as the cathode, with both electrodes immersed 2.5 cm apart in the electrolyte. The electrolyte contained 100 mL of 1.6 M sulfuric acid and 60 g·L⁻¹ aluminium sulphate hexadecahydrate, which controlled aluminium dissolution during anodization [31, 32]. The solution was kept under stirring at 40 °C using a jacketed vessel connected to a thermostat. A constant current of 2 A was applied for 1 h, and the voltage was monitored with the GPES software. The foams were then rinsed with deionised water, dried at 70 °C for 30 min, and calcined at 600 °C for 4 h.

A thin carbon coating was deposited on the aluminium foam structures by polymerization of furfuryl alcohol followed by pyrolysis. Three anodized foams were fixed to a cross-blade stirrer shaft and immersed in a mixture of 136.2 g furfuryl alcohol, 0.84 g oxalic acid dihydrate, and 16.7 g distilled water. The foams were rotated at 200 rpm while the temperature was raised at 2 °C·min⁻¹ to 110 °C. Polymer curing was maintained for approximately one hour in the range of 110–130 °C by manual adjustment of the heating profile. Polyethylene glycol (M = 8 kDa, 0–15 wt.%) was added during the final curing stage (ca. 50 min) as a pore-forming precursor to generate mesoporosity during pyrolysis and activation. The excess polymer on the foams was removed by rotating them for five minutes at 1000 rpm. Subsequent polymer pyrolysis was carried out at 550 °C in a furnace with a nitrogen flow of 2 L·min⁻¹, NTP for five hours, followed by an activation step at 380 °C under an airflow of 1 L·min⁻¹, NTP for two hours.

The obtained carbon-coated foams were immersed in a 5 wt.% nitric acid solution for two hours to generate oxygen-containing surface groups, after which they were washed and oven-dried for two hours at 70 °C. Ruthenium incorporation was performed by incipient wetness impregnation with a 0.6 mol·L⁻¹ solution of Ru(III) nitrosyl nitrate, dripped stepwise (≈0.4 g per step) onto the carbon surface. Each impregnation step was followed by drying at 110 °C for 24 h. Finally, the catalysts were reduced under a hydrogen stream (100 mL·min⁻¹, NTP) at 300 °C for 5 h with a heating ramp of 3 °C·min⁻¹.

2.4. Catalyst and material characterization techniques

Thermogravimetric analysis (TGA) was used to study the decomposition of poly(furfuryl alcohol) mixed with polyethylene glycol (PEG), precursors of the carbon coating in Ru/C solid foam catalyst synthesis, by heating 20 mg of sample from 20 to 1000 °C at 5 °C·min⁻¹ under nitrogen in a SDT 650 analyser to determine the carbon yield and the role of the pore-forming agent. TGA was also applied to fresh and spent Raney-type foam catalysts used in semi-batch hydrogenation experiments. After drying at 100 °C for 1 h, the samples were analysed under nitrogen from 100 to 800 °C at 5 °C·min⁻¹ to assess the presence of organic deposits.

Scanning electron microscopy (Zeiss Leo Gemini 1530) coupled with energy-dispersive X-ray analysis (LEOGemini 1530 with a Thermo Scientific Ultradry Silicon Drift Detector) was used to study the morphology and surface composition of the different materials used in this work. Transmission electron microscopy (TEM, JEM-1400 Plus) was employed to determine the Ru nanoparticle size distribution of the synthesized catalysts. The micrographs were analysed using

Image J software. For a statistically reliable distribution, between 500 and 1000 nanoparticles were counted for each sample.

Inductively Coupled Plasma Optical Emission Spectroscopy (ICP-OES; PerkinElmer Optima 5300 DV) was employed to quantify the metallic content of the synthesized catalysts and to monitor Ru or Ni leaching under reaction conditions. Solid samples (≈0.1 g) were digested in a 1:1 mixture of sulfuric acid (96 wt.%) and nitric acid (65 wt.%) prior to spectrometric analysis.

Temperature-Programmed Reduction (TPR) measurements were carried out using a Microtrac MRB Catalyst Analyzer Belcat II to determine the reduction conditions necessary for the synthesized catalysts and to evaluate the metal–support interactions in Ru supported on MMS. The measurements were performed from 30 to 800 °C at a heating rate of 10 °C·min⁻¹ under a 5.24 mol% H₂/Ar flow (30 cm³·min⁻¹, STP). In the same equipment, pulse hydrogen chemisorption was employed to determine the Ni surface area of fresh and spent Raney-type foam catalysts. Approximately 60 mg of sample were placed in the furnace and dried at 110 °C for 3 h. Hydrogen adsorption was then performed at 50 °C using 50 cm³·min⁻¹, STP of Ar as carrier gas. A mixture of 5.24 mol % H₂ in Ar was introduced from a calibrated sample loop (0.9950 cm³, STP) via a 6/2-way valve, with pulses injected every 200 s (10 injections per sample). The exhaust gas was passed through a molecular sieve bed to remove moisture before entering the thermal conductivity detector (TCD). The areas of the first three pulses were used to calculate the amount of adsorbed hydrogen, while the last five pulses served for calibration.

Nitrogen physisorption measurements at 77 K were performed using a Micromeritics 3Flex-3500 sorptometer to determine the specific surface area and pore size distribution of the studied materials. Prior to analysis, the samples were outgassed at 300 °C for 24 h.

X-ray Photoelectron Spectroscopy (XPS) was employed to analyse the surface chemical states of the catalysts. Samples were dried under nitrogen in a glove box and transferred to the instrument using a Thermo Scientific transfer vessel to avoid air exposure (Ni foam catalysts). Measurements were performed with a Thermo Scientific Nexsa G2 spectrometer equipped with a monochromated Al K α source, maintaining the analysis chamber pressure below 2×10^{-9} mbar. To remove possible surface oxides formed during transfer, a mild ion beam etching (6000 eV/300 Ar cluster, 30 s) was applied. The C 1s peak at 284.8 eV (C-C) was used as the binding energy reference. The spectra

were acquired for Ni 2p/3p, Ru 3d, Al 2p, and Mo 3p regions, and deconvoluted with XPS PEAK 41 software using literature binding energy values and characteristic reference peaks.

2.5. Kinetic experiments in semi-batch operation

Kinetic experiments in semi-batch mode were carried out in a laboratory-scale reactor (BR, Parr 4561, nominal volume 300 mL), equipped with baffles, a sampling line with a sintered filter (7 μ m), a heating jacket, temperature and stirring controllers (Parr 4843), a cooling coil, a pressure display module (Parr 4843), and a preheating chamber (BR-PC), as illustrated in Figure 4(a). Prior to each experiment, the reactor was purged with argon and subsequently with hydrogen, and the catalyst was reduced in situ in hydrogen at 120 °C and 5 bar for two hours. A sugar solution (130 mL) in deionized water was saturated with hydrogen in the preheating chamber at the selected temperature and pressure before being injected into the reactor at t = 0 min. This procedure enabled the reaction to start directly under the desired experimental conditions. Hydrogen was constantly fed to the reactor to maintain constant pressure conditions during the experiments.

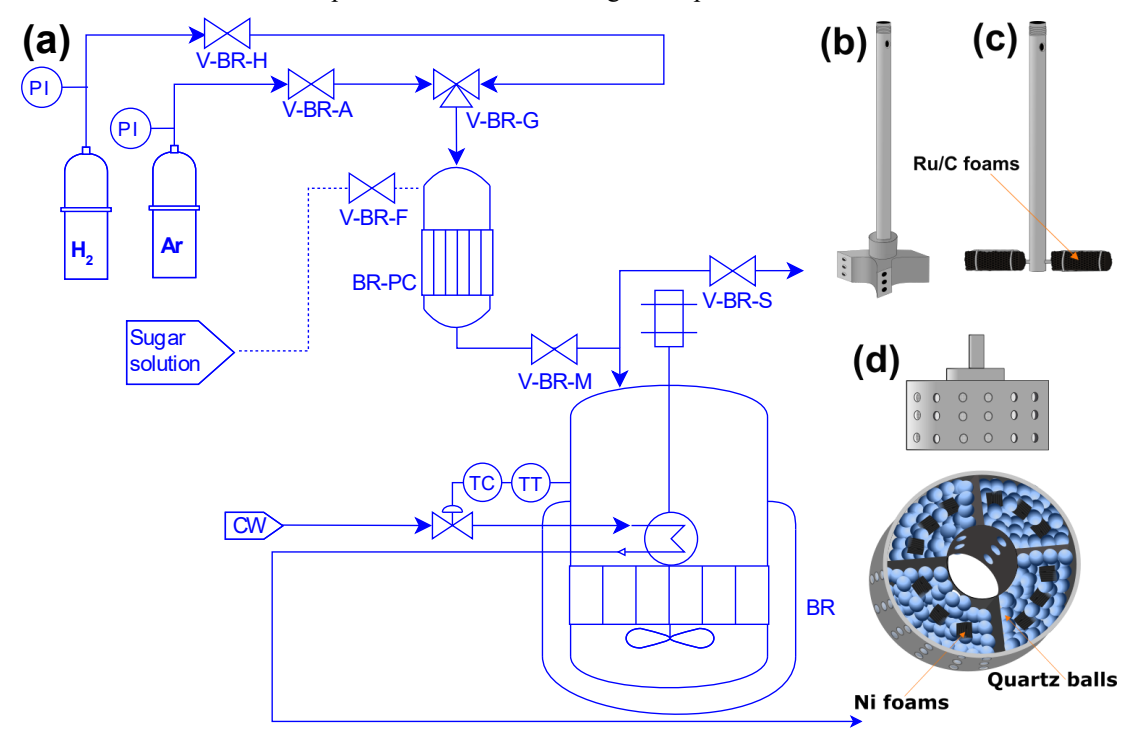


Figure 4. Configurations for semi-batch experiments: (a) Reactor setup; (b) gas-entrainment impeller; (c) Ru/C foam attached to stirrer shaft of the autoclave reactor, (d) SpinChem® rotating bed loaded with Ni foam catalysts.

The catalysts tested in this configuration comprised Ru-supported silicate and aluminosilicate powders (Ru/Al-MCM-41, Ru/Al-MCF, Ru/Al-Si-SBA-15, Ru/Si-SBA-15, Ru/Si-MCM-41), a commercial Ru/C powder catalyst, two Raney-type Ni foams—Ev-F-Ni (Metalyst® MC 911, 80–95 % Ni) and Ev-F-NiMo (Metalyst® MC 981, 80–95 % Ni, Mo-promoted)—as well as a homemade Ru/C solid foam (Ru/FC). For powder catalysts, a gas-entrainment impeller was employed (Figure 4(b)). In the case of the Ru/C solid foam, two foam pieces were fixed to the stirrer shaft, replacing the conventional impeller and acting as both catalyst and stirrer (Figure 4(c)). The Raney-type foams (4 × 4 × 1.9 mm) were mounted in a SpinChem® rotating bed filled with inert quartz balls to fix them (Figure 4(d)).

Catalyst screening of the Ru/MMS series was carried out against a commercial Ru/C benchmark at 100 °C and 40 bar. A systematic study of temperature (75–100 °C) and pressure (10–50 bar) was also performed for the best catalyst in the series. The stability of the Raney-type solid foams was evaluated by repeating hydrogenation experiments at 90 °C and 30 bar. Finally, a detailed kinetic study was conducted with the most active Ru/C solid foam catalyst over a temperature range of 60–120 °C, hydrogen pressures between 20 and 60 bar, and initial xylose concentrations of 0.065–0.13 M.

2.6. Continuous hydrogenation experiments

Kinetic experiments were carried out in a laboratory-scale parallel screening reactor displayed in Figure 5(a). The reactor system consisted of six tubular beds (R1–R6; L = 23.1 cm, i.d. = 1 cm), each equipped with independent heating jackets, gas flow controllers, and HPLC pumps. Gas and liquid flowed co-currently through the beds, and samples were withdrawn via a small sampling loop (L = 2 cm, i.d. = 0.15 cm). The reactor effluents were cooled in heat exchangers (E-X) and collected in 1 L vessels (C-X). The pressure of the system was controlled with a backpressure valve installed on a shared outlet line; a 0.5 L overflow vessel (OC-1) protected the regulator from liquid carryover.

Each bed was packed as shown in Figure 5(b), an initial layer of quartz sand to improve uniform gas-liquid distribution, followed by an uncoated aluminium foam to stabilize the velocity profile, and finally three Ru/C or Raney-type foam catalysts. A thermocouple embedded in the last quartz was in contact with the last foam catalyst.

A standard hydrogenation experiment was performed in the following way.

- The reactor was filled with hydrogen with a gas flow rate of 100 mL⋅min⁻¹, NTP up to a
 pressure of 20 bar.
- The catalysts were reduced in-situ at 120 °C for 2 h.
- The system temperature adjusted to the desired setpoint.
- The sugar solution fed at the target liquid flow rate, and the samples were withdrawn every ~30 min for 5 h.
- After the experiment, the reactor was stepwise depressurized and flushed with deionized water (1.00 mL·min⁻¹) under 1 bar Ar (50 mL·min⁻¹). The catalysts were stored under 1 bar Ar to prevent oxidation.
- HPLC analysis (HP 1100, RI detector) was performed with a Rezex RCM-Monosaccharide Ca²⁺ column at 70 °C using 1.2 mM CaSO₄ as the mobile phase (0.6 mL·min⁻¹, 5 μL injection volume).

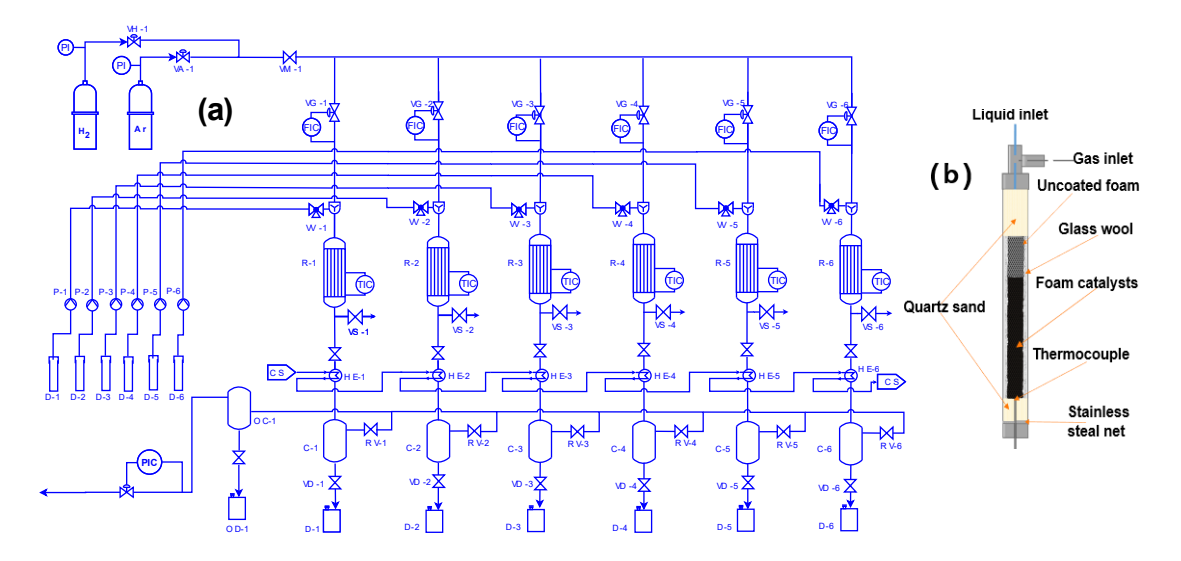


Figure 5. Parallel screening reactor system: (a) flow diagram and (b) packing of an individual reactor with solid foam catalysts.

2.7. Residence Time Distribution (RTD) experiments

The hydrodynamics of the packed bed was characterized through step-response experiments at liquid flow rates between 0.25 and 1.00 mL·min⁻¹. The reactor was first pressurized with hydrogen (100 mL·min⁻¹, NTP) to 20 bar and heated to 120 °C. Water was pumped at the selected flow rate and allowed to stabilize for 1 h. Subsequently, the feed was switched to an inert tracer solution, consisting of 0.13 M xylitol, chosen to mimic the physical properties of the reaction mixture. Liquid samples were collected from the reactor outlet at intervals adjusted to the flow rate, and the tracer concentration was quantified by HPLC. The time delay introduced by the inlet tubing was determined in separate RTD experiments performed at the reactor inlet using three-way valves VV-X (Figure 5(a)) and the results were applied as a correction to the measured residence time distributions.

The cumulative residence time distribution F(t) was obtained from the tracer signal s(t) according to Equation (1).

$$F(t) = \frac{s(t) - s_0}{s_\infty - s_0}$$
 (1)

Where S_0 and S_∞ correspond to the baseline and the asymptotic signals at long times, respectively. The residence time distribution E(t) was then computed as the time derivative of F(t).

$$E(t) = \frac{dF(t)}{dt}$$
 (2)

The mean residence time \bar{t} and the variance σ^2_{θ} of the RTD were calculated from the first and second moments of E(t):

$$\bar{t} = \varepsilon_L \cdot \tau_L = \int_0^\infty E(t) dt$$
 (3)

$$\sigma_{\theta}^{2} = \int_{0}^{\infty} \left(\frac{t}{\varepsilon_{L} \cdot \tau_{L}} - 1 \right)^{2} \cdot E(t) dt$$
 (4)

Using the non-reactive transient axial dispersion model (ADM), the dimensionless variance $\sigma^2_{\ \theta}$ of the

residence time distribution (RTD) is related to the axial Peclet number $Pe_{ax} = \frac{u_z \cdot L_c}{D_z}$ through the axial dispersion coefficient, D_z , the linear velocity, u_z , and the characteristic length, L_c as:

$$\sigma_{\theta}^{2} = \frac{2}{Pe_{ax}^{2}} \left(Pe_{ax} - 1 + e^{-Pe_{ax}} \right)$$
 (5)

The experimental curves were fitted by nonlinear regression to a logistic function, which was differentiated analytically to compute the moments while avoiding noise amplification from numerical differentiation. Finally, Equation (5) was solved iteratively for Pe_{ax} using Brent's method implemented in Python.

2.8. Liquid holdup experiments

To determine the liquid holdup inside the reactor under the experimental conditions, a gravimetric recirculation method was employed, following the procedure described by García Serna et al. [33], as illustrated in Figure 6. The method is based on water mass balance: a fixed amount of water (200 g) was continuously recirculated at a constant liquid flow rate in a closed-loop system operating at fixed temperature, pressure, and gas flow rate. The change in water mass was continuously recorded until steady state was achieved.

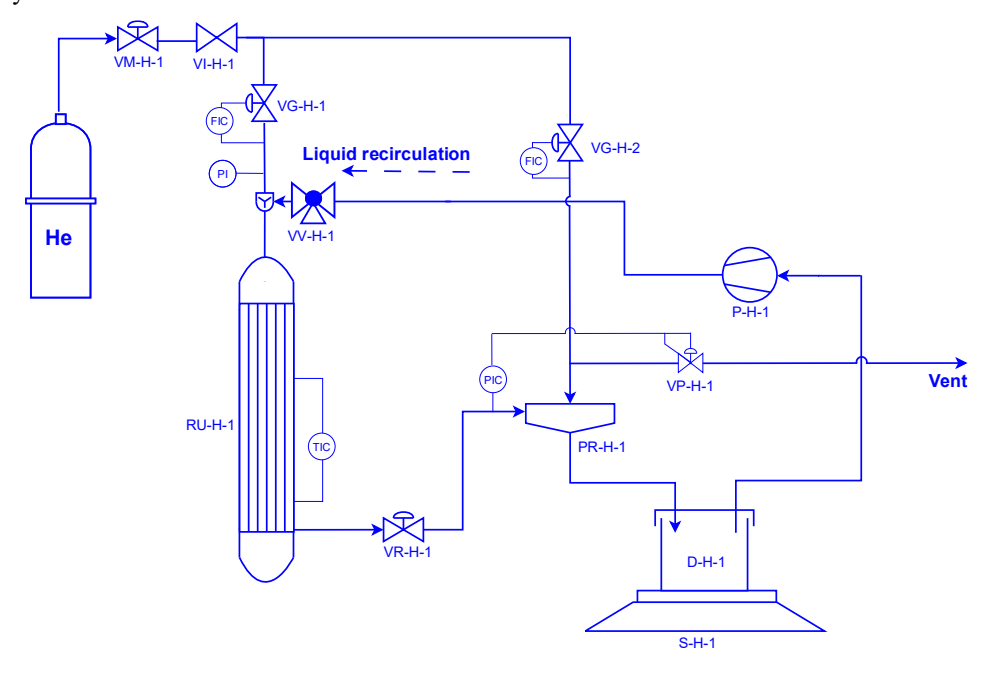


Figure 6. Experimental setup for liquid holdup measurements using the gravimetric recirculation method.

In a typical experiment, helium was continuously fed to the reactor at a controlled flow rate through valve VG-H-1, which served as the main gas inlet. A small auxiliary flow (5 mL·min⁻¹, NTP) was introduced via VG-H-2 to improve the pressure stability. The system pressure was maintained with a backpressure controller (EquilibarU3L Ultra Low Flow Back Pressure Regulator). Prior to each run, the liquid line was pre-filled with water up to the reactor inlet by setting the three-way valve VV-H-1 to close the path to the reactor and open the outlet to the atmosphere. Once the target temperature and pressure were reached, the scale was tared. At t = 0, the HPLC pump (P-H-1) was started, and the scale continuously recorded the water retained in the reactor. Mass measurement data were collected every minute until stabilization, enabling the determination of the liquid holdup at steady state.

Key process parameters—liquid flow rate (0.10–2.00 mL·min⁻¹), pressure (1–30 bar), and gas flow rate (50–200 mL·min⁻¹, NTP)— were varied systematically, while the temperature was fixed at 90 °C to represent the hydrogenation conditions and to prevent water evaporation. The liquid holdup was measured using the same packing employed in the continuous kinetic studies (Section 2.6). Independent measurements were carried out with the reactor packed only with Ru/C solid foams to determine the holdup specific to the catalytic section.

The liquid holdup (ε_L) is defined by Equation (6), where V_L and V_{Bed} are the retained liquid volume and total bed volume, respectively. Here, m_L is the measured mass of water retained in the reactor at a given time point, m_0 is the initial water mass in the bed, and \emptyset and L are the reactor diameter and length, respectively.

$$\varepsilon_{L} = \frac{\frac{V_{L}}{V_{Bed}}}{\frac{T_{L}}{4} \cdot \varnothing^{2} \cdot L}$$
 (6)

3. RESULTS AND DISCUSSION

In this work, different catalytic technologies were investigated for the hydrogenation of sugars. As discussed in Section 1, the most widely applied catalysts in this process are finely dispersed sponge nickel materials, commonly referred to as Raney-type catalysts. Although Raney nickel is economically attractive, it suffers from significant drawbacks, including lower intrinsic activity compared to ruthenium and a pronounced susceptibility to deactivation.

To address these limitations, the first part of this study focused on ruthenium catalysts supported on mesoporous molecular sieves (MMS). The selected supports—MCM-41, SBA-15, and MCF—provide high surface areas, ordered pore structures, and well-developed porosity, aiming to enhance the dispersion and stability of Ru nanoparticles. Their performance was benchmarked against a commercial Ru/C powder catalyst.

From an industrial perspective, however, Raney-type catalysts remain widely used. Therefore, in the second part of this work, solid Raney-type nickel foams were investigated as an alternative to conventional powdered Raney catalysts. Their application enables operation under continuous flow, and the role of molybdenum as a promoter was systematically studied. The activity, selectivity, and stability of these materials were assessed through detailed characterization combined with kinetic modelling.

Finally, in the third part of this work, a novel Ru/C solid foam catalyst was developed. Its preparation was optimized through a reproducible carbon coating and metal incorporation method, and its performance was evaluated through extensive kinetic experiments, both in semi-batch operation with single (xylose) and binary sugar mixtures (arabinose and galactose) and in continuous trickle-bed operation. Special attention was given to mathematical modelling, linking intrinsic kinetics with mass transfer and hydrodynamic effects.

3.1. Ru on mesoporous molecular sieves (Article IV)

3.1.1. Primary catalyst characterization

Ru-supported silicate and aluminosilicate mesoporous materials were synthesized following the procedure described in Section 2.2. and thoroughly characterized to elucidate their catalytic behaviour in xylose hydrogenation. Their performance was benchmarked against a commercial Ru/C catalyst. The obtained materials exhibited highly ordered mesostructures. SEM images (Article IV [34]) revealed that MCM-41 and SBA-15 silicates, as well as SBA-15 and MCF aluminosilicates, consist of rope-like particles with sizes of 1.0–1.5 µm, while Al-MCM-41 showed agglomerated spherical particles of 0.1–0.2 µm. The Ru loading of the synthesized materials was in the range of 2–4 wt.%, except for Ru/Si-MCM-41, which presented a lower loading of 1.2 wt.% (Table 1). This reduced loading in the silicate-based catalysts, compared to the aluminosilicate-supported samples, is attributed to weaker metal–support interactions in the absence of Al species. Conversely, the incorporation of Al enhanced these interactions, favouring the formation of acid sites and leading to higher Ru dispersion. This effect was corroborated by TEM analyses (Figure 7), where the aluminosilicate-based materials displayed smaller Ru nanoparticles than their pure silicate analogues.

Table 1. Key characteristics of Ru/MMS catalysts.

Catalyst	$w_{Ru}{}^a\!(wt.\%)$	$d_{Ru}{}^{b}\left(nm\right)$	D^{c}	$S_{BET}\left(m^2 \cdot g^{\text{-}1}\right)$	$V_{meso}(cm^3{\cdot}g^{\text{-}1})$
Ru/Si-MCM-41	1.2	4.8±1.4	0.27	665	0.59
Ru/Al-MCM-41	2.9	1.9±1.1	0.68	600	0.59
Ru/Si-SBA-15	2.2	3.8±1.3	0.34	435	0.54
Ru/Al-SBA-15	3.1	2.3±0.7	0.56	330	0.89
Ru/Al-MCF	3.6	2.0±0.9	0.64	230	1.08
Ru/C	5.9	4.7±1.5	0.27	445	0.15

^a Ruthenium loading; ^b Mean ruthenium nanoparticles size; ^c Ruthenium dispersion.

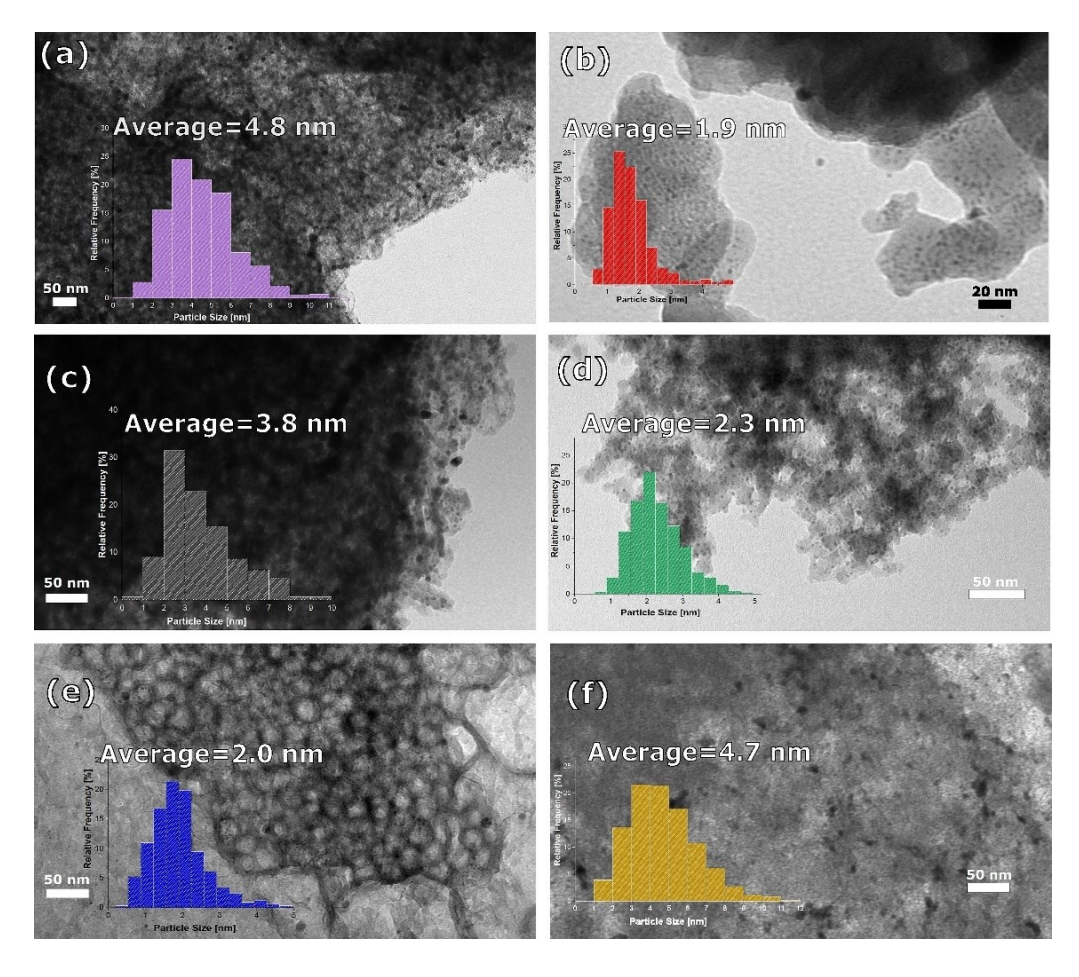


Figure 7. TEM images of (a) Ru/Si-MCM-41, (b) Ru/Al-MCM-41, (c) Ru/Si-SBA-15, (d) Ru/Al-SBA-15, (e) Ru/Al-MCF, (f) Ru/C.

Figure 8 shows the nitrogen physisorption isotherms of the synthesized catalysts. Both Ru/Si-MCM-41 and Ru/Al-MCM-41 exhibited type IV isotherms with an inflection point around a relative pressure of 0.3 and a narrow hysteresis loop, consistent with ordered mesopores of about 4 nm and high mesopore surface areas (595–640 m²·g⁻¹), typical for MCM-41 structures. Ru/Si-SBA-15, Ru/Al-SBA-15, and Ru/Al-MCF also showed type IV isotherms, but with pronounced H2(a)-type hysteresis loops [35], wider mesopores (10–30 nm), larger pore volumes (up to 1.08 cm³·g⁻¹), and comparatively lower surface areas. By contrast, the commercial Ru/C catalyst displayed a type I isotherm, combining micropores (~0.59 nm) with a broad distribution of mesopores. The mesoporous on the molecular sieves originated from the removal of polyethylene oxide units of Pluronic P-123. Notably, the textural

properties of Ru/Al-MCM-41 remained essentially unchanged after reaction, ruling out pore blocking or loss of surface area as causes of catalyst deactivation.

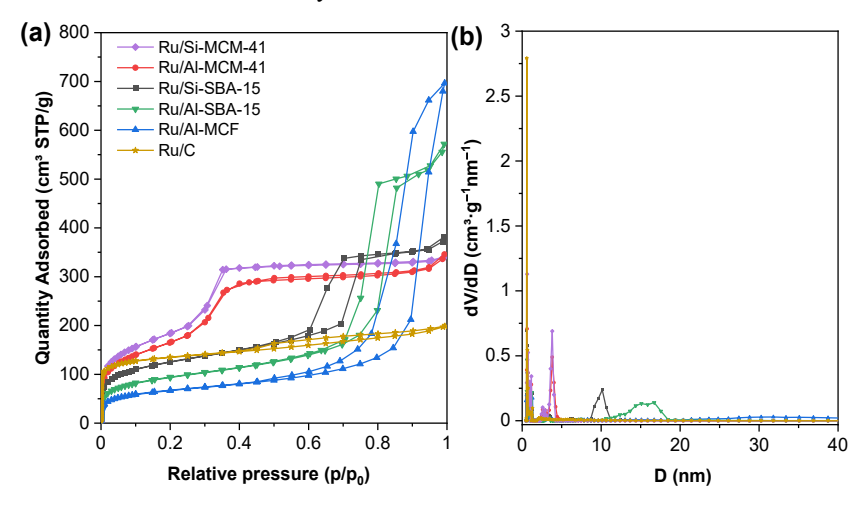


Figure 8. Nitrogen adsorption—desorption isotherms of Ru/MMS catalysts and commercial Ru/C: (a) isotherms at 77 K, (b) pore-size distribution curves (solid lines are guides for the eyes).

To gain further insight into the performance of the best Ru-supported MMS catalyst, Ru/Al-MCM-41, relative to the commercial Ru/C, XPS measurements were conducted on fresh and used samples of both catalysts. Figure 9 displays the XPS spectra of Ru/C and Ru/Al-MCM-41 before and after 4 h of xylose hydrogenation at 90 °C and 40 bar H₂, and the corresponding fitting data are presented in Article IV [34]. The XPS spectra confirmed the presence of multiple oxidation states of Ru in the Ru/Al-MCM-41 catalyst, with a lower Ru⁰ fraction after reaction. In contrast, Ru/C exhibited a shift towards lower oxidation states after use. The presence of reduced Ru species in Ru/C could account for its higher activity in xylose hydrogenation, while the reduction of Ru during reaction may explain the increase in activity commonly observed for Ru/C catalysts in aqueous-phase hydrogenations [36,37]. Nevertheless, the interpretation of the Ru 3d region requires caution, as the C–C peak overlaps with Ru signals.

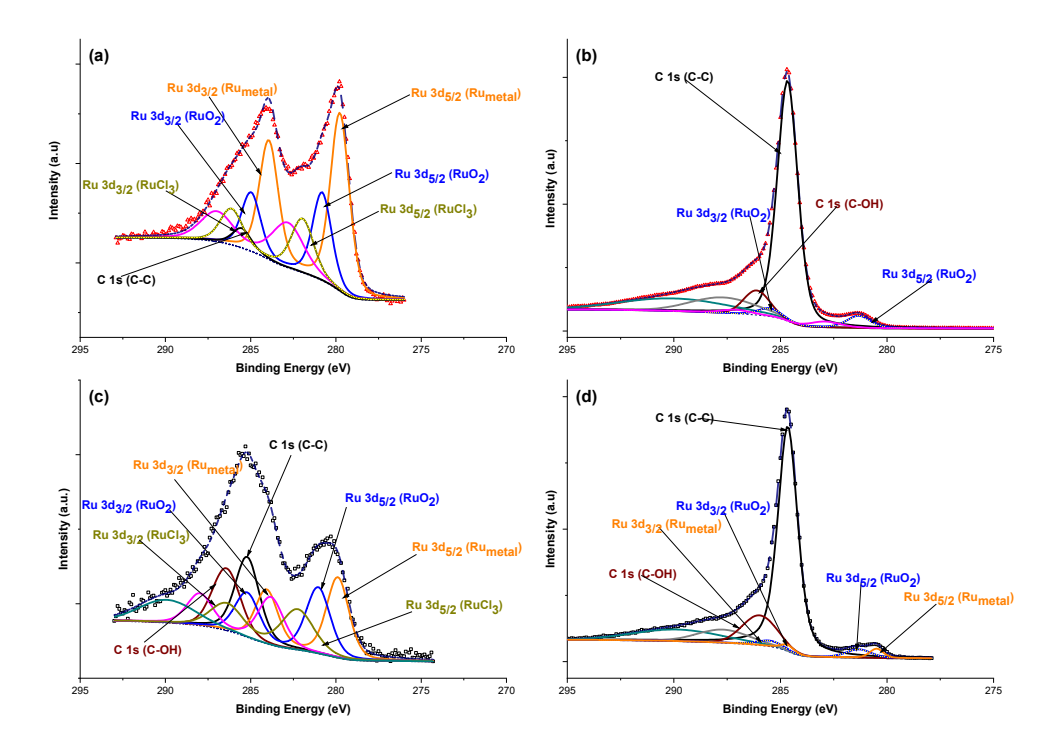


Figure 9. XPS in the Ru 3d region for (a) Ru/Al-MCM-41(fresh), (b) Ru/C (fresh), (c) Ru/Al-MCM-41 (used), and (d) Ru/C (used).

For comparison of Ru oxidation states and metal–support interactions, temperature-programmed reduction (TPR) profiles were recorded for fresh Ru/C, Ru/Si-MCM-41, and Ru/Al-MCM-41 (Figure 4, Article IV [34]. The main reduction peaks for Ru/Si-MCM-41 and Ru/Al-MCM-41 appeared at lower temperatures (106 and 127 °C, respectively) than those of Ru/C (210–220 °C), suggesting weaker metal–support interactions and/or higher accessibility of the Ru precursor on silica and aluminosilicate supports [38]. A broad peak at ca. 500 °C observed for Ru/C corresponds to methanation of the carbon support. The weaker interactions in the silica- and aluminosilicate-supported catalysts may also explain their stronger tendency to Ru leaching during reaction compared to Ru/C [39]. The higher peak intensity observed for Ru/Al-MCM-41 compared to Ru/Si-MCM-41 reflects its higher Ru loading, while the lower intensity of the Ru/C peak is consistent with the larger Ru particle size in this catalyst (Table 1).

3.1.2. Catalyst screening

The synthesized Ru/MMS catalysts and the commercial Ru/C were evaluated in xylose hydrogenation at 90 °C, 40 bar H₂, and an initial concentration of 0.13 M. Conversion profiles normalized by Ru mass are shown in Figure 10. After four hours of reaction, all catalysts reached conversions of 80–99 % and xylitol selectivity values of 93–99 %, confirming the well-established efficiency of ruthenium in the selective hydrogenation of carbohydrates in aqueous media [40]. At low conversion levels, the reaction was close to the zero-order with respect to xylose shifting towards the first order upon an increase of conversion. This resulted in conversion profiles featuring straight lines at the beginning, followed by bending as the reaction proceeded, finally reaching a plateau at almost complete conversion, in case of the most active catalysts.

All aluminosilicate-supported catalysts exhibited higher reaction rates than the silica-supported ones. The catalytic activity followed the order: Ru/C > Ru/Al-MCM-41 > Ru/Al-MCF \geq Ru/Al-Si-SBA-15 > Ru/Si-SBA-15 > Ru/Si-MCM-41. Among the synthesized materials, Ru/Al-MCM-41 showed the highest specific activity (per gram of Ru), with a performance comparable to the commercial Ru/C catalyst. Although the initial reaction rates of Ru/Al-MCM-41 (7.8 × 10⁻⁴ mol·kg_{Ru}⁻¹·s⁻¹) and Ru/C (9.0 × 10⁻⁴ mol·kg_{Ru}⁻¹·s⁻¹) were similar, the former displayed a higher xylitol yield (Figure 10(b)). Arabitol and erythritol were detected as minor by-products by HPLC. The former compound originated from xylose isomerization followed by hydrogenation, while the latter one appeared through retroaldol condensation and hydrogenation.

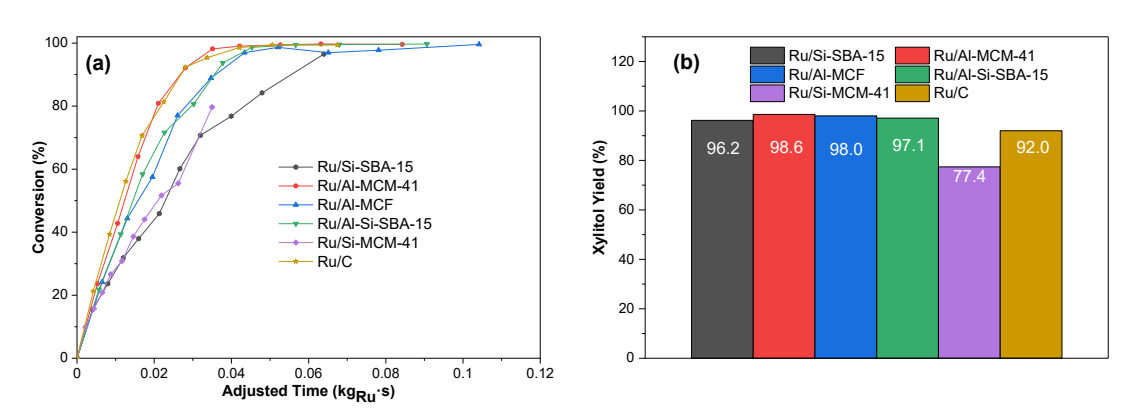


Figure 10. Comparison of D-xylose hydrogenation kinetics at 90 °C and 40 bar H₂ over the screened catalysts:

(a) conversion profiles; (b) xylitol yield after 4 h. Solid lines are guides for the eye.

3.1.3. Process parameters and stability

The effect of temperature was investigated for the most active Ru-supported MMS catalyst, Ru/Al-MCM-41. As expected, temperature strongly influenced the reaction rate, but selectivity towards xylitol remained high across the studied range, with only a slight decrease at 100 °C due to the formation of by-products. Figure 11(a) illustrates this behaviour: below 75 °C the reaction proceeded slowly, whereas at 90 °C, >99 % xylose conversion was achieved within 100 min with >99 % selectivity. At 75 °C, up to 240 min were required to reach the same conversion, while at 100 °C complete conversion was also obtained but selectivity decreased moderately to 95.5 %. The apparent activation energy was 43.21 kJ·mol⁻¹, in line with previously reported values for hydrogenation of monomeric sugars [39,41].

Figure 11(b) shows the effect of hydrogen pressure on xylose hydrogenation with Ru/Al-MCM-41. At pressures below 20 bar, the reaction rate increased significantly with hydrogen pressure, in agreement with previous studies on xylose hydrogenation [42] and other monomeric sugars [39,41]. Above 40 bar, however, the effect became negligible, indicating strong hydrogen adsorption on the Ru surface and saturation at the higher dissolved hydrogen concentrations, which leads to an apparent zero-order dependence on hydrogen.

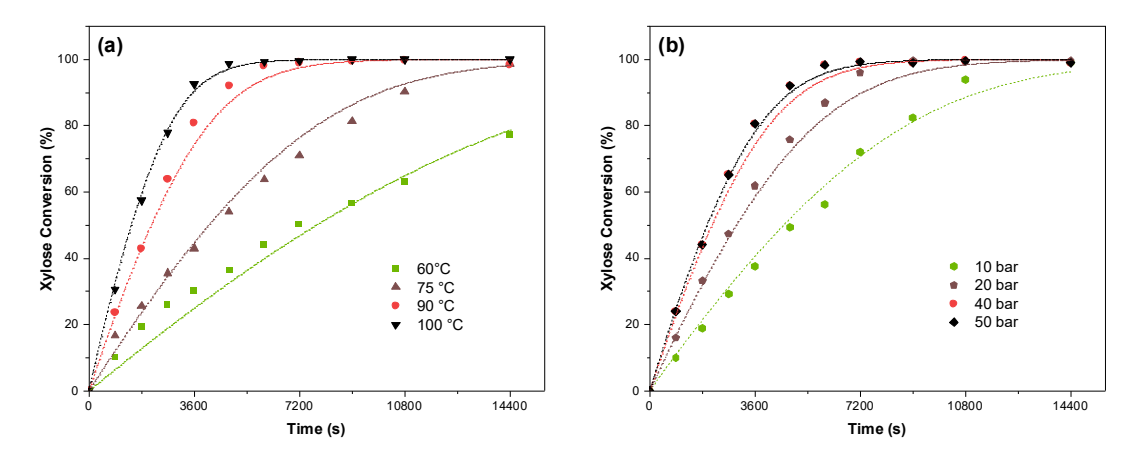


Figure 11. Xylose hydrogenation over Ru/Al-MCM-41: (a) effect of temperature; (b) effect of hydrogen pressure. Dashed lines are model predictions.

The reusability of Ru/Al-MCM-41 was evaluated by recovering part of the used catalyst through filtration, followed by five washing cycles and drying, and then performing a new experiment under identical conditions. Figure 12 compares the performance of fresh and reused Ru/Al-MCM-41. A decrease in activity of approximately 30 % relative to the initial rate was observed. Catalyst

deactivation can mainly be attributed to ruthenium leaching, as shown in Table 2, which also indicates that the extent of Ru dissolution is strongly influenced by reaction temperature. This highlights the need to optimize operational conditions to ensure catalyst reusability in practical applications. Nevertheless, xylitol selectivity and yield at final conversion remained essentially stable.

Table 2. Leaching of Ru from Ru/Al-MCM-41 catalyst after 4h of reaction determined by ICP-OES.

Temperature(°C)	$C_{Ru}^{a} (mg \cdot L^{-1})$	W _{Ru} (%) ^b
75	< 0.03	-
90	0.55	1.20
100	0.97	2.15

^a Ru concentration in final reaction mixture; ^b Percentage of dissolved Ru respect to initial loading.

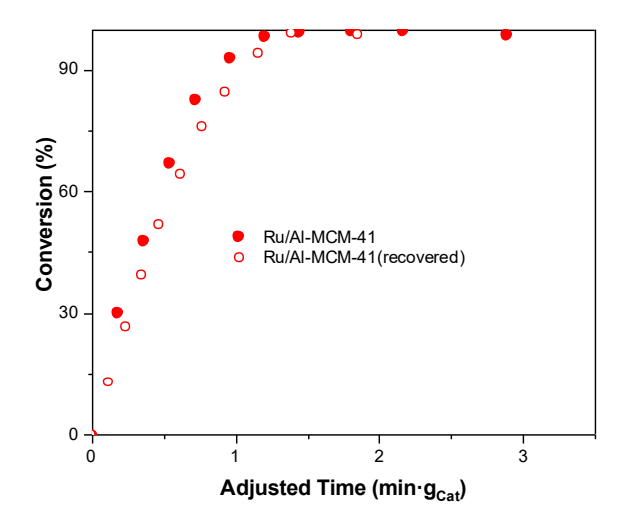


Figure 12. Comparison of the fresh and recovered Ru/Al-MCM-41 catalyst in xylose hydrogenation at 90 °C and 40 bar H₂.

Although the synthesized mesoporous silicate and aluminosilicate materials exhibit high surface areas and well-developed mesoporosity, the results demonstrate that suitable metal—support interactions are essential to stabilize Ru and maintain long-term catalytic activity. Nevertheless, these materials remain highly attractive because of their tunable textural and acidic properties. The presence of acid sites provides additional functionalities that could be combined with the intrinsic hydrogenation ability of Ru, opening opportunities for multifunctional catalysts. Such features are particularly promising for advanced applications such as one-pot conversion of hemicelluloses into sugar alcohols [43], where hydrolysis and hydrogenation steps could be efficiently integrated in a single catalyst system.

3.2. Raney-type solid foam catalysts (Article VI)

Solid Raney-type Ni foam catalysts, including molybdenum-promoted variants were tested in the selective hydrogenation of xylose to xylitol under both semi-batch and continuous operating conditions. The objective is to provide a deeper understanding of the behaviour of this novel structured catalyst technology and to assess its potential to bridge the gap between the conventional use of sponge nickel in semi-batch processes and its application in continuous operation.

Two types of Raney-type solid foam catalysts were investigated: Ev-F-Ni (Metalyst® MC 911, 80–95 % Ni) and Ev-F-NiMo (Metalyst® MC 981, 80–95 % Ni, Mo-promoted). The catalysts were tested as foam pieces with dimensions of 4 × 4 × 1.9 mm. In the semi-batch configuration, they were mounted in a SpinChem® rotating bed, as described in Section 2.5. For the continuous experiments, cylindrical foams of 10 mm in diameter and 1.9 mm in thickness were employed and loaded into a parallel screening reactor, as described in Section 2.6.

The handling of Raney-type catalysts must be carried out in the absence of oxygen due to their pyrophoric nature. Accordingly, the weighing procedure for kinetic experiments and catalyst characterization strictly followed the manufacturer's safety guidelines. A volumetric flask was first filled with distilled water, and the mass of the water $(m_{\rm H2O})$ was recorded. The required amount of catalyst was then introduced into the flask, ensuring that sufficient water was present to keep the material fully submerged. The water level was adjusted back to its original mark, and the new mass (m_s) was measured. The actual catalyst mass (m_{cat}) was calculated using Equation (7), applying a skeletal density correction factor (e=1.2) specific to the nickel foam catalysts.

$$m_{cat} = e \cdot \left(m_s - m_{H_2O} \right) \tag{7}$$

3.2.1. Semi-batch experiments and catalyst characterization

The catalytic performance of Ev-F-Ni and Ev-F-NiMo was evaluated through repeated semi- batch experiments under identical conditions. In the first cycle, Ev-F-NiMo exhibited markedly higher xylose conversion (Figure 13(a)) and an initial reaction rate nearly twice that of Ev-F-Ni (Figure 13(b)). Although both catalysts showed an initial activity loss of approximately 40 % after the first cycle, the subsequent deactivation followed an asymptotic trend, indicating a slower rate of decay. Throughout all cycles, Ev-F-NiMo consistently outperformed Ev-F-Ni. Moreover, Ev-F-NiMo displayed only half the Ni leaching observed for Ev-F-Ni in the first cycle (see Article VI [44]),

highlighting the stabilizing effect of molybdenum. By the fourth cycle, Ni leaching had decreased substantially for both catalysts, whereas Al leaching remained at comparable levels.

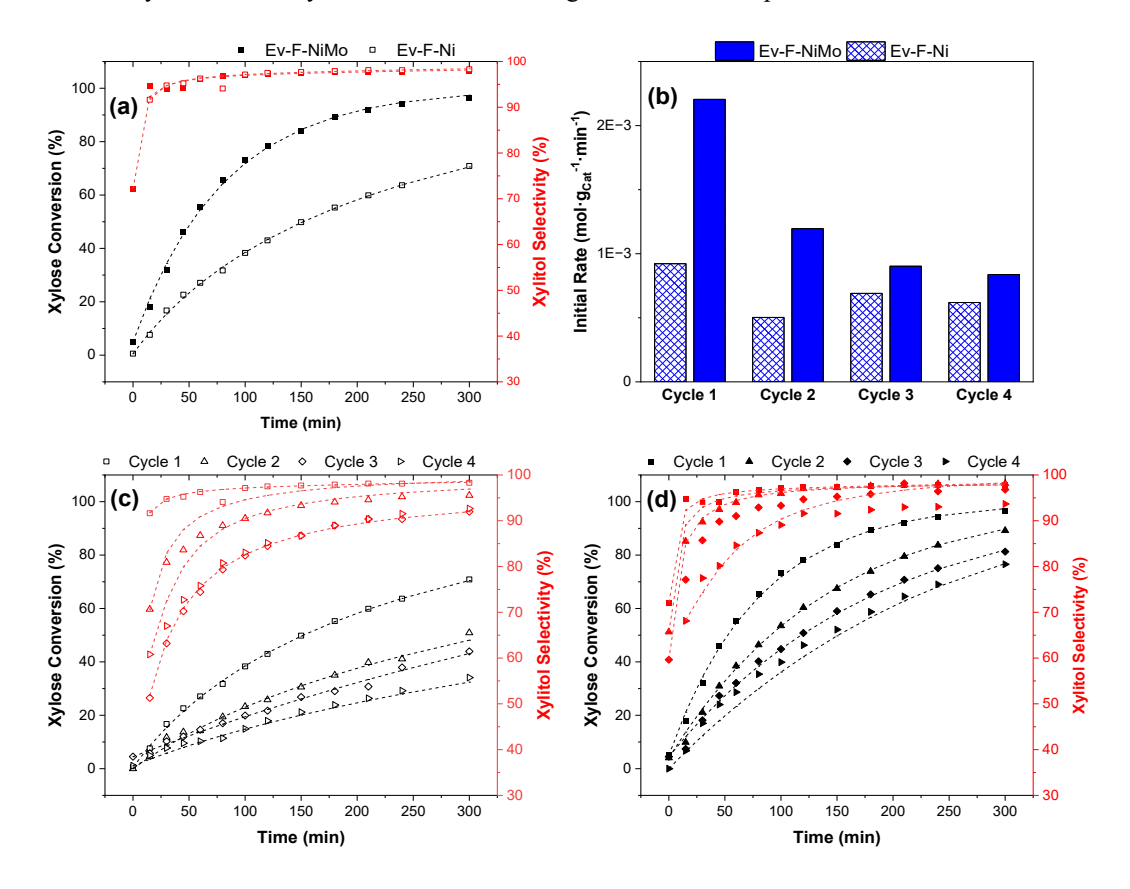


Figure 13. Semi-batch xylose hydrogenation at 90 °C, 30 bar H₂, and 0.75 g of Ni foam catalyst: (a) conversion and selectivity in cycle 1; (b) initial rate over consecutive cycles; (c) conversion and selectivity of Ev-F-Ni over four reuse cycles; (d) conversion and selectivity of Ev-F-NiMo over four reuse cycles.

Although the catalysts exhibited comparable surface areas (~25 m²·g⁻¹, Table 3), hydrogen chemisorption measurements indicated a slightly higher adsorption area for Ev-F-Ni (1.9 m²·g⁻¹) compared to Ev-F-NiMo (1.2 m²·g⁻¹). After four cycles, surface blockage prevented both nitrogen physisorption and hydrogen chemisorption analyses. Nevertheless, catalytic activity remained: in the fourth cycle, xylose conversion reached 25 % for Ev-F-Ni and 80 % for Ev-F-NiMo after 5 h. This observation suggests that the reaction conditions, namely hydrogen atmosphere and elevated temperature, may partially mitigate surface blockage by promoting poison desorption and enabling further hydrogenation.

Table 3. Surface area of Raney-type solid foams.

Catalyst	BET specific surface area, S _{BET} (m ² ·g ⁻¹)	Ni surface area, S _{Ni} (m ² ·g ⁻¹)	Sni/Sbet
Ev-F-NiMo Fresh	25	1.2	0.05
Ev-F-Ni Fresh	25	1.9	0.08

The blocking of hydrogenation sites also caused a reduction in xylitol selectivity, particularly for Ev-F-Ni at low xylose conversions, as shown in Figure 13 (c) and (d). The main by-products identified were xylulose (a ketopentose isomer of xylose) and arabitol (a stereoisomer of xylitol). Overall, the selectivity toward these by-products decreased with increasing xylose conversion, likely due to the progressive hydrogenation of xylulose into xylitol.

The formation of organic deposits on the catalyst surface—such as carboxylic acids, including xylonic acid in this case—has been proposed as a major cause of deactivation of Raney-type Ni catalysts in sugar hydrogenation [45–47]. These species exert two principal effects: they bind strongly to the active sites and, through chelation, promote metal leaching. As shown in the TGA profile in Figure 14, the used Ev-F-NiMo catalyst exhibited two major mass loss steps at \sim 250 °C and \sim 350 °C, with a total mass loss of \sim 10 %. In contrast, the fresh catalyst showed only a single mass loss step at \sim 230 °C with a 2 % mass loss. Together with the evidence of surface blockage from physisorption and chemisorption, these results support the hypothesis that organic deposits are a primary factor in catalyst deactivation.

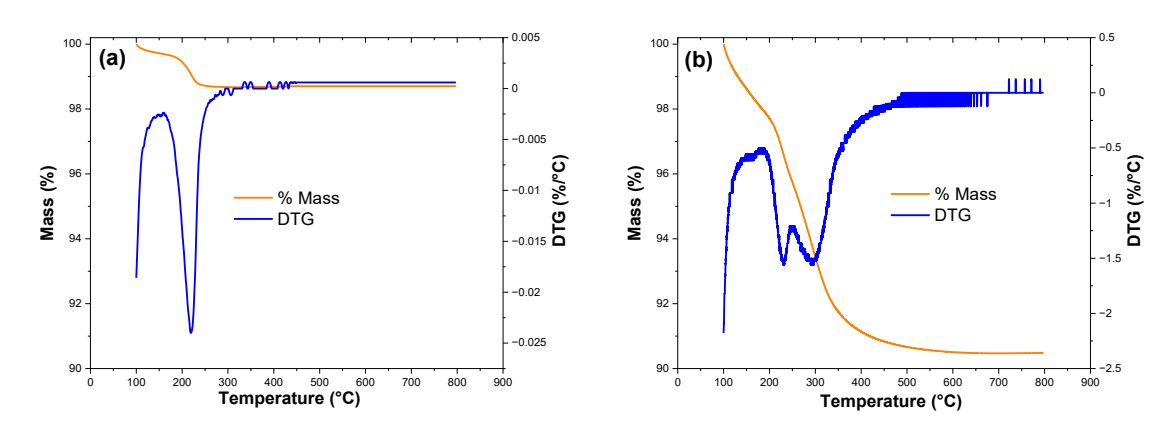


Figure 14. Thermogravimetric analysis for Ev-F-NiMo used in semi-batch experiments: (a) fresh catalyst; (b) catalyst after four reuses.

The oxidation state of the metals under reaction conditions is a key factor influencing catalytic performance. Figure 15 shows the XPS spectra in the Ni 2p and Ni 3p/Al 2p regions, together with the deconvolution of the identified surface species. In the Ni 2p region, peaks (average values) were assigned to metallic Ni at 852.6 eV (2p₃/₂) and 870.3 eV (2p₁/₂), NiO at 855.9 (2p₃/₂) and 873.4 eV (2p₁/₂), and Ni(OH)_x at 859.3 (2p₃/₂) and 876.8 eV (2p₁/₂). Characteristic satellite features of Ni²⁺ were observed at 864.1 eV and 881.1 eV. In the Ni 3p region, metallic Ni, NiO, and Ni(OH)_x were identified at 65.1, 67.4, and 69.7 eV, respectively. The Al 2p spectra displayed contributions from metallic Al (72.3 eV), Al₂O₃ (73.7 eV), and Al(OH)_x (75.9 eV). In addition, Mo species were detected: MoO₂ (Mo⁴⁺) at 230.8 and 233.8 eV, and MoO₃ (Mo⁶⁺) at 232.3 and 235.7 eV. A complete list of binding energies and peak assignments is provided in Article VI [44]. The analysis of surface species ratios is summarized in Table 4, where values derived from the Ni 2p and Ni 3p regions show close agreement, confirming the consistency of the spectral deconvolution.

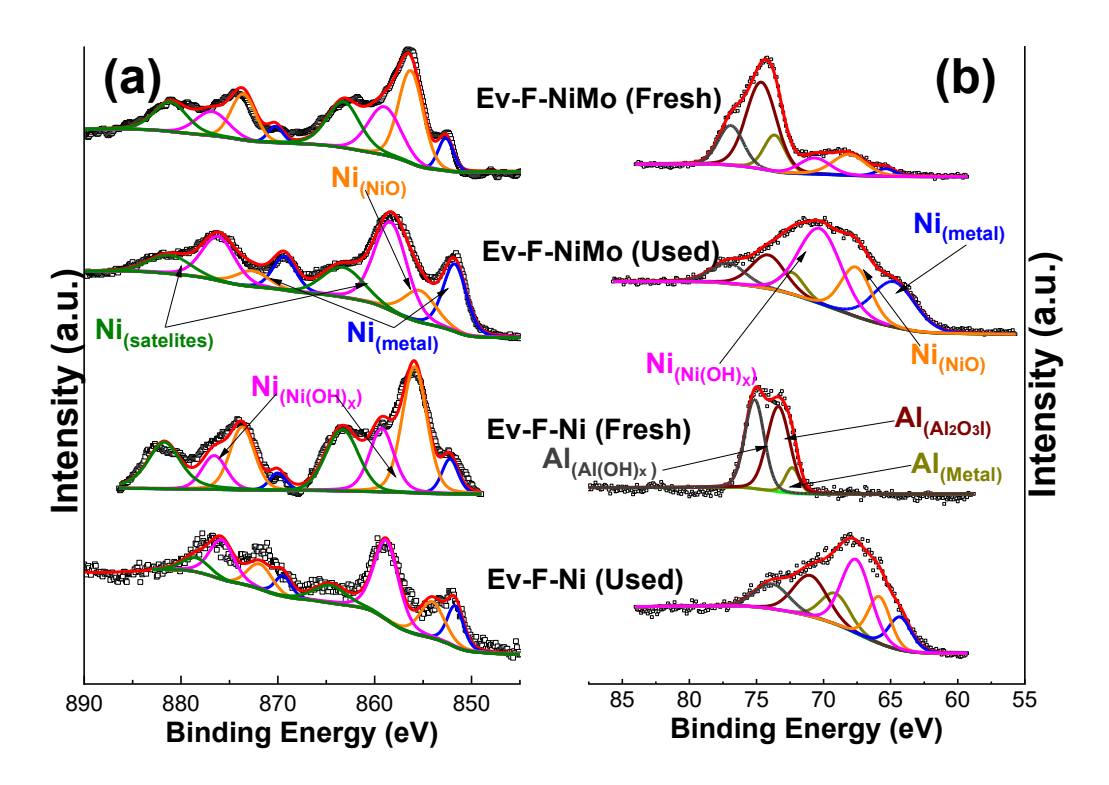


Figure 15. XPS spectra of Raney-type Ni foam catalysts in the (a) Ni 2p and (b) Ni 3p/Al 2p regions, including the deconvolution of the identified species.

In the fresh samples, the catalyst surface was enriched in aluminium (Ni $_{(total)}$ /Al $_{(total)}$) ratio ~0.40), mainly present in oxidized forms. The Al $_{metal}$ /Al $_{total}$ ratios were 0.18 and 0.09 for Ev-F-NiMo and Ev-F-Ni, respectively. After four reaction cycles, both catalysts showed increased intensity at 75.9 \pm 1.1 eV, consistent with aluminium hydroxide species resulting from interactions with aqueous media under reaction conditions. The Ni/Al ratio also increased post-reaction—up to 2.62 for Ev-F-NiMo and 1.37 for Ev-F-Ni—likely due to aluminum leaching [48].

Ev-F-NiMo consistently displayed a higher proportion of metallic Ni (fresh = 0.11; used = 0.29) compared to Ev-F-Ni (fresh = 0.10; used = 0.19). This, combined with the promoting effect of Mo—known to modify Ni's electronic properties and facilitate organic species adsorption and desorption—explains the superior activity of the Mo-doped catalyst [49]. The XPS analysis of Mo species (Electronic Supporting Information, Figure S4 in Article VI [44]) indicates that Mo exists in high oxidation states (6^+ and 4^+). Previous studies suggest that the improved stability of Raney-type Ni catalysts doped with small loadings of molybdenum arises from Mo protecting Ni active sites from oxidation [48,50].

The observed increase in the $Ni(OH)_x/Ni_{(total)}$ ratio after use (Ev-F-NiMo from 0.36 to 0.50; Ev-F-Ni from 0.30 to 0.54) corroborates the leaching trends observed in batch tests. Overall, the characterization confirms that the presence of Mo not only enhances the catalytic activity but also contributes to preserving Ni in its reduced, active form.

Table 4. Analysis of surface species on the studied catalysts from deconvolution of XPS spectra.

Ratio of species	Ev-F-NiMo (Fresh)	Ev-F-NiMo (Used)	Ev-F-Ni (Fresh)	Ev-F-Ni (Used)
$Ni_{(metal)}/Ni_{(total)}$	0.11	0.29	0.10	0.19
NiO/Ni _(total)	0.53	0.21	0.60	0.27
Ni(OH) _x /Ni _(total)	0.36	0.50	0.30	0.54
Ni _(total) /Al _(total)	0.36	2.62	0.40	1.36
Al _(metal) /Al _(total)	0.18	0.22	0.09	0.28
Al ₂ O ₃ /Al _(total)	0.59	0.48	0.48	0.44
Al(OH) _x /Al _(total)	0.22	0.30	0.43	0.27

3.2.2. Deactivation modelling

To interpret the behavior of the catalyst in recycle semi-batch experiments, a kinetic model was fitted to the experimental data. The derivation of the rate expressions is presented in Article VI [44]. The proposed reaction network, based on the detected species, is presented in Figure 16. The main pathway corresponds to the hydrogenation of xylose to xylitol (r₁). Xylose can also isomerize to its ketopentose isomer, xylulose (r₂), which can convert back to xylose (r₃). Xylulose hydrogenation yields a mixture of pentitols, primarily xylitol and arabitol (also known as lyxitol), via reactions r₄ and r₅, respectively.

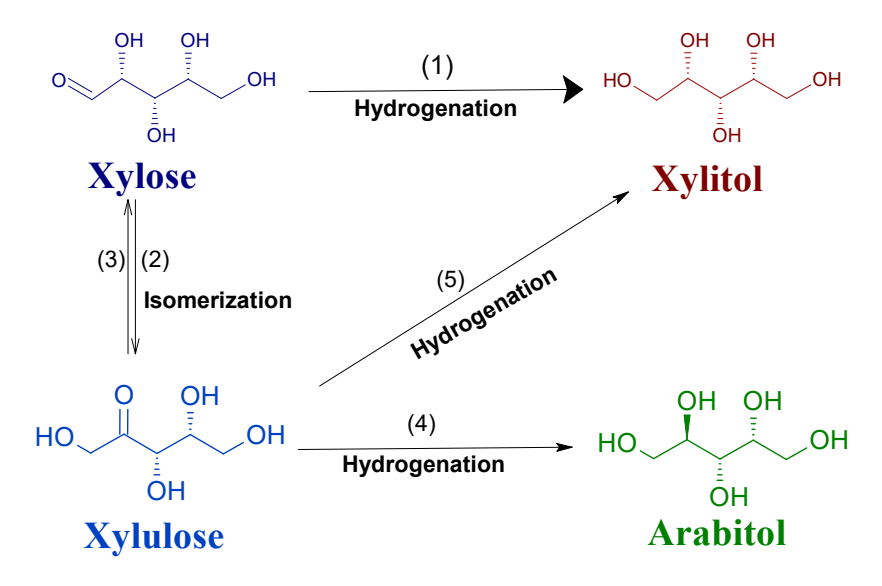


Figure 16. Reaction network for xylose hydrogenation using Raney-type Ni foam catalysts.

Considering the large size difference between hydrogen and sugar molecules, a non-competitive adsorption model was adopted. The adsorption of the products was excluded from the model, as preliminary fitting indicated that their adsorption constants were negligible compared to that of xylose. The resulting rate expressions are summarized in Equations(8)-(12).

$$r_{1} = \frac{\kappa_{1, 363K} \cdot C_{X}}{\left(1 + K_{X, 363K} \cdot C_{X}\right)}$$
(8)

$$r_2 = \frac{\kappa_{2, 363K} \cdot C_X}{\left(1 + K_{X, 363K} \cdot C_X\right)}$$
 (9)

$$r_{3} = \frac{\kappa_{3, 363K} \cdot C_{Xy}}{\left(1 + K_{X, 363K} \cdot C_{X}\right)}$$
(10)

$$r_4 = \frac{\kappa_{4, 363K} \cdot C_{Xy}}{\left(1 + K_{X, 363K} \cdot C_X\right)}$$
 (11)

$$r_{5} = \frac{\kappa_{5, 363K} \cdot C_{Xy}}{\left(1 + K_{X, 363K} \cdot C_{X}\right)}$$
 (12)

The effect of the external mass transfer limitations was neglected giving the low concentration utilized during the experiments (0.14 M) and the high agitation rate (700 rpm). The internal mass transfer limitation in the catalyst pores were not considered because of the thin catalyst layers and the low concentrations used during the experiments. Consequently, the mass balance equations for the present species reduce to simplified forms, as expressed in Equations (13)-(16), where ρ_B denotes the catalyst bulk density, defined as the ratio between the catalyst mass (m_{Cat}) and the liquid volume (V_L).

$$\frac{dC_X}{dt} = \left(-r_1 \cdot a - r_2 + r_3\right) \cdot \rho_B \tag{13}$$

$$\frac{dC_{X_{OH}}}{dt} = (r_1 \cdot a + r_4) \cdot \rho_B$$
 (14)

$$\frac{dC_{Xy}}{dt} = (r_2 - r_3 - r_4 - r_5) \cdot \rho_B$$
 (15)

$$\frac{dC_{\Lambda_{OH}}}{dt} = r_4 \cdot \rho_B \tag{16}$$

In the above equations, a denotes the catalyst activity factor (0-1), with a=1 corresponding to the initial activity of the catalyst and a=0 to a condition of complete deactivation. The experiments indicate that the catalysts retained a residual activity, denoted as the asymptotic value a', which is approached upon repeated recycling. The time dependence of the activity a was described by a first-order deactivation model Equation (17), where $k_{d, 363 \text{ K}}$ is the deactivation rate constant [51]. A similar approach has been successfully applied to describe the hydrogenation of xylose on Raney NiMo powder catalysts [17] and the hydrogenation of citral [52].

$$\frac{\mathrm{da}}{\mathrm{dt}} = k_{\mathrm{d,363 K}} \cdot (a - a') \tag{17}$$

Integrating Equation (17) analytically with the initial conditions: t=0, a=1 yields the following expression,

$$a=a'+(1-a')e^{-k_{d,363}K}$$
 (18)

In the initial approach, by-product formation was neglected ($r_2 = r_3 = r_4 = 0$) to estimate $k_{1, 363 \text{ K}}$, $k_{d, 363 \text{ K}}$, a', and $K_{X, 363 \text{ K}}$. After determining these parameters, by-product formation was introduced into the model, and the corresponding kinetic constants were evaluated. The system of ordinary differential (Equations (13)-(16)) was solved with the LSODA algorithm for stiff equations, and parameter estimation was performed by minimizing the objective function (Q) using the Nelder–Mead optimization method in Python.

$$Q = \sum_{i=1}^{N_{\text{Exp}}} \sum_{j=1}^{N_{\text{C}}} \left(C_{i,j}^{\text{Exp}} - C_{i,j}^{\text{Calc}} \right)^{2}$$
(19)

The time variable in the equations corresponds to the cumulative reaction time experienced by the catalyst under operating conditions. Consequently, the initial activity of the catalyst for each experiment was set to the final activity from the preceding experiment.

Figure 17 and Figure 18 compare the experimental and modeled concentration profiles for Ev-F-NiMo and EV-F-Ni, respectively, with the fitted parameters summarized in Table 5. The model reproduced the experimental data with excellent accuracy. Ev-F-NiMo displayed roughly twice the activity of Ev-F-Ni for the main reaction, as indicated by the fitted rate constant. The asymptotic activity values were 0.33 for Ev-F-NiMo and 0.24 for Ev-F-Ni. However, the deactivation rate constant was markedly higher for the unpromoted Ev-F-Ni.

Table 5. Fitted kinetic parameters for the deactivation model.

Parameter	Ev-F-NiMo	Relative Error (%)	Ev-F-Ni	Relative Error (%)
$\kappa_{1, 363 \text{ K}} (\times 10^{-5}) / \text{m}^3 \cdot \text{kg}_{\text{Cat}}^{-1} \cdot \text{s}^{-1}$	7.53	14	3.28	25
K _{X, 363 K} (×10 ⁻³) / m ³ ·mol ⁻¹	1.94	90	1.96	>100
k _{d, 363 K} (×10 ⁻³) / (-)	2.95	20	3.43	14
a'/(-)	0.33	9.4	0.24	10

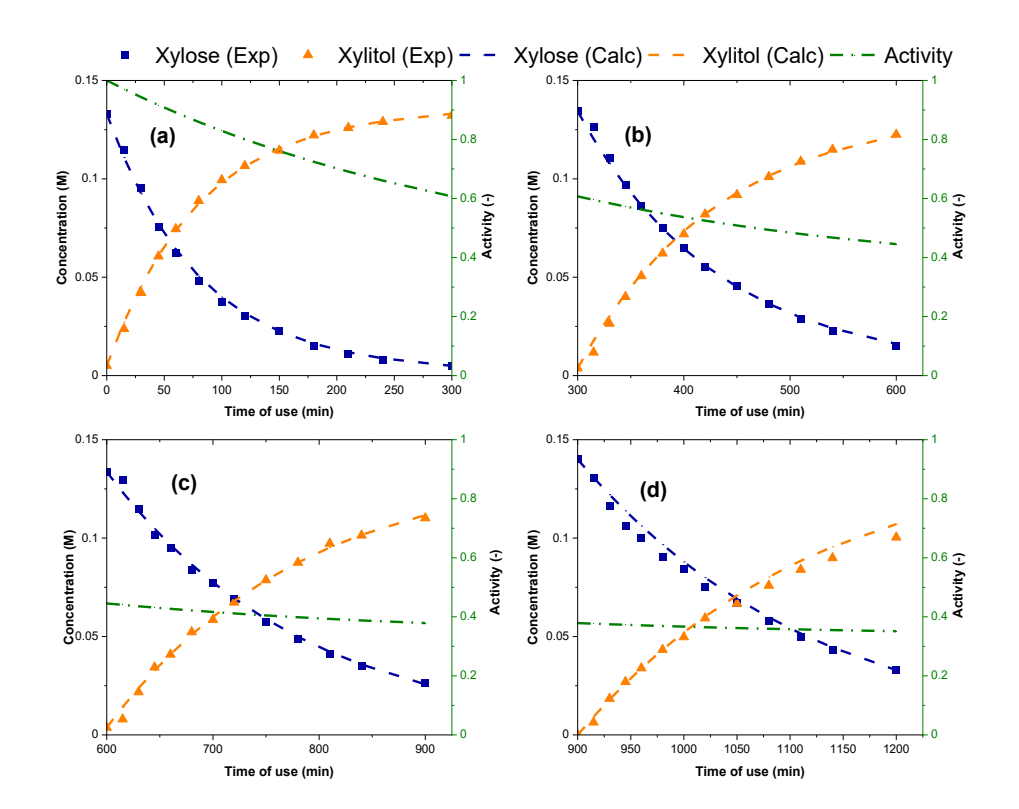


Figure 17. Fitting results for the catalyst Ev-F-NiMo to the deactivation model across different recycling experiments: (a) cycle 1, (b) cycle 2, (c) cycle 3, and (d) cycle 4.

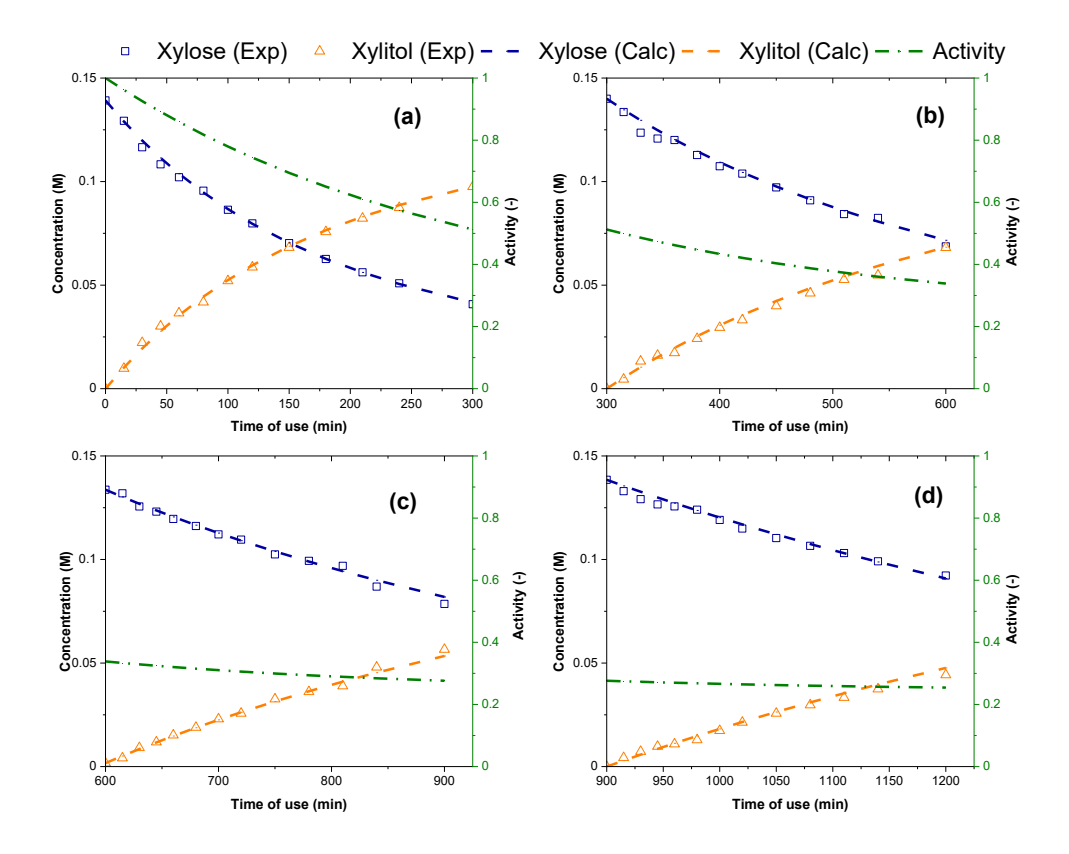


Figure 18. Fitting results for the catalyst Ev-F-Ni to the deactivation model across different recycling experiments: (a) cycle 1, (b) cycle 2, (c) cycle 3, and (d) cycle 4.

3.2.3. Continuous hydrogenation experiments

In the initial continuous operation experiment (Figure 19), Ev-F-NiMo exhibited a marked increase in xylitol yield after ~200 min, along with a significant decrease in the isomerization by-product xylulose. In contrast, Ev-F-Ni showed a less pronounced activity increase but achieved a considerable reduction of by-products, particularly xylulose. This behavior is attributed to improved hydrogen distribution in the liquid phase as the catalyst bed became saturated with the sugar solution. After this stage, both catalysts maintained stable performance during time-on-stream.

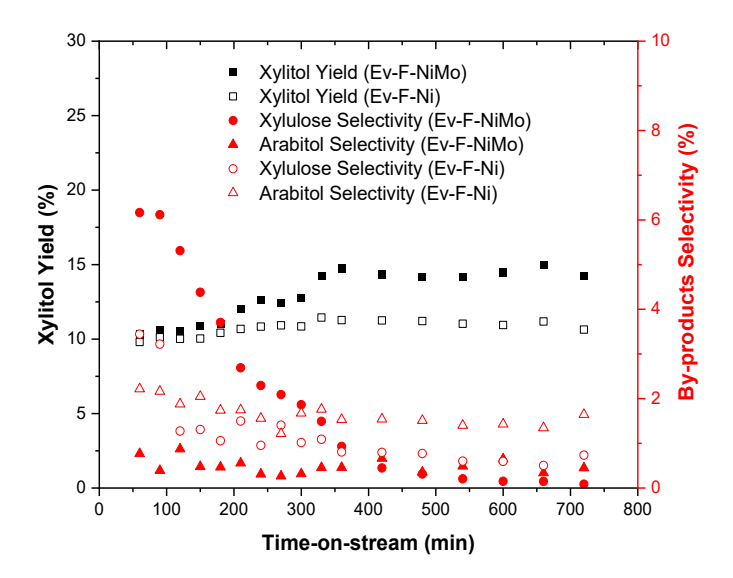


Figure 19. Performance of Ni foam catalysts during the initial continuous operation experiment. Conditions: xylose feed 0.25 mL·min⁻¹ (0.14 M), 90 °C, 20 bar H₂ (6.6 mL·min⁻¹), 0.25 g of catalyst.

The effect of the key process parameters, temperature and liquid flow rate was investigated in continuous operation using two catalyst loadings of Ev-F-NiMo. A loading of 0.25 g was used to evaluate the behavior at medium conversions, while 1.2 g was used to examine the performance at high xylose conversions.

As expected, the reaction temperature strongly influenced the xylitol yield (Figure 20). Although higher temperatures promoted by-product formation, the selectivity remained above 97%. The apparent activation energy was estimated as 43.9 kJ·mol⁻¹, consistent with previously reported values for xylose hydrogenation [53]. At higher catalyst loading, the effect of temperature became less pronounced, primarily due to slower kinetics at the low xylose concentrations prevailing in the final section of the catalytic bed.

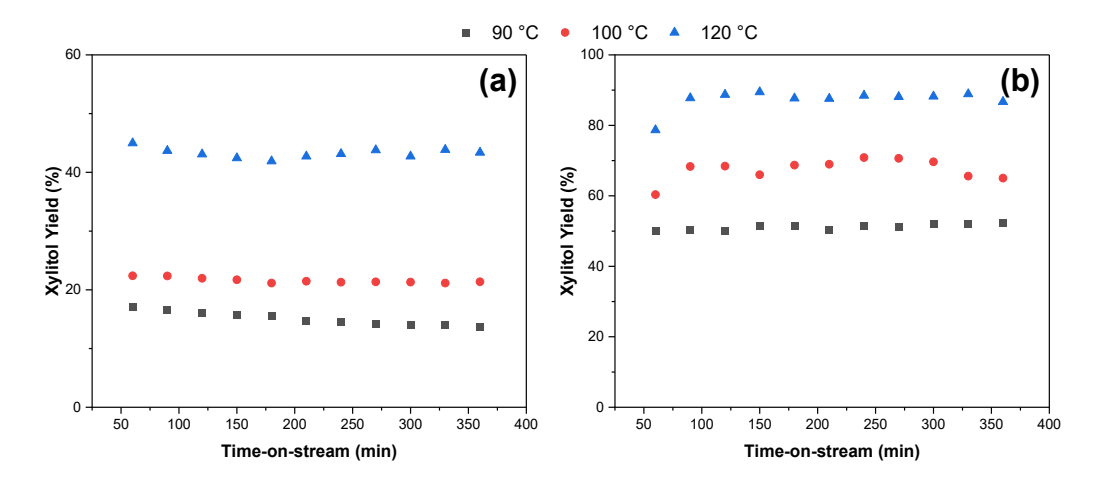


Figure 20. Effect of temperature on continuous hydrogenation of xylose on Ev-F-NiMo. Conditions: 0.25 mL·min⁻¹ feed (xylose 0.14 M), 6.6 mL·min⁻¹ H₂ (20 bar) with catalyst loading of (a) 0.25 g and (b) 1.2 g.

The effect of the liquid flow rate on the xylitol yield is shown in Figure 21. Sugar hydrogenation is a relatively slow reaction; therefore, a decrease in residence time directly impacts the conversion, with increased flow rates reducing the xylitol yield. However, there is a compensating effect: low liquid flow rates imply low Reynolds numbers, which in turn result in low Sherwood numbers (Sh), i.e. low mass transfer coefficients [54].

It is worth highlighting that under continuous-flow conditions, the extent of observed catalyst deactivation was notably lower than in batch operation, likely due to enhanced desorption of poisoning species with the steady feed of fresh reactants into the reactor tube.

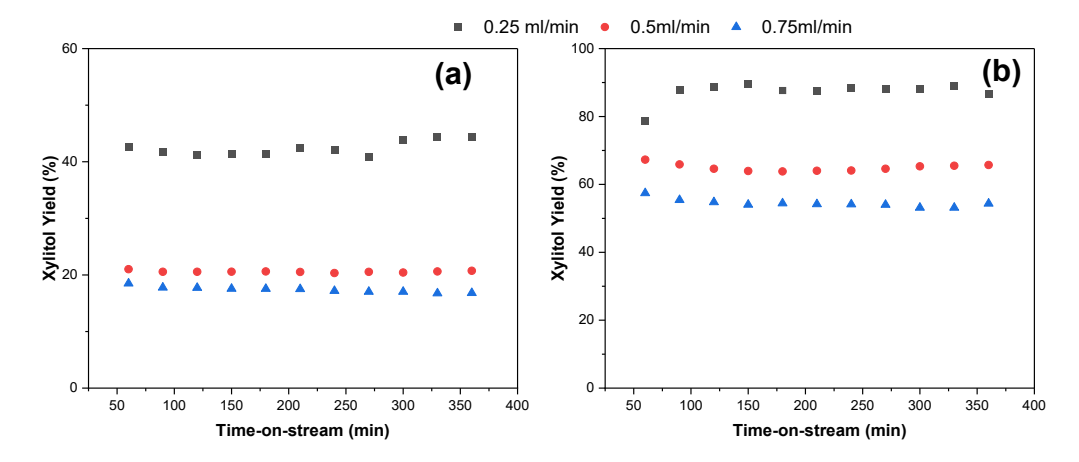


Figure 21. Effect of liquid flow rate on continuous hydrogenation of xylose using Ev-F-NiMo. Conditions: 120 °C, feed (xylose 0.14 M), 6.6 mL·min⁻¹ H₂ (20 bar), with catalyst loadings of (a) 0.25 g and (b) 1.2 g.

The formation of aldonic acids, such as gluconic acid in glucose hydrogenation, lactobionic acid in lactose hydrogenation, and xylonic acid in xylose hydrogenation, has been identified as an important cause of deactivation of Raney-type Ni catalysts under non-optimal hydrogen pressure and high temperatures. These species adsorb strongly on active sites and, through chelation, promote metal leaching. Literature studies (DFT and in situ FTIR) support this hypothesis, showing strong carboxylate binding of gluconic acid on Ni surfaces [46].

In agreement, batch experiments reported in the literature demonstrated severe activity losses when Raney Ni catalysts were exposed to aldonic acids [18,45]. To evaluate this effect under continuous flow, Ev-F-NiMo was exposed to a dilute xylonic acid solution after stabilization (270 min). As shown in Figure 22, the xylitol yield decreased modestly (~5 %), and the catalyst fully recovered its activity once the contaminant was removed, indicating that continuous operation mitigates poison accumulation. A slight increase in xylulose selectivity (0.8 % to 3 %) further suggested that the acidic medium may promote aldose–ketose isomerization.

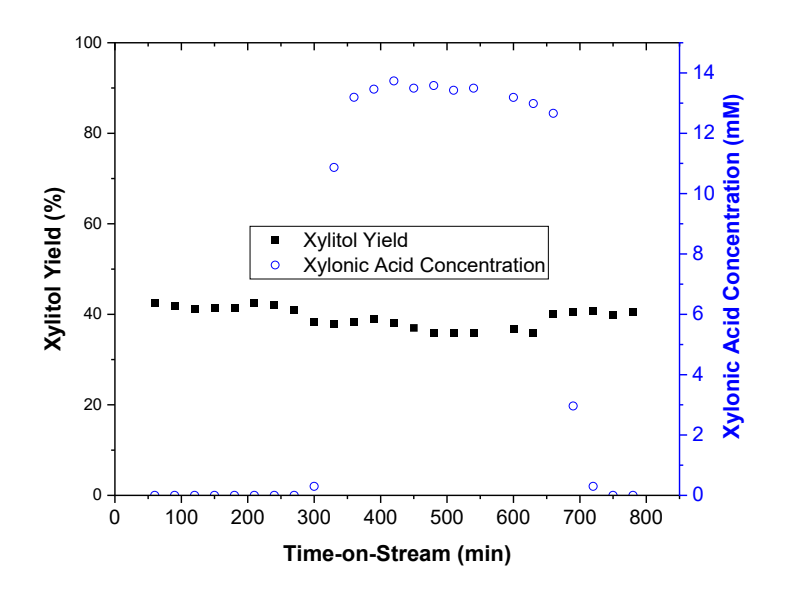


Figure 22. Poison-response experiment. 0.14 M xylose (0.25 mL·min⁻¹), 120 °C, 20 bar, 6.6 mL·min⁻¹ H₂, 0.3 g catalyst (Ev-F-NiMo).

Overall, the results demonstrate the potential of solid Raney-type Ni foams as an alternative for continuous hydrogenation of xylose to xylitol based a non-noble metal. The Mo-promoted foam (Ev-F-NiMo) consistently outperformed the unpromoted analogue, showing higher activity, stability, and selectivity. Continuous operation further reduced the extent of deactivation compared to batch mode, while kinetic modeling provided a coherent description of the reaction and deactivation behavior, supporting the superior performance of the promoted catalyst.

3.3. Ru/C solid foam catalysts (Articles I–III and Appendix I)

Given the high activity, selectivity, and stability of Ru/C catalysts in sugar hydrogenation, solid Ru/C foams were developed as a novel structured catalytic system that also enable continuous operation. The synthesis method was optimized to obtain reproducible and robust catalysts, which were then tested in semi-batch operation for the selective hydrogenation of monomeric sugars—xylose, arabinose, and galactose—as well as binary mixtures of arabinose and galactose. Extensive kinetic data were collected and modeled, providing valuable insight into the intrinsic kinetics and the effect of operating conditions. The study was further extended to continuous operation in a parallel screening reactor under trickle-bed conditions, complemented by hydrodynamic experiments on liquid hold-up and residence time distribution, which allowed to model and analyse the data from the continuous operation experiments.

3.3.1. Catalyst synthesis results

Ru/C solid foam catalysts were synthesized according to the procedure described in Section 2.3. The preparation involved anodic oxidation of Al foams, coating with poly(furfuryl alcohol) (P(FA)), pyrolysis/activation to obtain a thin carbon layer, and Ru deposition followed by reduction. Figure 23 displays the open-cell foam at the successive synthesis stages.

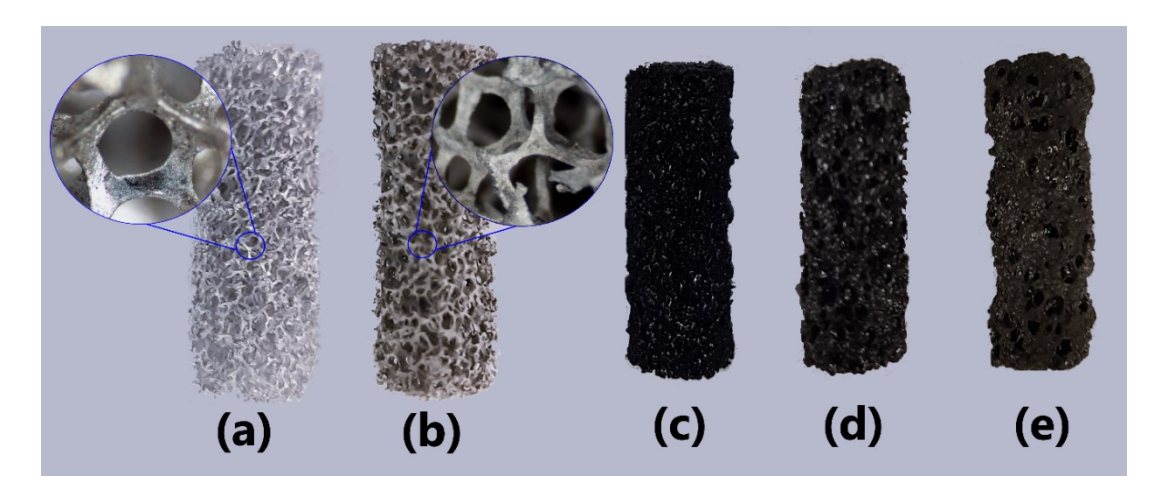


Figure 23. Synthesis stages of Ru/C foam catalyst: (a) untreated open-cell Al foam; (b) anodized and calcined foam; (c) P(FA)-coated foam; (d) pyrolyzed/oxygen-treated foam; (e) Ru-impregnated and reduced catalyst.

After the anodic oxidation, the glossy silver colour of the untreated aluminium foam pieces changed to a grey matte colour, suggesting the formation of a well-distributed oxide layer (Figure 23(a)-(b)). SEM images (Figure 24) of the surface textures at different stages of the anodic oxidation process

revealed that the surface was changed from a mainly smooth texture (Figure 24 (a)) to be covered by fibre-shaped features in case of the anodized sample (Figure 24 (b)), and by a semi-regular hexagonal nanopores (with an average size of 220 nm) in case of the anodized and calcined sample (Figure 24 (c)). These pores of a hexagonal arrangement are typical for anodic aluminium oxide [55].

The differences between the micrographs before and after the calcination demonstrate the need for such a treatment to obtain a more uniform pore pattern and to eliminate surface sub-holes. This effect is ascribed to the diffusion of the ambient oxygen and the aluminium from the substrate through the existing aluminium oxide layer, which combine to form additional oxide, suggested also by the remarkable increase of the oxygen content on the surface after the calcination step as reported in Article I [56]. On the other hand, the increase in the content of other minority elements (S, Mg, Si, Fe) can be ascribed to the presence of impurities in the used sulphuric acid.

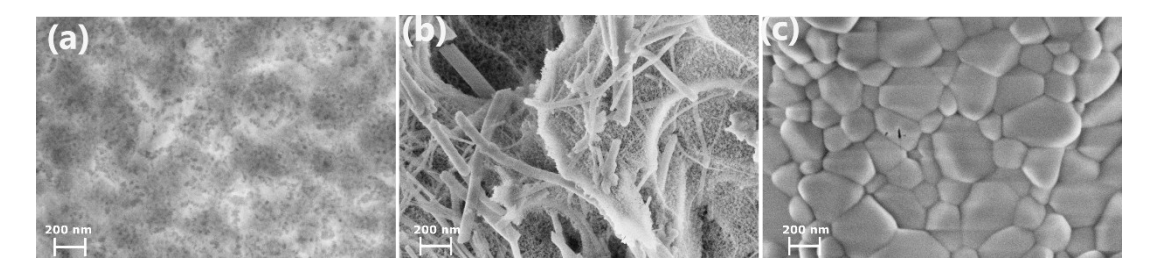


Figure 24. SEM micrographs of Al foams: (a) untreated; (b) anodized; (c) anodized and calcined.

The carbon coating of anodized aluminium foams was carried out by controlled polymerization of furfuryl alcohol, followed by pyrolysis and subsequent activation under an air stream. Polymerization proceeded via stepwise heating in the presence of oxalic acid as catalyst. Water in the mixture—both liquid and evaporated—played a critical role in cross-linking and cavity formation, which determine the cohesion and porosity of the resulting carbon layer [57]. Under experimental conditions, two types of polymeric coatings were obtained: (i) a dark, foamy material, formed when rapid heating and water vaporization occurred above 110 °C, and (ii) a golden-colored, less viscous polymer when these effects were absent. Carbons derived from the former showed superior properties as catalyst supports, including higher surface area, more homogeneous coverage, and enhanced acid resistance.

Although the detailed mechanism of furfuryl alcohol polymerization remains debated, it is generally accepted that under acidic conditions the main product is a linear poly(furfuryl alcohol) structure linked

by methylene bridges. Branching and cross-linking darken the mixture and increase its viscosity, while the exothermic character of the reactions leads to water vaporization and cavity formation [57].

Carbons obtained by direct pyrolysis of P(FA) are typically microporous, displaying type I nitrogen adsorption—desorption isotherms [35], often with open hysteresis loops due to diffusion limitations in the narrowest nanopores [57, 58]. To introduce mesoporosity, various activation strategies have been reported, such as high-temperature treatments (above 800 °C) with CO₂ or steam [59, 60], or the addition of pore-forming agents during polymerization [61, 62]. The latter was adopted in this work, since the aluminium foam substrate restricts the maximum activation temperature. Poly(ethylene glycol) (PEG, 8 kDa) was selected as pore-former, aiming to tailor the carbon framework towards mesopore generation. This approach is consistent with the objective of achieving better dispersion of ruthenium nanoparticles (typically 1.5–5 nm) and enhanced accessibility for relatively large sugar molecules [27, 36, 39, 63].

The carbon layer obtained from pyrolyzing the P(FA)/PEG mixture at 550 °C retained approximately 40% of the original mass. In contrast, PEG alone produced a negligible carbon residue, as confirmed by thermogravimetric analysis (Figure 25) and the carbon contents reported in Table 6. The effect of PEG addition on the foam surface is illustrated by the SEM images shown in Figure 26. Increasing PEG content in the precursor mixture promoted the formation of surface depressions and more developed porosity, while excessive addition (>20 wt.%) caused collapse of the carbon layer.

Table 6. Mass of foam pieces throughout the catalyst synthesis process.

PEG (wt. %)	Initial mass (g)	After A.O. (g)	P(FA)	After pyrolysis	After activation
1 EG (wt. 70)	imuai mass (g)	Alta A.O. (g)	(wt. %)	(C wt.%)	(C wt.%)
0	0.6314±0.0018	0.5915±0.0035	78.90 ± 0.76	59.39 ± 3.67	49.99 ± 7.41
3	0.6179±0.0039	0.5678±0.0054	74.02 ± 1.9	53.25 ± 3.62	32.24 ± 7.33
5	0.6294±0.0017	0.5800±0.0016	64.21 ± 0.11	43.18 ± 0.62	39.06 ± 1.59
15	0.6171±0.0239	0.5705±0.0239	50.94 ± 2.23	29.77 ± 2.20	27.68 ± 2.73

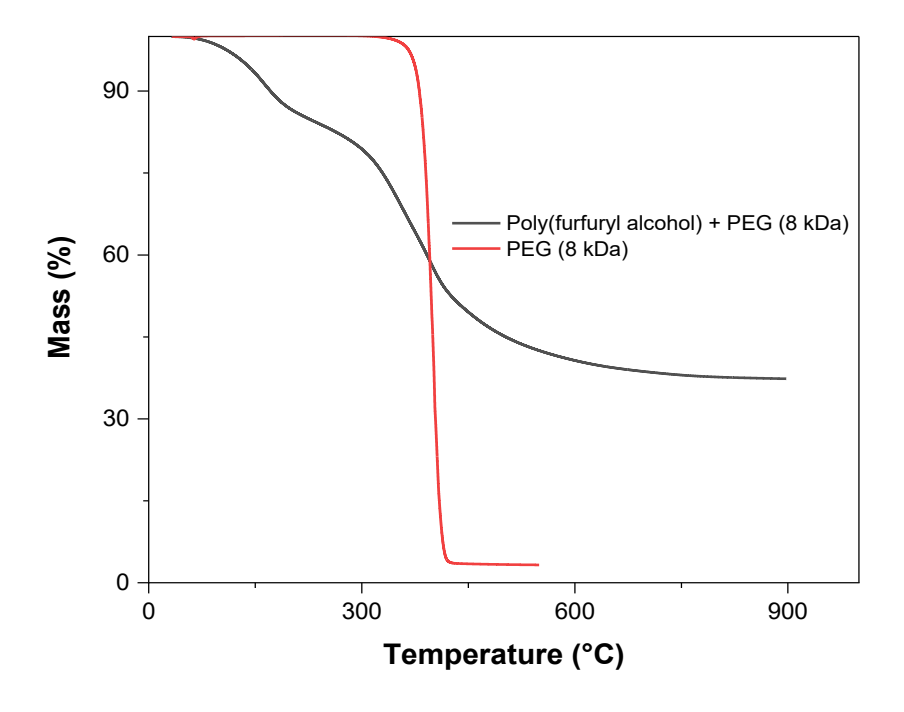


Figure 25. Thermogravimetric analysis (TGA) of P(FA)/PEG 8kDa (5 wt.%) mixture and PEG (8 kDa).

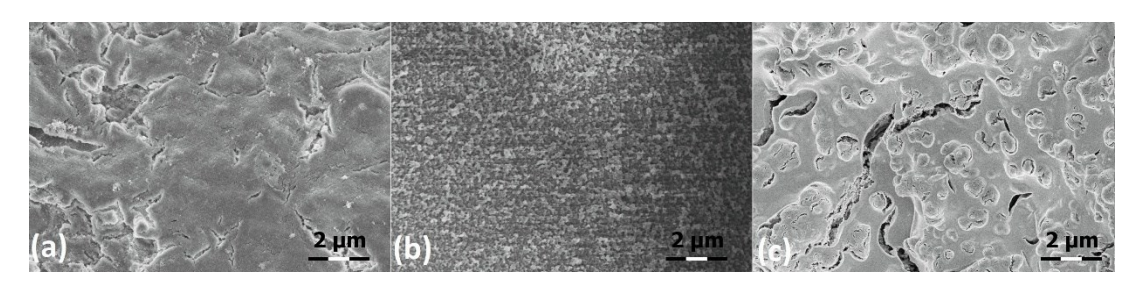


Figure 26. Effect of PEG (8 kDa) addition on the resulting carbon-coating surface (SEM images): (a) 0 wt.% PEG, (b) 5 wt.% PEG, (c) 15 wt.% PEG.

The nitrogen physisorption isotherms (77 K) of the carbon-coated foams prepared with different PEG contents are shown in Figure 27 and the corresponding textural parameters are summarized in Table 7. When no PEG or only a small amount (3 wt.%) was added, the isotherms were of type I with open hysteresis loops, typical of microporous carbons where nitrogen diffusion is restricted at 77 K [57,58]. Increasing the PEG content to 5 and 15 wt.% shifted the isotherms towards type IV, indicating the development of mesopores wider than 4 nm [35]. This trend is corroborated by the pore volume analysis (Table 7): the meso-to-micropore volume ratio increased from 0.12 in the PEG-free material

to 1.0 with 5 wt.% PEG, while the 15 wt.% PEG sample even suggested partial macroporosity formation. In contrast, the specific surface area decreased as mesoporosity became more dominant, consistent with a structural rearrangement of the carbon framework.

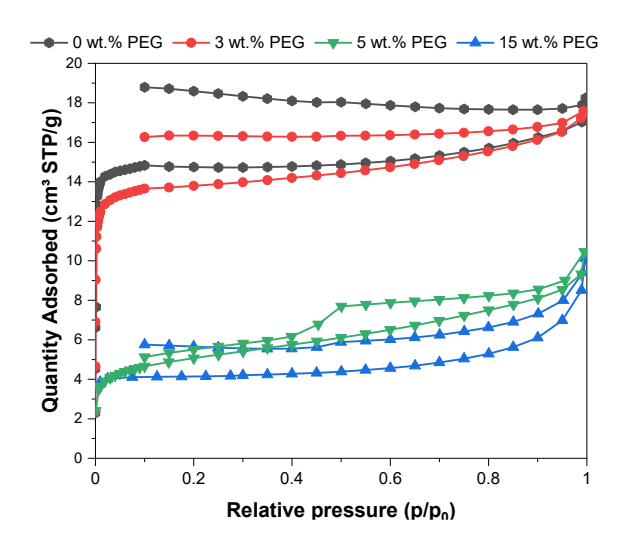


Figure 27. Nitrogen physisorption isotherms (77 K) recorded for carbon-coated aluminium foams using different PEG contents in the precursor polymer mixture (solid lines are guides for the eyes).

Table 7. Textural properties of carbon-coated aluminium foams prepared with different PEG contents in the precursor mixture.

PEG	DR surface areaa	BET area ^b	Pore volume ^c	Ratio meso/micro pore
(wt. %)	$(\mathbf{m}^2 \cdot \mathbf{g}^{-1})$	$(\mathbf{m}^2 \cdot \mathbf{g}^{-1})$	(cm ³ ·g ⁻¹)	volume (-)
0	69	47	0.024	0.12
3	63	46	0.023	0.24
5	20	17	0.012	1.00
15	No fitted	12	0.010	0.93

^a Dubinin-Radushkevich specific surface area, ^b Brunauer-Emmett-Teller specific surface area, ^c Cumulative pore volume (pore width ≤50nm).

The reduction conditions for the prepared catalysts were established by H₂-TPR measurements. Figure 28 displays the hydrogen consumption profile of the Ru/C solid foam catalyst synthesized with 5 wt.% PEG in the polymer precursor mixture. Two distinct hydrogen consumption maxima were identified: the first peak, at approximately 250 °C, is attributed to the reduction of ruthenium species, whereas the second peak is associated with the methanation of the carbon support, as confirmed by mass spectrometry. Based on these results, the reduction procedure was set at 300 °C with a heating ramp of 3 K·min⁻¹.

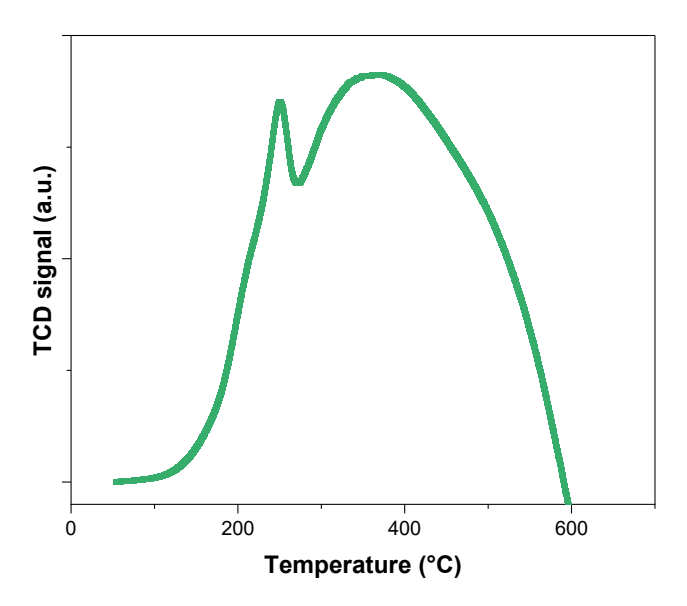


Figure 28. Hydrogen-TPR profile of the Ru/C solid foam catalyst prepared with 5 wt.% PEG in the polymer precursor mixture. TCD = thermal conductivity detector.

Ruthenium nanoparticles were deposited on carbon-coated foams prepared without and with 5 wt.% PEG in the polymer precursor mixture to evaluate the effect of induced mesoporosity on catalytic performance. Under the impregnation conditions described in Section 2.1., Ru loadings of 1.7 wt.% and 1.4 wt.% were obtained, respectively. Regarding the Ru nanoparticle size distribution, the introduction of mesoporosity improved the metal dispersion: the average particle size decreased from 3.6 nm (microporous carbon coating, Figure 8 of Article I [56]) to 2.8 nm (mesoporous carbon coating), as shown in the TEM micrographs in Figure 30 (d). Considering that sugar hydrogenation is a structure-sensitive reaction [63], the enhanced metal dispersion of the mesoporous catalyst translated into a higher activity for the hydrogenation of D-xylose. Consequently, this catalyst was selected for systematic kinetic experiments and kinetic modelling of xylose hydrogenation.

In contrast, a decrease in catalytic activity was observed after 200 h of operation in repeated semi-batch experiments (Figure 29). The primary cause of deactivation was attributed to nanoparticle agglomeration, as evidenced in the Figure 6 of Article III [64]. Nevertheless, the mesoporous catalyst retained its activity for twice as long as the purely microporous Ru/C foam. This improved stability can be ascribed to the spatial restriction exerted by mesopores confining the Ru nanoparticles, which hindered agglomeration, in agreement with the findings of Cattaneo et al. [65] for Ru-based catalysts supported on porous carbons.

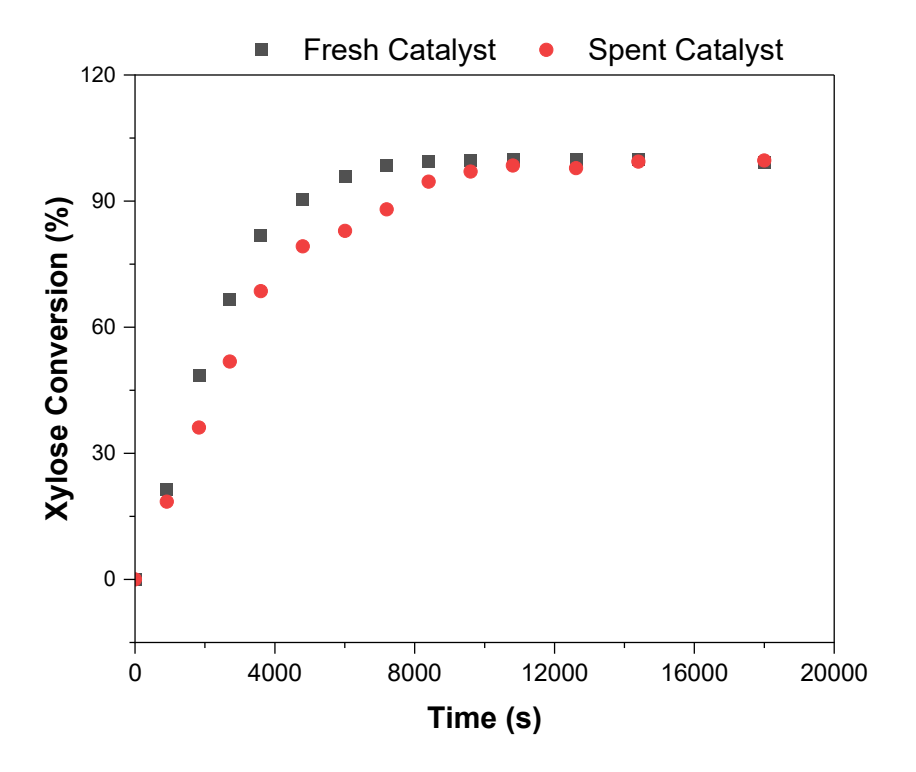


Figure 29. Decrease of catalytic activity in Ru/C solid foam (prepared with 5 wt.% PEG) after 200 h of use in subsequent semi-batch experiments. Conditions: 100 °C, 40 bar H₂, and 0.13 M xylose.

Figure 30 summarizes the main structural features of the Ru/C solid foam catalyst prepared with 5 wt.% PEG and employed in kinetic studies. The open-cell structure was preserved after carbon coating, which resulted in a continuous but thin layer of approximately $\sim \! 10~\mu m$ on the struts. This morphology ensured both mechanical stability and accessibility of the foam cells. In addition, the Ru nanoparticles displayed a narrow size distribution. The combination of a thin and homogeneous carbon coating with well-dispersed Ru nanoparticles provided an active and stable catalyst, suitable for systematic kinetic and transport investigations of xylose hydrogenation.

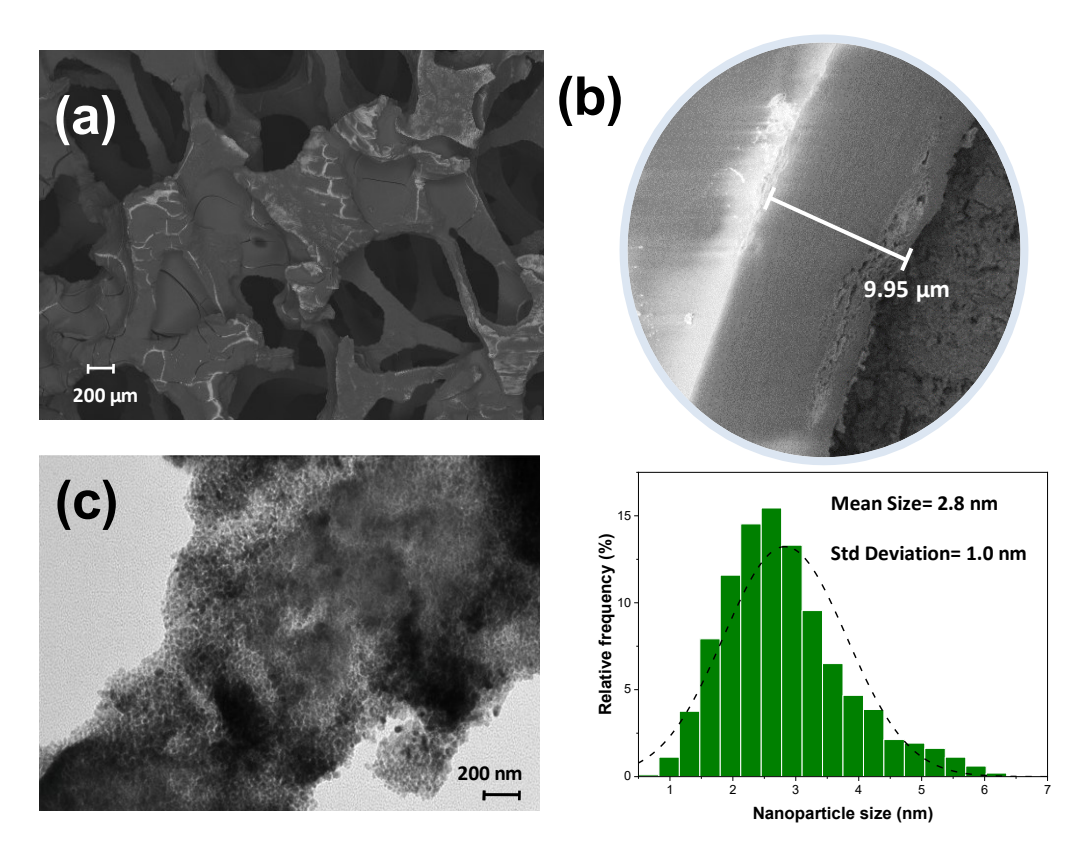


Figure 30. Key features of Ru/C solid foam catalysts: (a) SEM image showing foam morphology; (b) thickness of the carbon coating measured on struts (\sim 10 μ m); (c) representative TEM image of Ru nanoparticles; (d) histogram of nanoparticle size distribution (1000 counts).

3.3.2. Semi-batch experiment results

Kinetic studies in semi-batch mode were performed with the Ru/C foam catalyst prepared with 5 wt.% PEG, following the procedure described in Section 2.3. Figure 31 summarizes the influence of temperature (Figure 31(a)), hydrogen pressure (Figure 31(b)), and initial xylose concentration (Figure 31(c)) on the catalytic performance in xylose hydrogenation. As an illustration of the most prominent effect on xylitol selectivity, the impact of temperature is highlighted in Figure 31(d). A detailed analysis of the other variables is provided in Article III [64].

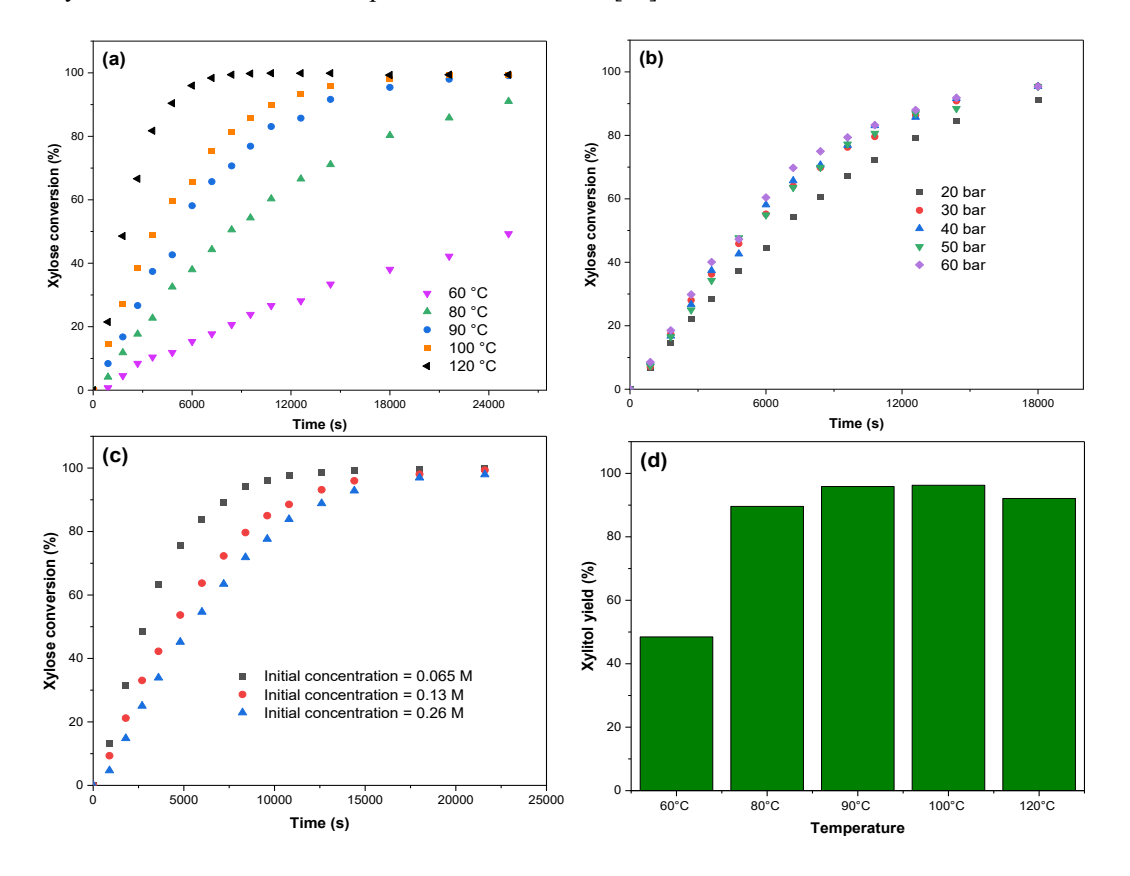


Figure 31. Effect of process parameters on the kinetics of D-xylose hydrogenation: (a) temperature effect at 40 bar H₂; (b) hydrogen-pressure effect at 90 °C; (c) effect of initial D-xylose concentration at 100 °C and 40 bar; (d) final xylitol yield after 7 h as a function of temperature at 40 bar.

A pronounced effect of temperature on the reaction rate was observed (Figure 31(a)). Below 80 °C, the hydrogenation proceeded slowly, whereas at temperatures above 100 °C the rate increased markedly. However, the selectivity towards xylitol decreased from 99 % at 60–90 °C to 92 % at 120 °C (Figure 31(d)), primarily due to the formation of arabitol as a by-product. These observations confirm that the side reactions leading to by-product formation are associated with higher activation energies than the main hydrogenation pathway. Therefore, the selection of the operating temperature in prospective industrial applications must strike a balance between productivity and selectivity, with moderate conditions (90–100 °C) providing an optimal compromise.

The effect of hydrogen pressure was comparatively minor, as observed in Figure 31(b). Increasing the pressure above 50 bar did not significantly enhance the hydrogenation rate, consistent with surface saturation of hydrogen on Ru sites under aqueous-phase conditions. Nevertheless, a slight improvement in xylitol selectivity was observed at higher pressures, suggesting that elevated hydrogen concentrations may suppress isomerization or degradation pathways.

The initial concentration of D-xylose also influenced the kinetics. Lower feed concentrations resulted in higher reaction rates, consistent with an effective reaction order in xylose of less than one (see Figure 31(c)). This behaviour indicates that adsorption of xylose molecules on the catalyst surface plays a determining role in the overall kinetics, with surface crowding at higher concentrations limiting the availability of active sites for hydrogenation.

Taken together, these results highlight that temperature exerts the strongest influence on both conversion and selectivity, while hydrogen pressure has only a secondary effect—especially beyond 40 bar—and substrate concentration primarily governs the reaction through adsorption phenomena. The optimal operating window therefore corresponds to intermediate xylose concentrations, temperatures around 90–100 °C, and hydrogen pressures above 30 bar, conditions under which high xylitol yields (>95 %) can be obtained with minimal by-product formation.

3.3.3. Intrinsic kinetic modelling

The mathematical models developed to describe the semi-batch experimental data were based on the following assumptions:

- The reaction proceeds under intrinsic kinetic control, with no internal or external mass transfer limitations due to high agitation and the thin catalyst layer, as confirmed by the Weisz–Hick's criterion.
- 2. The reaction volume remains constant since the withdrawn samples represented less than 6 % of the total.
- 3. Moreover, xylitol was considered the only reaction product due to the negligible formation of by-products.
- 4. Hydrogen solubility in the liquid phase follows Henry's law, with concentration proportional to gas-phase pressure [66].
- 5. Hydrogen undergoes dissociative adsorption but reacts in its molecular form, providing two atoms per sugar molecule.
- 6. Adsorption of xylitol is negligible due to its lower adsorption affinity [39].
- 7. The rate-determining step is the surface reaction between adsorbed sugar molecules and adsorbed hydrogen.

Regarding the reaction mechanism to derive the rate equation, two variants are explored: The non-competitive adsorption model and the semi-competitive adsorption model. The non-competitive adsorption models assume that due to the size differences between the sugar molecules and hydrogen, it is reasonable to suppose that they are adsorbed on separated active sites. This approach has been applied successfully to describe the hydrogenation of sugars [53,67], even if it is only an approximation from a physical viewpoint. On the other hand, a semi-competitive adsorption model has been proposed as a more realistic, though still hypothetical, description of the adsorption behaviour [68,69]. In this case, it is assumed that sugar molecules occupy the primary active sites of the catalyst surface, while smaller interstitial sites may remain available for hydrogen. The corresponding rate equations were derived based on these two mechanistic frameworks.

Non-competitive adsorption model

Scheme 1 illustrates the proposed surface reaction network according to the non-competitive adsorption model. In this approach, # denotes an active site for sugar adsorption (S), whereas # represents a site available for hydrogen adsorption.

$$S + * \longleftrightarrow S *$$

$$H_2 + 2 * ' \longleftrightarrow 2H * '$$

$$S * + 2H * ' \stackrel{k_X}{\longleftrightarrow} S_{OH} + * + 2 * '$$

Scheme 1. Reaction network for the non-competitive adsorption model.

The surface reaction is presumed to be rate-limiting. Therefore, the primary form of the rate expression can be written as:

$$\mathbf{r}_{\mathbf{X}} = \mathbf{k}_{*\mathbf{X}} \cdot \mathbf{C}_{*\mathbf{X}} \cdot \mathbf{C}_{*'\mathbf{H}}^{2} \tag{20}$$

The site balances for sugar and hydrogen adsorption sites are expressed as:

$$C_{*X} + C_{*} = C_{0}$$
 (21)

$$C_{*'H} + C_{*'} = C'_{0}$$
 (22)

where C_0 and C'_0 denote the total concentrations of adsorption sites available for sugar and hydrogen, respectively.

By applying the site balances together with the quasi-equilibrium hypothesis and rearranging, the final form of the rate equation is obtained (a detailed derivation is provided in Article III [64]):

$$r_{X} = \frac{\kappa_{X} \cdot C_{X} \cdot P_{H_{2}}}{\left(1 + K_{X} \cdot C_{X}\right) \cdot \left(1 + \sqrt{K_{H_{2}} \cdot P_{H_{2}}}\right)^{2}}$$
(23)

Here, κ_{X} is a merged parameter comprising the kinetic and adsorption constants, while K_{X} and $K_{H_{2}}$ are the adsorption parameters for xylose and hydrogen, respectively. The merged parameter κ_{X} is presumed to follow the Arrhenius and van't Hoff law, and its temperature dependence can be expressed as in Equation (24), referenced to 90 °C (363 K).

$$\kappa_{X} = \kappa_{X, 363 \text{ K}} \cdot e^{\frac{E_{A}}{R} \cdot \left(\frac{1}{T} - \frac{1}{T}\right)}$$
(24)

Semi-competitive adsorption model

For the semi-competitive adsorption model, it is assumed that the smaller molecule (hydrogen) occupies one primary site, whereas the larger molecules (sugars) require m adjacent sites for adsorption. Thus, the site balance for the primary adsorption sites can be expressed as:

$$m \cdot C_{*X} + C_{*H} + C_{*} = C_{0}$$
 (25)

The total concentration of primary sites, C_0 is distributed among three possibilities: sites occupied by hydrogen (C_{*H}), clusters of m sites occupied by sugars ($m \cdot C_{*X}$) and remaining vacant sites (C_*). If no sugars were present, the maximum number of potential clusters would be $\frac{C_0 - C_{*H}}{m}$. Not all these potential clusters are geometrically available because of steric hindrance and the random distribution of adsorbates. To account for this, a competitiveness factor α is introduced. This coefficient represents the maximum fraction ($\alpha \le 1$) of clusters that can be effectively occupied by sugars. Therefore, the balance of occupied and vacant clusters becomes:

$$C_{*X} + C_{*} = \frac{\alpha \cdot (C_0 - C_{*H})}{m}$$
 (26)

By applying the quasi-equilibrium hypothesis to the adsorption steps, and combining these relations with the site balance equations, the final rate expression (27) is obtained. A detailed step-by-step derivation is provided in Article III [64].

$$r_{X} = \frac{\kappa_{X} \cdot \alpha \cdot (1 + (1 - \alpha)) \cdot K_{X} \cdot C_{X})^{2} \cdot C_{X} \cdot P_{H_{2}}}{\left(1 + \sqrt{K_{H_{2}} \cdot P_{H_{2}}} + K_{X} \cdot C_{X} + (1 - \alpha) \cdot \sqrt{K_{H_{2}} \cdot P_{H_{2}}} \cdot K_{X} \cdot C_{X}\right)^{3}}$$
(27)

The merged parameter κ_{X} comprises the reaction constant and the adsorption parameters. It is assumed to follow the law of Arrhenius and van't Hoff. Thus, its temperature dependence can be described by Equation (24).

Mass balances and solution strategy

The mass balances of the components in the liquid phase can be written in a very simple manner because all the experiments were carried out in the kinetic regime using a thin catalyst layer and high stirring speed, thus avoiding the appearance of concentration gradients in the system:

$$\frac{dC_{X}}{dt} = -r_{X} \cdot \rho_{B} \tag{28}$$

$$\frac{dC_{X_{OH}}}{dt} = r_X \cdot \rho_B \tag{29}$$

The model was solved in Python by minimizing the objective function presented in Equation (30) with the Nelder-Mead optimization method. The LSODA solver was employed for the numerical solution of the ordinary differential Equations (28) and (29).

$$Q = \sum_{i=1}^{N_{\text{Exp}}} \sum_{j=1}^{N_{\text{C}}} \left(C_{i,j}^{\text{Exp}} - C_{i,j}^{\text{Calc}} \right)^{2}$$
(30)

Table 8 presents the fitting results for both the non-competitive and the semi-competitive adsorption models. Both approaches provided a satisfactory description of the experimental data. The estimated activation energies fall within the range reported for the hydrogenation of monomeric sugars on metallic catalysts. The adsorption parameter of xylose indicates a strong interaction of the substrate with the catalyst surface, whereas the parameter obtained for hydrogen is numerically lower because it combines two contributions: the solubility in the liquid phase (expressed by Henry's law constant) and the subsequent adsorption on the ruthenium active sites. The semi-competitive adsorption model exhibited a slightly higher coefficient of determination (R²) and lower parameter correlation (see Section 5.4.2, Article III [64]), which is reasonable since this approach offers a more realistic approximation of the molecular distribution on the catalyst surface compared with the limiting cases of fully non-competitive or competitive adsorption.

The concentration profiles obtained with the semi-competitive model are shown in Figure 32 and Figure 33 for the effects of initial xylose concentration and temperature, respectively. Additional profiles for the pressure effects can be found in Figure 14, Article III [64].

Table 8. Parameters estimated for the semi-competitive and non-competitive adsorption models.

Parameter	Non-competitive model	Semi-competitive model	Units
κx	2.0	6.8	$(\times 10^{-9}) \text{ m}^3 \cdot \text{kg}_{Ru}^{-1} \cdot \text{s}^{-1} \cdot Pa^{-1}$
E_{A}	4.18	4.21	(×10 ⁴) J·mol ⁻¹
K_{H_2}	7.2	3.5	$(\times 10^7) \mathrm{Pa}^{-1}$
K _X	9.13	5.17	(×10 ⁻³) m ³ ·mol ⁻¹
α	-	0.74	-
R ²	98.85	98.90	%
Q	7000	7200	mol²⋅m ⁻⁶

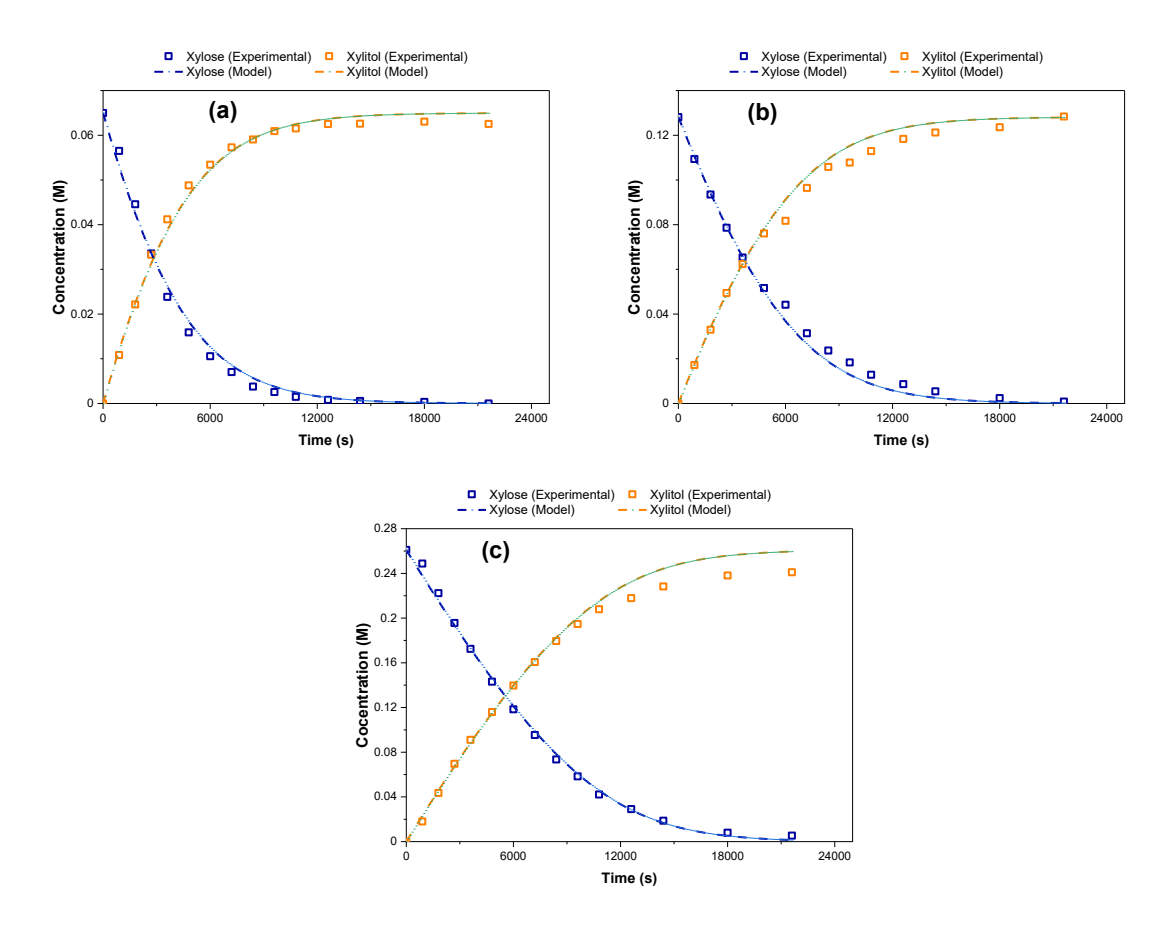


Figure 32. Modelling of D-xylose hydrogenation at $100\,^{\circ}$ C and $40\,$ bar H_2 , with initial concentrations of (a) $0.065\,$ M, (b) $0.13\,$ M, and (c) $0.26\,$ M (semi-competitive adsorption model).

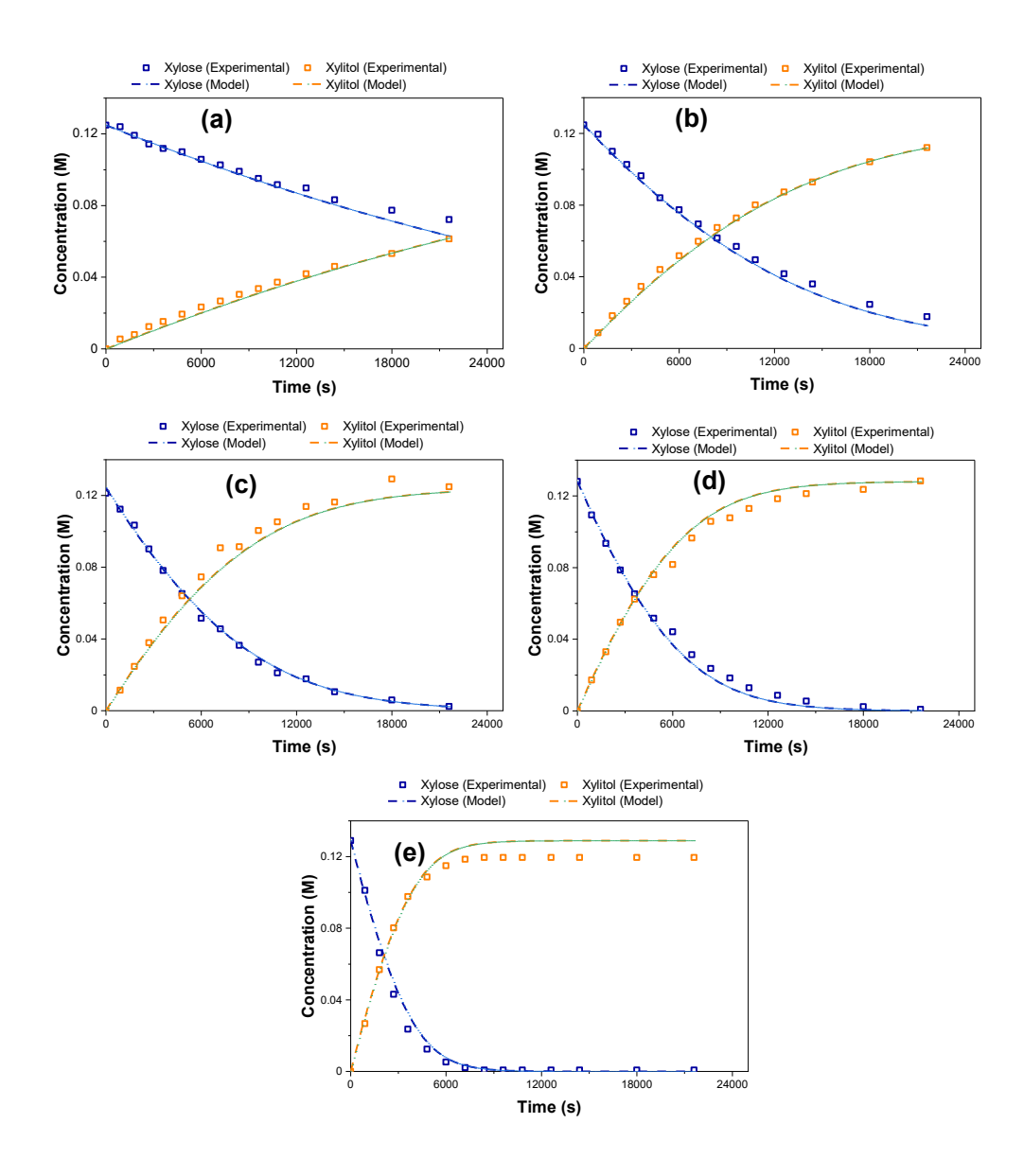


Figure 33. Modelling of D-xylose hydrogenation at 40 bar and (a) 60 °C, (b) 80 °C, (c) 90 °C, (d) 100 °C, (e) 120 °C (semi-competitive adsorption model).

As can be seen in Figure 32, the model describes well the effect of xylose concentration: higher initial concentrations lead to lower conversion profiles due to stronger substrate adsorption on the active sites. The model also predicts very successfully the influence of temperature on the hydrogenation process. The deviations observed at high conversion levels, particularly at 120 °C, can be attributed to the minor formation of by-products (Figure 33).

The semi-competitive adsorption model predicts a competitiveness factor of $\alpha=0.74$, indicating that up to 70 % of the primary adsorption sites on the ruthenium surface can be occupied by sugar molecules. Between the adsorbed sugar molecules, interstitial sites remain available for hydrogen adsorption, which is reasonable considering the size difference between sugar molecules and hydrogen. For the idealized case of spherical molecules (radius R) arranged on a flat surface, the ratio between the area occupied by the molecules and the total surface area is $\pi \cdot R^2/(2 \cdot R)^2 = \pi/4 = 0.785$ for a rectangular arrangement and $\pi/(2 \cdot \sqrt{3}) = 0.907$ for a triangular arrangement. These values can be regarded as the theoretical upper limits for site occupation.

To further assess the role of this parameter, the competitiveness factor was systematically varied between 0.1 and 1, while the other kinetic and adsorption parameters were kept fixed at the values obtained from the regression analysis. The simulation results, shown in Figure 34, reveal that the fraction of active sites maximally occupied by sugar molecules is well defined at $\alpha \approx 0.74$.

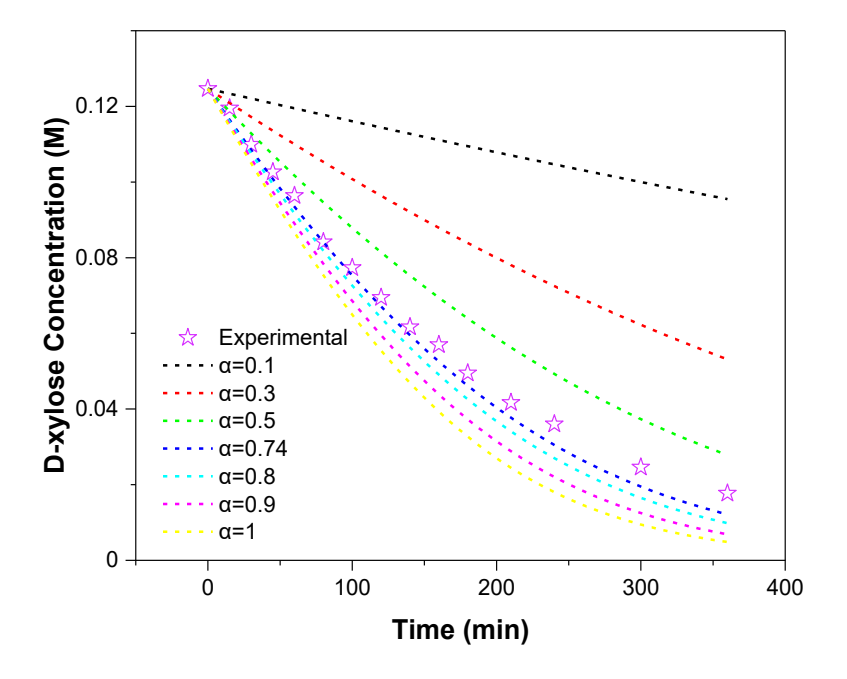


Figure 34. Effect of the competitiveness factor (α) on the predictions of the semi-competitive adsorption model for xylose hydrogenation at 40 bar and 80 °C.

3.3.4. Modelling of sugar mixtures

The hydrogenation of a sugar mixture composed of L-arabinose and D-galactose was investigated over Ru/C solid foam catalysts under semi-batch operation. These rare sugars can be derived from arabinogalactan, a hemicellulosic polysaccharide abundantly present in larch species (e.g., Larix sibirica) across the Northern Hemisphere. Arabinogalactan consists of a β-D-galactopyranose backbone with side chains of D-galactopyranose and L-arabinofuranose units. The average galactose-to-arabinose molar ratio is about 6:1, while the molar mass typically ranges from 20 to 100 kDa, corresponding to an average degree of polymerization of approximately 130–200 [70]. To examine the effect of composition, sugar mixtures with different galactose-to-arabinose molar ratios (0.5, 1, and 5) were prepared and hydrogenated at different temperatures (90, 100, and 120 °C).

A simultaneous catalytic process involving molecules that follow identical reaction mechanisms can be analyzed using double logarithmic plots of the reactant concentrations. Such plots are employed to confirm whether the parallel reactions proceed through a common mechanism[71,72]. The underlying principle is that the ratio of the reaction rates of the competing components is proportional to the ratio of their concentrations. Consequently, if the mixture behavior conforms to the assumed reaction mechanism on an ideal surface, a double logarithmic plot of the concentrations should yield a straight line.

In the case of L-arabinose and D-galactose following the mecanism of Scheme 1,

$$\frac{\mathbf{r}_{\mathbf{A}}}{\mathbf{r}_{\mathbf{G}}} = \frac{\mathbf{dC}_{\mathbf{A}}}{\mathbf{dC}_{\mathbf{G}}} = \frac{\kappa'_{\mathbf{A}} \cdot \mathbf{C}_{\mathbf{A}}}{\kappa'_{\mathbf{G}} \cdot \mathbf{C}_{\mathbf{G}}}$$
(31)

The relative reactivity of the components is denoted by the parameter σ as,

$$\sigma = \frac{\kappa'_{A}}{\kappa'_{G}} \tag{32}$$

Separation of variables and integrating Equation (31) with the integration limits [C_{A0} , C_{A}] and [C_{G0} , C_{G}] gives

$$\int_{CA0}^{CA} \frac{dC_A}{C_A} = \sigma \cdot \int_{CG0}^{CG} \frac{dC_G}{C_G}$$
(33)

Solving the integrals gives the logarithmic relationship,

$$-\operatorname{Ln}\left(\frac{\operatorname{C}_{A}}{\operatorname{C}_{A0}}\right) = -\sigma \cdot \operatorname{Ln}\left(\frac{\operatorname{C}_{G}}{\operatorname{C}_{G0}}\right) \tag{34}$$

The logarithm of the galactose concentration ratio $-Ln\left(\frac{C_G}{C_{G0}}\right)$ was plotted against the corresponding arabinose logarithm ratio $-Ln\left(\frac{CA}{C_{A0}}\right)$ obtained from the mixture experiments. For ideal mixtures, expression (34) predicts a linear relation, from which the relative reactivity factor (σ) can be determined. The value of σ is temperature dependent but independent of the initial reactant concentrations. As an example, the double logarithmic plot at 100 °C is presented in Figure 35. The results indicate that both sugars follow similar reaction mechanisms.

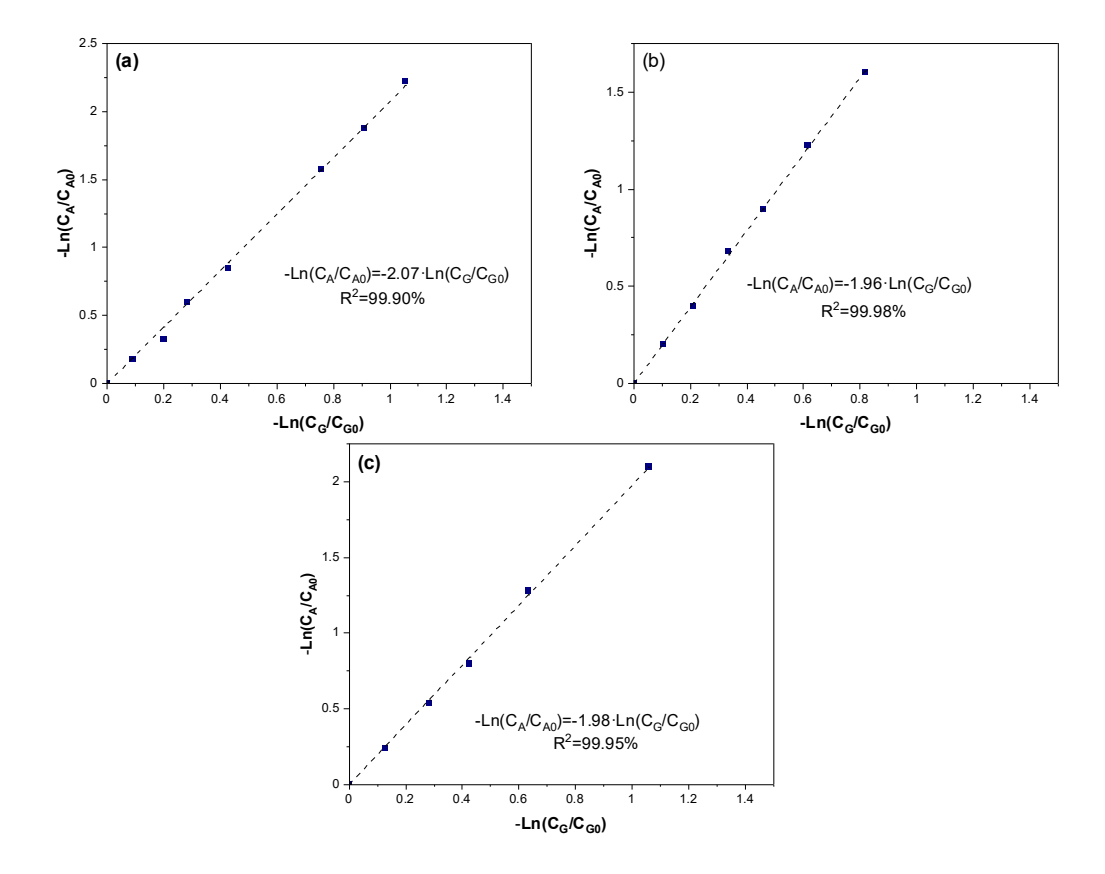


Figure 35. Double logarithmic plots of sugar mixtures at 100 °C and 20 bar: (a) D-galactose:L-arabinose = 0.5; (b) D-galactose:L-arabinose = 1; (c) D-galactose:L-arabinose = 5.

As shown in Table 9, the reactivity of L-arabinose is consistently higher than that of D-galactose across all initial molar ratios. However, the relative reactivity values varied with the initial galactose-to-arabinose ratio, suggesting some degree of non-ideality in the adsorption behavior. Comparable observations were reported by Sifontes et al. [73] for the hydrogenation of binary sugar mixtures using a commercial Ru/C powder catalyst.

Table 9. Relative reactivities at different initial molar ratios of D-galactose to L-arabinose.

Molar ratio (D-galactose:L-arabinose)	90 °C	100 °C	120 °C
0.5	1.73	2.07	1.67
1.0	2.03	1.96	1.70
5.0	1.77	1.98	1.78

In summary, the experimental data from the semi-batch hydrogenation experiments performed with the synthesized Ru/C solid foam catalyst could be described satisfactorily by mathematical models based on plausible reaction mechanisms, both for individual monomeric sugars and for their mixtures. The confirmed experimental observations reveal that sugar adsorption on ruthenium surfaces is a complex process. Monomeric sugars, such as xylose, coexist in aqueous solutions as mixtures of different isomeric forms, each exhibiting distinct reactivities and adsorption affinities that are further influenced by the reaction environment and process variables.

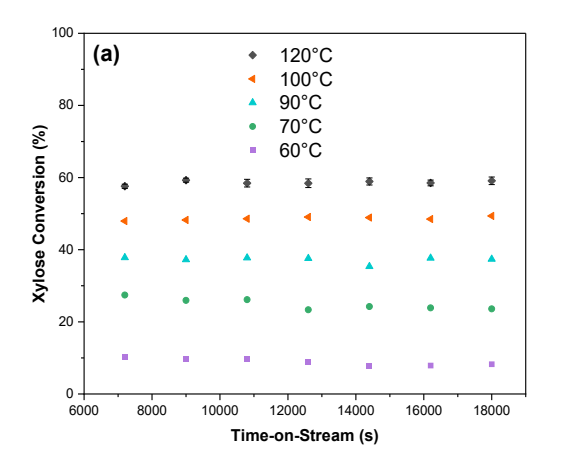
3.3.5. Continuous xylose hydrogenation

In this section, the results of the continuous xylose experiments performed with Ru/C solid foam catalysts in a parallel screening reactor are presented. The catalysts were synthesized following the procedure described in Section 2.3, employing 5 wt.% PEG in the polymer precursor mixture to tailor the carbon coating properties. The continuous hydrogenation experiments were conducted as outlined in Section 2.6, using the parallel screening reactor configuration to systematically evaluate the performance of the catalysts under different operating conditions.

Different process parameters—namely temperature, liquid flow rate, and feed concentration—were systematically evaluated to assess the performance of the Ru/C foam catalyst in continuous xylose hydrogenation. The catalyst showed stable behaviour during time-on-stream operation and good reusability, as confirmed by repeated experiments with the same catalyst.

The influence of temperature (60–120 °C) on xylose conversion and space-time yield (STY) is shown in Figure 36. Higher temperatures accelerate the intrinsic reaction rate, slightly increase the reactant diffusivity, and decrease the viscosity of the aqueous phase. Together, these effects enhance the transport of reactants to the catalyst surface, resulting in a steady rise in the STY with increasing temperature.

Because the experiments were conducted at a low liquid flow rate (0.25 mL·min⁻¹), external mass-transfer resistance was significant, which explains the lower conversions compared to those expected in the intrinsic kinetic regime. The xylitol selectivity ranged from 99 % to 94 %, with arabitol as the main by-product and xylulose found in small concentrations at the higher temperatures (≤1%). The xylitol selectivity improved at lower temperatures, which is consistent with the higher activation energy for the by-product formation. The near-neutral pH (5−7) and hydrogen-saturated conditions also suppressed the side reactions, favoring xylitol production [74].



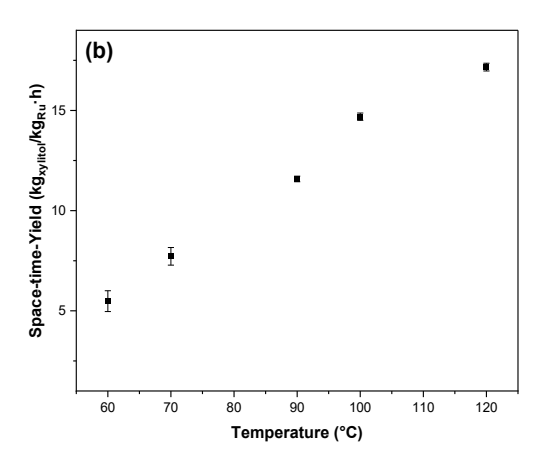


Figure 36. Effect of temperature on continuous xylose hydrogenation (0.13 M xylose, 0.25 mL·min⁻¹, 6.6 mL·min⁻¹ H₂, 20 bar): (a) xylose conversion vs. time-on-stream; (b) space–time yield (STY) at different temperatures.

Increasing the flow rate generally resulted in a lower conversion (Figure 37 (a)). Higher liquid velocities reduce the residence time in the catalytic bed, which is critical for relatively slow reactions such as sugar hydrogenation, where a sufficient contact time is required to achieve high single-pass conversions. In addition, higher flow rates increase the liquid holdup in the bed, effectively reducing the catalyst-to-liquid ratio.

Conversely, higher flow rates improve the liquid-solid mass transfer by increasing the Reynolds number and enhancing the wetting of the foam catalyst. The combination of these effects explains the behavior observed in Figure 37(b):

- STY rises as the flow rate increases from 0.25 to 0.75 mL min⁻¹, reflecting better catalyst utilization due to enhanced mass transfer.
- Beyond 0.75 mL·min⁻¹, the STY reaches plateaus because the residence time becomes too short, and maldistribution or partial channeling in the shallow, narrow bed might limit the effective catalyst use.
- At 1.25 mL·min⁻¹, the STY shows less stable behavior over time-on-stream.

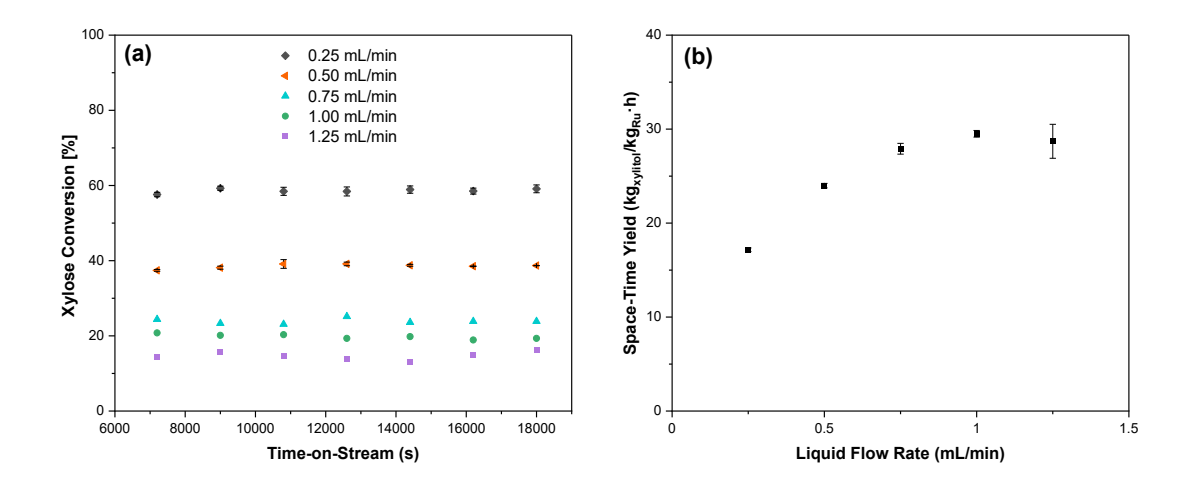


Figure 37. Effect of liquid flow rate on continuous xylose hydrogenation (120 °C, 0.13 M, 0.25 mL·min⁻¹, 6.6 mL·min⁻¹ H₂ at 20 bar): (a) xylose conversion vs. time-on-stream; (b) space–time yield (STY) at different liquid flow rates.

The effect of the feed concentration on xylose hydrogenation is presented in Figure 38. The conversion decreased with an increasing inlet concentration of xylose. This trend can be attributed to stronger product adsorption, which hinders the reactant access to active sites, and to higher liquid viscosity at higher concentrations. The increase in viscosity lowers the Reynolds number and therefore reduces the liquid—solid mass transfer. Additional contributing factors may include a decrease in hydrogen solubility.

Despite the lower conversion, the space-time yield (STY) increased as the feed concentration rose from 0.13 M to 0.26 M, reflecting the higher inlet throughput. At the feed concentration 0.39 M, the STY remained approximately constant, likely due to the combined effects of mass transfer limitations, reduced solubility, and reactant adsorption.

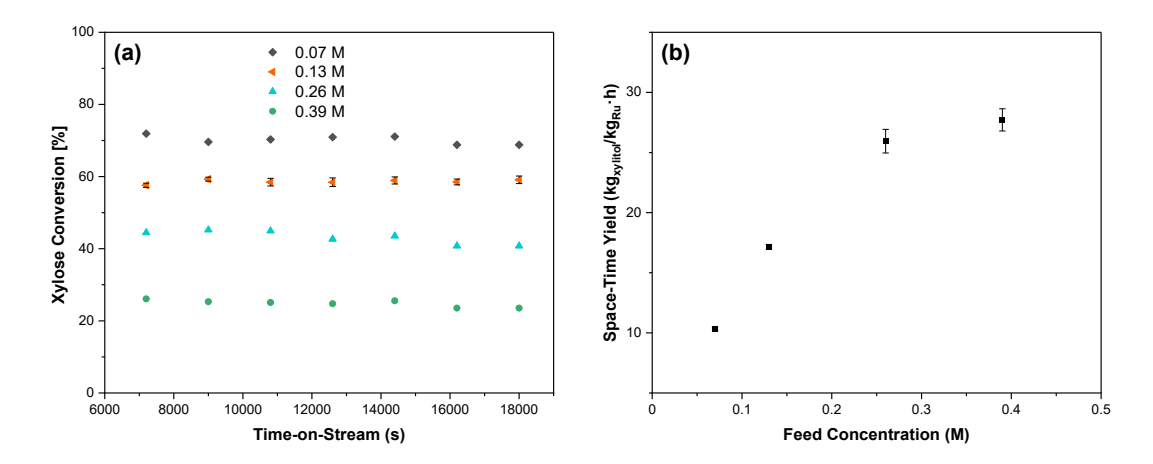


Figure 38. Effect of feed concentration on continuous xylose hydrogenation (120 °C, 0.25 mL·min⁻¹, 6.6 mL·min⁻¹ H₂ at 20 bar): (a) xylose conversion vs. time-on-stream; (b) space–time yield (STY) at different feed concentrations.

It can be concluded that temperature, feed concentration, and liquid flow rate are the key parameters governing the performance of xylose hydrogenation on Ru/C foam catalysts in trickle bed regime. Their effects arise from the interplay of intrinsic kinetics, mass transfer limitations, and hydrodynamics. Higher temperatures enhance the reaction rates, and diffusivity, but slightly decrease the product selectivity, while increased flow rates improve the liquid—solid mass transfer but reduce the residence time and effective catalyst concentration per liquid volume. The feed concentration directly affects both the kinetics and mass transfer by altering the viscosity, solubility, and adsorption. The combination of these factors determines the conversion, selectivity, and space-time yield. Efficient operation of foam-based trickle bed reactors therefore requires balancing temperature, liquid velocity, and feed concentration to minimize the mass-transfer limitations while maintaining a sufficiently long residence time and efficient catalyst utilization.

3.3.6. Modelling of continuous xylose hydrogenation

To complement the experimental studies, mathematical modelling was carried out to describe the continuous hydrogenation of xylose on Ru/C solid foam catalysts. Since hydrodynamic characteristics strongly affect the performance of trickle-bed reactors, liquid holdup and residence time distribution (RTD) measurements were first conducted to characterize the flow regime and quantify the extent of dispersion inside the catalytic beds. These experimental data provided the basis for the development of reactor models that couple intrinsic kinetics with transport phenomena. In particular, the modelling framework included the non-competitive adsorption rate expression together with axial dispersion and external gas—liquid and liquid—solid mass transfer resistances, allowing a quantitative interpretation of the continuous experiments under various operating conditions.

Residence Time distribution (RTD)

The residence time distribution (RTD) experiments displayed a clear evolution of the bed hydrodynamics with increasing liquid flow rate. At 0.25 mL·min⁻¹ (Figure 39 (a)), the reactor displayed the longest mean residence time (1344 s) and the broadest RTD (variance = 1641 s²), with an effective axial Péclet number of 35.7, indicative a relatively high axial dispersion. Increasing the flow rate to 0.50 mL min⁻¹ and 0.75 mL min⁻¹ (Figure 39 (b)-(c)) sharply reduced both the mean residence time (731 s and 504 s) and variance (396 s² and 198 s²), while raising the Péclet number to 43.9 and 41.5. These conditions correspond to a narrower residence time distribution and lower relative dispersion, as convective transport dominates over axial diffusion. At 1.00 mL·min⁻¹ (Figure 39 (d)), the mean residence time dropped to 360 s and the variance reached its minimum (120 s²), but the Péclet number decreased again to 35.4. This result reflects that, despite the narrow absolute RTD, the short residence time amplifies the relative influence of local maldistribution or bypassing, making axial dispersion comparatively more significant. Overall, the RTD analysis shows a transition from a broad, more dispersive flow pattern at low flow rates to convectively dominated behaviour at intermediate rates, followed by a high-flow regime where the reduced residence time increases the sensitivity to axial mixing.

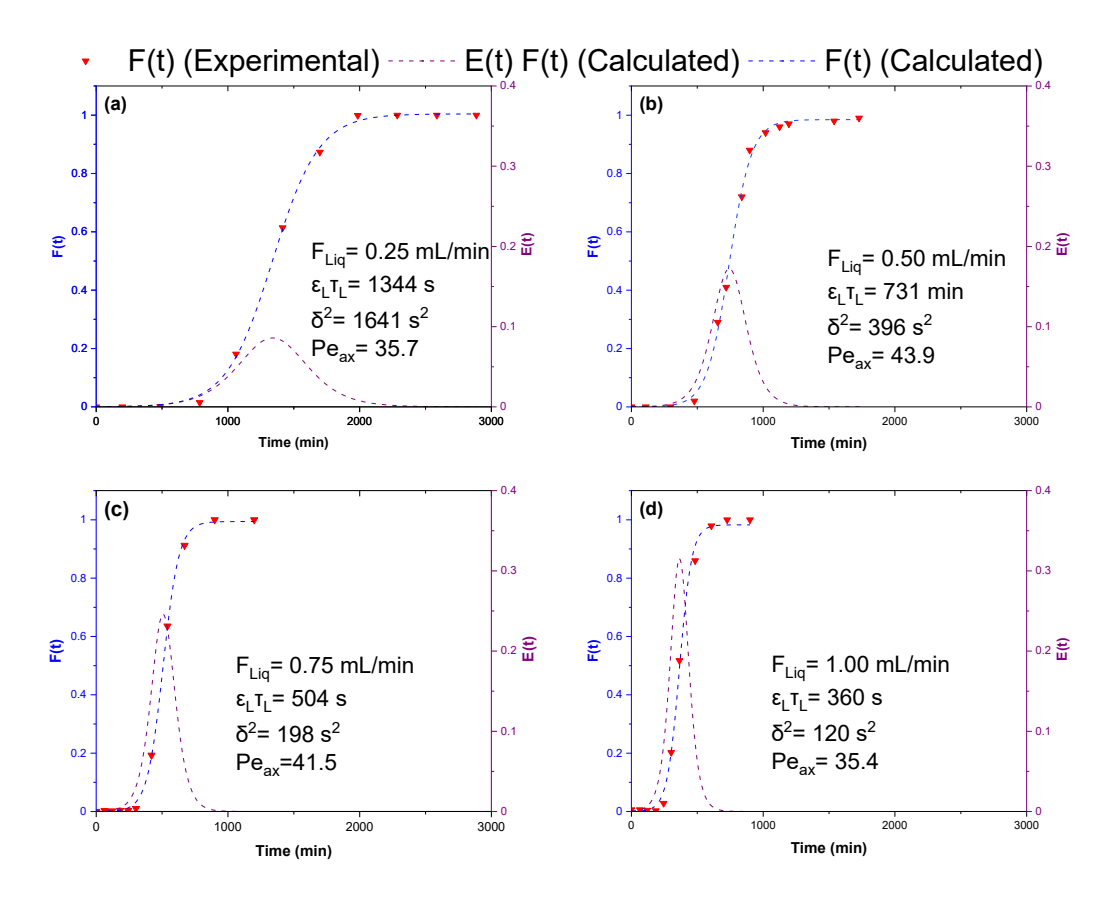


Figure 39. Step-response experiments at different liquid flow rates using xylitol as tracer. Conditions: 120 °C, 6.6 mL·min⁻¹ H₂ (20 bar).

Liquid holdup

The liquid holdup in the reactor packing as described in Section 2.3, as well as in a bed exclusively filled with Ru/C solid foam, was measured by a gravimetric water recirculation method (Section 2.5). The retained water at different liquid flow rates is presented in Figure 40(a). For the highest liquid flow rate (2.00 mL·min⁻¹), the bed was allowed to stabilize for a longer time to promote good wetting. As the flow rate decreased, a progressive reduction in retained water was observed for both configurations. Among the parameters studied, the liquid flow rate was the most decisive factor influencing the liquid holdup.

The solid foam catalyst bed retained more water than the mixed bed of sand and foams, which is expected because of the higher void fraction of the solid foams (~0.91) compared to quartz sand (~0.40), the latter reducing the overall liquid holdup. Nevertheless, both beds displayed similar variations with the process parameters.

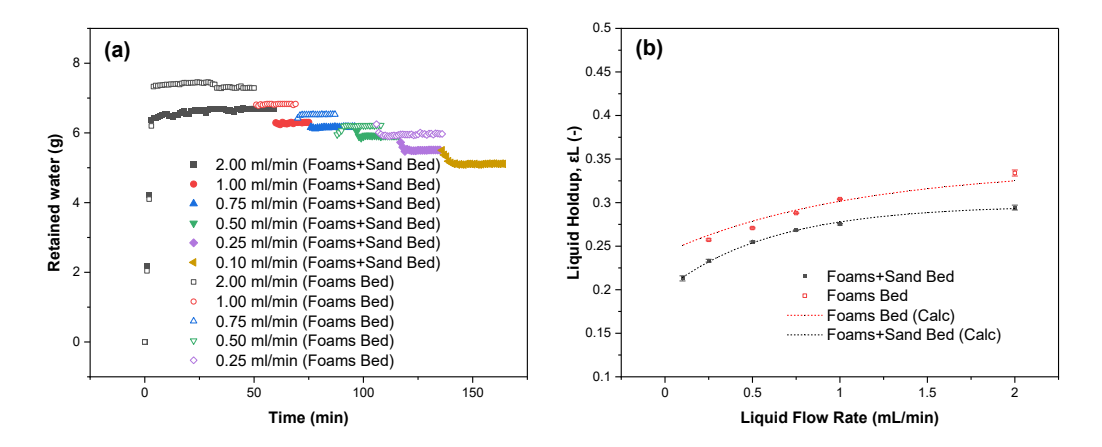


Figure 40. Liquid holdup in the total bed and in the Ru/C foam bed at 90 °C under 6.6 mL·min⁻¹ He at 20 bar:

(a) effect of liquid flow rate on retained water; (b) effect of liquid flow rate on liquid holdup.

The experimental data were fitted using the correlation proposed by García-Serna et al. [33] as presented in Equation (35), which accounts for the negative influence of increasing gas mass velocity (G') and the positive effects of pressure (P) and liquid mass velocity (L') on the liquid holdup. The fitting provided good agreement with the experiments, and the obtained parameters were consistent with those reported in the literature (listed in Table 10) [33].

$$\varepsilon_{L} = \left[a_{\varepsilon_{L}} + b_{\varepsilon_{L}} \left(1 - e^{-c_{\varepsilon_{L}} \cdot L'} \right) \right] \cdot \left(\frac{P}{G'} \right)^{d_{\varepsilon_{L}}}$$
(35)

Table 10. Fitting parameters for the liquid holdup correlation.

Reactor bed type	Parameter	Value
	a_{ϵ_L}	0.032
_	b_{ϵ_L}	0.013
Foams bed	c_{ϵ_L}	4.53
_	$d_{\epsilon_{\mathrm{L}}}$	0.100
-	R ²	95.8%
	a_{ϵ_L}	0.012
_	b_{ϵ_L}	0.006
Foam + Sand bed	c_{ϵ_L}	7.95
	$d_{\epsilon_{L}}$	0.140
	R ²	99.7%

Physical properties

The following physical properties were used to describe the experimental data obtained for the continuous xylose hydrogenation on Ru/C solid foam catalysts.

The correlation proposed by Sifontes et al. [66] (Equation (36)) was used to estimate the viscosity of aqueous sugar solutions as a function of the weight fraction (x_s) and temperature $(T/{}^{\circ}C)$. The coefficients reported for arabinose were adopted because of its structural similarity to its epimer, xylose.

$$\ln(\mu_{L}) = A_{\mu} \cdot \frac{x_{s}}{(T/^{\circ}C)} + B_{\mu} \cdot x_{s}^{2} + C_{\mu} \cdot x_{s} + D_{\mu} + \frac{E_{\mu}}{(T/^{\circ}C)} + \frac{F_{\mu}}{(T/^{\circ}C)^{2}}$$
(36)

The densities of the solutions under different experimental conditions were determined using Equation (37). As in the previous case, the coefficients estimated for arabinose were used [66].

$$\rho_{L} = -A_{\rho} \cdot T(^{\circ}C) \cdot x_{s} + B_{\rho} \cdot x_{s}^{2} + C_{\rho} \cdot x_{s} + D_{\rho} - E_{\rho} \cdot T(^{\circ}C) + F_{\rho} \cdot T(^{\circ}C)^{2}$$
(37)

The diffusion coefficients of xylose and hydrogen in water were calculated using the Wilke-Chang correlation [75]. In Equation (38), \mathfrak{D}_{i, H_2O} is the diffusion coefficient of the species i in water, $\phi_{H_2O} = 2.6$ is the association factor for water, M_{H_2O} is the molar mass of water, μ_{H_2O} is the water viscosity and V_{mi} is the normal boiling molar volume for hydrogen [76] or the effective molar volume

for xylose, which was estimated using the atomic group increments of Le Bas, as reported by Poling et al. [77].

$$\mathfrak{D}_{i, H_2O} = 7.4 \times 10^{-12} \cdot \frac{\left(\phi_{H_2O} \cdot M_{H_2O}\right)^{0.5} \cdot T}{\mu_{H_2O} \cdot V_{mi}^{0.6}}$$
(38)

The solubility of hydrogen in aqueous xylose solutions was calculated using the data collected by Wisniak et. al. [78], by adjusting the empirical correlation presented in Equation (39). The pressure exerts the strongest influence on hydrogen solubility, while the concentration effect is moderate and the effect of temperature is comparatively less pronounced, but hydrogen solubility increases slightly with increasing temperature. The values of the constants are: $\beta_0^{\text{sat}} = -1.45 \times 10^3$, $\beta_1^{\text{sat}} = 6.47 \times 10^3$ K, $\beta_2^{\text{sat}} = 20.30$, $\beta_3^{\text{sat}} = 4.72 \times 10^2$ K·L·mol⁻¹, $\beta_4^{\text{sat}} = -3.2 \times 10^{-3}$ bar⁻¹.

$$\left(\frac{C_{\text{M}_2}^{\text{sat}}}{L}\right) = \left(\frac{P}{\text{bar}}\right) \cdot e^{\left(\beta_0 + \frac{\beta_1^{\text{sat}}}{T} + \beta_2^{\text{sat}} \cdot \text{LnT} + \beta_3^{\text{sat}} \cdot \text{C}_x + \beta_4^{\text{sat}} \cdot \frac{\left(C_x / \frac{\text{mol}}{L}\right)}{T} + \beta_5^{\text{sat}} \cdot \left(\frac{P}{\text{bar}}\right)\right)} \tag{39}$$

On the other hand, key geometrical properties of the foam catalyst used in the modelling are summarized in Table 11.

Table 11. Relevant characteristics of the prepared Ru/C solid foam catalysts.

Catalyst property	Value
Catalyst mass (3 pieces)/ g	2.14
Carbon loading/ wt.%	35-40
Ru loading (based on carbon)/ wt.%	~1.0
Foam windows size /mm	1.21
Foam strut size/ mm	0.21
Carbon layer thickness/ μm	~101
Geometrical surface area/ m ² /m ³	2200 ²
Ru nanoparticle size/ nm	$2.8\pm1.0\ nm$
Void fraction/%	913

¹ Based on scanning electron microscopy images (see Figure 30).

² Estimate with the procedure described in Ref [79]

³ Based on apparent density measurements.

General model hypothesis

The general hypotheses adopted for the formulation of the kinetic and mass transport model are the following:

- Internal mass transfer limitations are negligible compared to external mass transfer resistances, due to the thin catalyst layer, as supported by previous simulations [80].
- The axial dispersion coefficient is assumed to be common to all species in the liquid phase and is taken as the value determined from step-response RTD studies.
- The liquid holdup in the catalytically active section is equal to the value measured by the gravimetric recirculation method.
- Radial concentration and velocity gradients were neglected due to the small reactor diameter.

Liquid-phase mass balance

The mass balance in the liquid phase is presented in Equation (40). The equation corresponds to the axial dispersion model incorporating both gas—liquid and liquid—solid external mass-transfer contributions. A detailed derivation of this expression is provided in Section 3.4 of Appendix I.

$$\frac{\varepsilon_{L}}{\text{Pe}} \cdot \frac{d^{2}C_{Li}}{dz^{2}} - \frac{dC_{Li}}{dz} + k_{GLi} \cdot a_{GL} \cdot \left(C_{Li}^{\text{sat}} - C_{Li}\right) \cdot \tau_{L} = N_{LSi} \cdot a_{LS} \cdot \tau_{L}$$
(40)

In Equation (40), the first term on the left-hand side accounts for the axial dispersion of species i along the dimensionless reactor coordinate z, with the liquid holdup ε_L and the Péclet number (Pe_{ax}) defined as in Equation (41).

$$Pe_{ax} = \frac{u \cdot L}{D_{x}}$$
 (41)

In Equation (41), u_z is superficial liquid velocity, L is the bed length, and D_z the axial dispersion coefficient. The mean residence time is given by

$$\tau_{L} = \frac{L}{u_{\perp}} \tag{42}$$

The second term in Equation (40) corresponds to convection. The gas-to-liquid transfer of species i is represented by the term $k_{GLi} \cdot a_{GL} \cdot \left(\begin{array}{c} C_{Li}^{sat} - C_{Li} \end{array} \right)$ where C_{Li}^{sat} is the equilibrium solubility of the species i in the liquid phase at the local interfacial temperature and pressure. In the present system, hydrogen is the only gas-phase component, and its saturation concentration was obtained from the selected solubility correlation as a function of temperature, pressure, and liquid composition. Finally, the

interfacial flux of species i from the liquid to the solid catalyst is denoted by N_{GLi} and a_{LS} are liquid—solid interfacial area-to-volume ratio, respectively.

If $Pe_{ax} \to \infty$, the plug flow reactor model is obtained indicated in Equation (43), with initial condition $C_{Lx} = C_{sln}$ and $C_{LH_2} = C_{H2}^{sat}$ at z = 0.

$$-\frac{dC_{Li}}{dz} + k_{GLi} \cdot a_{GL} \cdot (C_{Li}^{sat} - C_{Li}) \cdot \tau_{L} = N_{LSi} \cdot a_{LS} \cdot \tau_{L}$$

$$(43)$$

External mass transfer: liquid-solid interface

The mass balance for a component i in the liquid-solid interface of the catalyst is given by Equation (44), assuming steady-state conditions. Under this hypothesis, all the reactants that cross the liquid-solid interface are immediately consumed by the reaction.

$$v_{i} \cdot r \cdot \Delta m_{cat} + N_{LSi} \cdot \Delta A_{LS} = 0$$
(44)

The definitions of catalyst bulk density ($\rho_B = \frac{m_{Ru}}{V_L}$), which corresponds to the ratio between the mass of active metal (m_{Ru}) and the total liquid volume (V_L), along with surface area-to-volume ratio are introduced, yielding the relation,

$$v_{i} \cdot r \cdot \rho_{B} + N_{LSi} \cdot a_{LS} = 0 \tag{45}$$

Based on film theory and Fick's first law, the flux of species i (here N_{LSi}) through the stagnant liquid film can be expressed as Equation (46). The liquid-phase mass transfer coefficient is denoted as k_{LSi} representing the rate at which the species i is transported from the bulk liquid to the solid–liquid interface,

$$N_{LSi} = k_{LSi} \cdot \left(C_{Li} - C_{i}\right) \tag{46}$$

Combining (45) and (46) gives,

$$v_{i} \cdot r \cdot \rho_{B} + k_{LSi} \cdot a_{LS} \cdot \left(C_{Li} - C_{i}\right) = 0 \tag{47}$$

The dimensionless concentration y_i for species i is defined as the ratio between the concentration at the catalyst liquid interface, C_i and the concentration in the bulk liquid phase, C_{Li} as $y_i = \frac{C_i}{C_{Li}}$. Accordingly, Equation (47) can be expressed in the dimensionless form,

$$y_{i} - \frac{v_{i} \cdot r \cdot \rho_{B}}{k_{LSi} \cdot a_{LS} \cdot C_{Li}} = 1$$

$$(48)$$

Therefore, equations for xylose and hydrogen ($\nu_i = -1$) in the interface can be expressed by Equations (49) and (50), respectively using the non-competitive adsorption model (kinetic data from semi-batch experiments; see Section 3.3.3.)

$$y_{X} + \frac{\rho_{B} \cdot \kappa_{X,363 K} \cdot e^{\frac{E_{a}}{R} \cdot \left(\frac{1}{T} - \frac{1}{T}\right)} \cdot y_{X} \cdot C_{L_{H_{2}}} \cdot y_{H_{2}}}{\left(1 + K_{X} \cdot C_{L_{X}} \cdot y_{X}\right) \cdot \left(1 + \sqrt{C_{L_{H_{2}}} \cdot y_{H_{2}}}\right)^{2}} \cdot \frac{1}{k_{LSX} \cdot a_{LS}} = 1$$
(49)

$$y_{H_{2}} + \frac{\rho_{B} \cdot \kappa_{X, 363 K} \cdot e^{\frac{E_{a}}{R} \cdot \left(\frac{1}{T} - \frac{1}{T}\right)} \cdot C_{L_{x}} \cdot y_{X} \cdot y_{H_{2}}}{\left(1 + K_{x} \cdot C_{L_{x}} \cdot y_{X}\right) \cdot \left(1 + \sqrt{C_{L_{H_{2}}} \cdot y_{H_{2}}}\right)^{2}} \cdot \frac{1}{k_{LSH_{2}} \cdot a_{LS}} = 1$$
(50)

The liquid–solid mass transfer coefficient is inversely related to the thickness of the stagnant boundary layer, which is commonly expressed with the Sherwood number [81]. Mohammed et. al. [82] developed an effective liquid–solid correlation for foam packings in three-phase reactors (Equation (51)), using a modified electrochemical limiting-current method. Their formulation defines an effective Sherwood number based on the foam window diameter, d_w as the characteristic length and explicitly embeds foam geometry through the product $a_{geo} \cdot d_w \cdot \frac{1-\epsilon}{\epsilon}$ as well as gas hydrodynamics via a gas Reynolds term (Re_G). Importantly, the wetting efficiency ϕ is intrinsic to this correlation. Consequently, the effective volumetric liquid–solid coefficient can be estimated directly from Equation (52). With values of the constants: a=0.13, b=0.805, c=-0.89, d=-1.34.

$$\varphi \cdot Sh = a \cdot Re_L^b \cdot Re_G^c \left(a_{geo} \cdot d_w \cdot \frac{1 - \varepsilon}{\varepsilon} \right)^d$$
(51)

$$k_{LS} \cdot a_{LS} = \varphi \cdot k_{LS} \cdot a_{geo} = \varphi \cdot Sh \cdot \frac{\mathfrak{D}_{AB}}{d} \cdot a_{geo}$$
 (52)

External mass transfer: gas-liquid interface

Dedicated correlations for the gas–liquid (GL) mass transfer coefficient on solid open-cell foams are scarce and often unreliable in the low-interaction domain under reactive conditions [83,84]. Therefore, semi-empirical scaling was adopted, which preserves key hydrodynamic dependences while avoiding out-of-range correlations. The volumetric gas-liquid coefficient relates to the Sherwood number as $k_{GLi} = Sh \cdot \mathfrak{D}_{i,B}/L_c$. Consistent with boundary-layer/penetration theory, Equation (53) is used.

$$Sh_{average} \approx d \cdot Re_L^e \cdot Sc^f$$
 (53)

The expression (53) does not include the gas-phase Reynolds number (Re $_{\rm G}$), since gas-liquid mass transfer in packed/foam beds shows weak sensitivity to gas hydrodynamics in the low-interaction regime [85–87]. Therefore, it is possible to establish a relationship between the liquid-solid volumetric mass transfer coefficient of a given condition, $\begin{pmatrix} k_{\rm GLi} \cdot a_{\rm GL} \end{pmatrix}_{\rm j}$ with that of a reference $\begin{pmatrix} k_{\rm GLi} \cdot a_{\rm GL} \end{pmatrix}_{\rm REF}$ using the exponents predicted by the boundary layer theory for the gas-liquid interface with zero shear, and perfect slip [81], $e = \frac{1}{2}$, $f = \frac{1}{2}$:

$$\left(k_{GLi} \cdot a_{LG}\right)_{j} = \left(\frac{u_{j}}{u_{RFF}}\right)^{\frac{1}{2}} \cdot \left(\frac{\mathfrak{D}_{j}}{\mathfrak{D}_{REF}}\right)^{\frac{1}{2}} \cdot \left(k_{GLi} \cdot a_{GL}\right)_{REF}$$
(54)

Solution strategy

The Danckwerts' closed boundary condition (Equation (55)) is applied at the inlet of the catalyst bed for the liquid-phase mass balance. This condition establishes that the net convective inflow at z=0 is equal to the sum of the convective and dispersive fluxes at the same position,

$$C_{\text{feed}} = C_{\text{L0}} - \frac{1}{\text{Pe}_{\text{ax}}} \cdot \frac{\text{dC}_{\text{Li}}}{\text{dz}}$$
 (55)

At the outlet of the reactor (z=1), it is assumed that the concentration gradient vanishes, leading to the condition

$$\frac{dC_{N}}{dz} = 0 (56)$$

The first- and second-order spatial derivatives of the concentration are approximated using finite differences, as expressed in Equations (57) and (58):

$$\frac{dC_{Li}}{dz} = \frac{C_{L_{i+1}} - C_{L_{i-1}}}{2 \cdot \Lambda z}$$
 (57)

$$\frac{d^{2}C_{Li}}{dz^{2}} = \frac{C_{L_{i+1}} - 2 \cdot C_{L_{i}} + C_{L_{i-1}}}{\Delta z^{2}}$$
 (58)

The axial coordinate z is discretized into N nodes, and Equation (40) is rewritten accordingly, applying the corresponding boundary conditions.

The interface reaction rate in each node is approximated using a first-order Taylor expansion around the value at iteration k:

$$r\left(C_{j}\right) \approx r\left(C_{j}^{k}\right) + \frac{dr\left(C_{j}^{k}\right)}{dC}\left(C_{j}^{k+1} - C_{j}^{k}\right) \tag{59}$$

With the experimental steady-state xylose conversions, the value of $\left(k_{LGi} \cdot a_{LG}\right)_{REF}$ can be computed by minizine the objective function:

$$Q = \sum_{j=1}^{M} (X_{Exp} - X_{Calc})^{2}$$
 (60)

Where X_{Exp} and X_{Calc} are the experimental and calculated xylose conversion, respectively. The algorithmic for solving the system was implemented in Python following the steps described in Section 3.7. of Appendix I.

Modelling Results

The experimental data were fitted with the methodology described in the previous section to quantify the roles of gas-liquid (G-L) and liquid-solid (L-S) mass transfer using both the axial-dispersion model (ADM) and the plug flow model (PFR). The overall agreement is illustrated in Figure 41. Both models capture the experimental trends well. Because the dispersion effect on this system is significant but not dominant, including axial dispersion changes the predicted conversions only modestly; its impact becomes even less relevant at lower temperatures, where the Langmuir-Hinshelwood-type rate tends towards zero-order in xylose, so axial mixing has modest leverage on the outlet composition. Under the low-conversion conditions, the adsorption terms and interfacial transport become more influential.

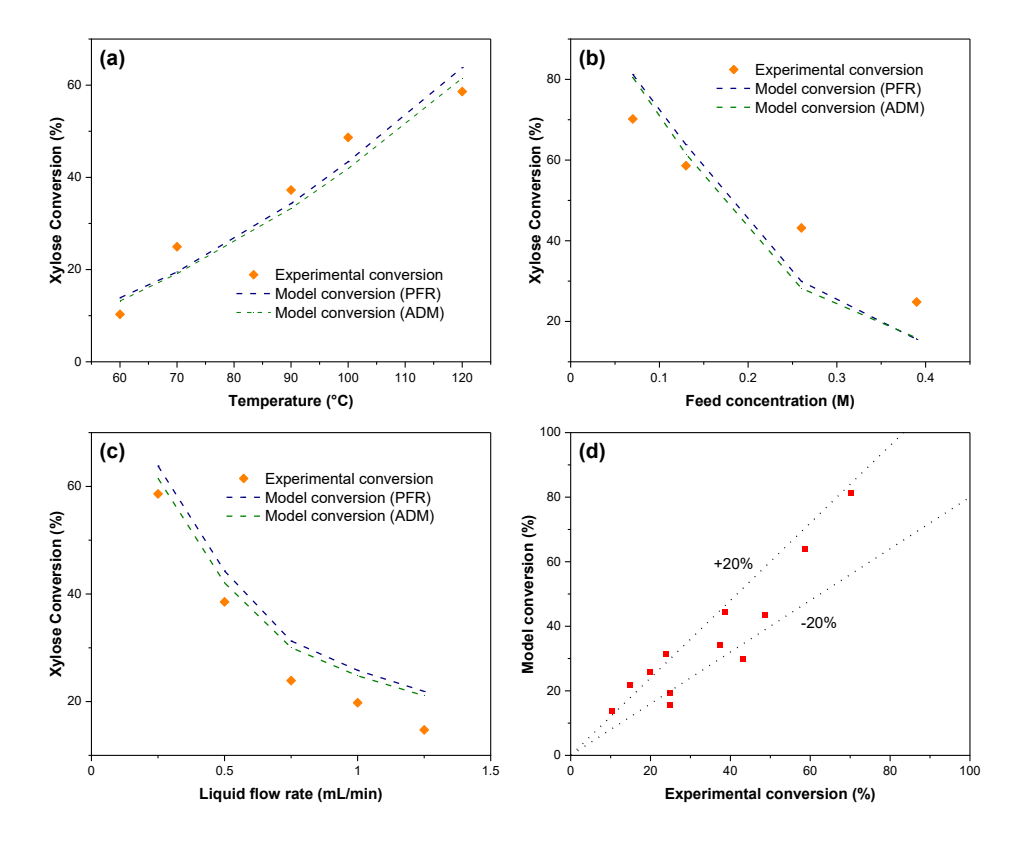


Figure 41. Experimental conversion data and model predictions (PFR and ADM), both including external gas—liquid (G–L) and liquid–solid (L–S) mass transfer resistances: (a) temperature effect (0.13 M xylose, 0.25 mL·min⁻¹ liquid, 6.6 mL·min⁻¹ H₂, 20 bar); (b) liquid flow-rate effect (120 °C, 0.13 M xylose, 6.6 mL·min⁻¹ H₂, 20 bar); (c) feed-concentration effect (120 °C, 0.25 mL·min⁻¹ liquid, 6.6 mL·min⁻¹ H₂, 20 bar); (d) parity plot of experimental versus predicted conversions.

The single fitted parameter in the PFR framework —the gas-liquid volumetric mass transfer coefficient $\left(k_{GLH_2}\cdot a_{GL}\right)_{REF}$ at 100 °C, 0.25 mL·min⁻¹ and 0.13 M xylose is shown in Table 12. The estimated value is 0.022 s⁻¹ (95% CI: 0.014–0.049 s⁻¹). This value is of the same order as the liquid-solid volumetric mass transfer coefficient for hydrogen $k_{LSH_2}\cdot a_{LS}$ predicted by the used correlation (Equation (51)), indicating that the gas-liquid mass transfer resistance is comparable to, and often slightly more limiting than, the liquid-solid mass transfer resistance for H_2 in this system. Similar observations have been reported previously for packed bed reactors operating at the low-interaction regime for sugar hydrogenation [83, 84].

Table 12. Fitting parameters for the axial dispersion model including gas-liquid and liquid-solid mass-transfer resistances.

Parameter	Value	95% CI	Units
$\left(\left. \mathrm{k}_{\mathrm{GLH}_{2}} \cdot \mathrm{a}_{\mathrm{GL}} \right)_{\mathrm{REF}} \right.$	0.022	[0.014, 0.049]	s ⁻¹
RMSE	6.60	-	%
\mathbb{R}^2	85.63	-	-

To interpret the mass transfer effect across various process conditions, Table 13 reports the resistances $\lambda = \frac{1}{k_i \cdot a_p} \text{ for L-S xylose } (\lambda_{LSX}), \text{ L-S hydrogen } (\lambda_{LSH_2}), \text{ and G-L hydrogen } (\lambda_{GLH_2}). \text{ From those values several trends can be deducted:}$

At a fixed flow rate, the mass transfer resistances increase as the temperature decreases, which is consistent with reduced diffusivities and lower Reynolds numbers (higher viscosity). However, the impact of the resistances on the overall reactor performance is less pronounced at lower temperatures because the reaction rate and interfacial driving forces are smaller, so even large resistances generate small fluxes as can be observed in the superficial concentration profiles displayed in Figure 42.

The mass transfer resistance shows a viscosity-driven trend: increasing the concentration raises the viscosity, which lowers the Reynolds and, therefore, Sherwood number, which reduces the overall mass transfer coefficient. In the present dataset this effect is non-monotonic (a decrease at 0.26 M followed by an increase at 0.39 M), suggesting competing effects of viscosity, wetting/area utilization, and changes in local driving forces.

Increasing the liquid flow rate enhances convection and typically reduces the film thickness, which increases the mass transfer coefficient but also can influence the effective wetting of the catalyst. Recent research on solid foams has shown that in co-current downflow, the wetting efficiency of the foam can be compromised by several hydrodynamic and design factors such as initial flow distribution, foam morphology and pre-wetting methods [86]. It is expected that under the screened conditions the wetness efficiency could have played an important role in the observed mass transfer limitations. Further research is necessary to separate the effects under reacting conditions.

Table 13. Mass-transfer resistances under the different experimental conditions predicted by the PFR model.

T (°C)	F (mL·min-1)	Cfeed (M)	$\lambda_{LSX}(s)$	$\lambda_{LSH_2}(s)$	$\lambda_{GLH_2}(s)$
60	0.25	0.13	117.5	57.5	62.1
70	0.25	0.13	94.3	46.1	56.9
90	0.25	0.13	62.9	30.8	48.8
100	0.25	0.13	52.4	25.6	45.6
120	0.25	0.13	37.3	18.3	40.3
120	0.5	0.13	21.4	10.5	28.5
120	0.75	0.13	15.4	7.5	23.3
120	1.00	0.13	12.2	6.0	20.2
120	1.25	0.13	10.2	5.0	18.0
120	0.25	0.07	34.2	16.7	40.3
120	0.25	0.26	43.1	21.1	40.3
120	0.25	0.39	48.1	23.5	40.3

Figure 42 displays the dimensionless concentration of the reacting species in the liquid-solid interface at different temperatures. In all cases the hydrogen interfacial fraction, y_{H_2} is lower than the xylose fraction, y_X . While the xylose profile remained relatively flat across the reactor length, with a slight decreasing trend near the outlet at higher temperatures, the hydrogen interfacial concentration showed a more complex behavior: it initially decreased in the vicinity of the reactor inlet, followed by a gradual increase toward the outlet.

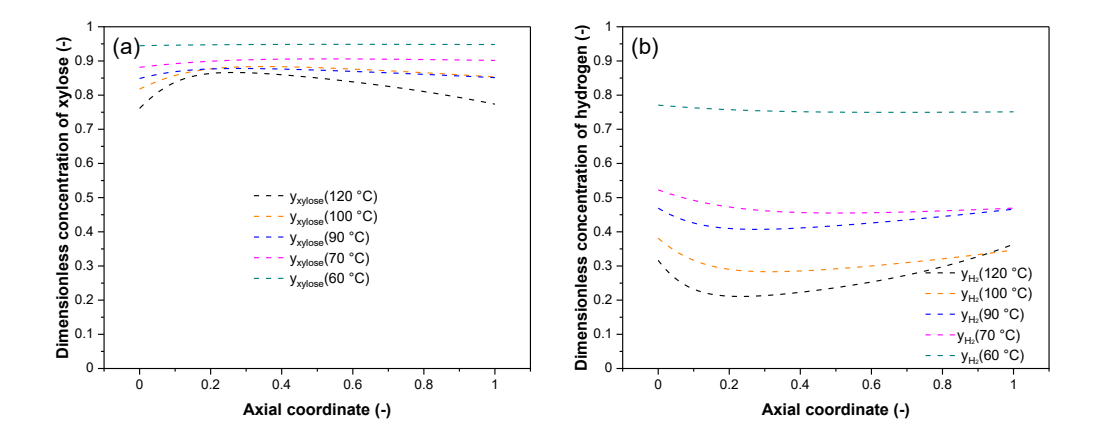


Figure 42. Dimensionless axial concentration profiles for (a) xylose and (b) hydrogen at the liquid–solid interface.

These trends can be explained by the form of the interfacial mass balances at the liquid-solid boundary and the liquid-gas mass transfer limitations. First, since the gas-liquid transfer of hydrogen is finite, the amount of dissolved hydrogen does not necessarily reach the maximal solubility, $C_{LH_2}^{sat}$ as shown below,

$$C_{LH_{2}} = C_{LH_{2}}^{sat} - \frac{r_{v}}{k_{GLH_{2}} \cdot a_{GL}}$$
(61)

Then, the balances in the liquid-solid interface, as described by Equations (49) and (50) can be rearranged substituting $r_v = r \cdot \rho_B$ and $\nu_i = -1$,

$$y_{H_{2}} = 1 - \frac{r_{v}}{k_{LSH_{2}} \cdot a_{LS} \cdot \left(C_{LH_{2}}^{sat} - \frac{r_{v}}{k_{GLH_{2}} \cdot a_{GL}}\right)}$$

$$y_{X} = 1 - \frac{r_{v}}{k_{LSX} \cdot a_{LS} \cdot C_{L_{v}}}$$
(62)

Then, dividing Equation (62) by (63) and rearranging gives the ratio

$$\frac{1 - y_{H_2}}{1 - y_X} = \frac{k_{LSx} \cdot C_{L_X}}{k_{LSH_2} \cdot \left(C_{LH_2}^{sat} - \frac{r_v}{k_{GLH_2} \cdot a_{GL}}\right)}$$
(64)

Since the bulk concentration of xylose generally is higher than that of hydrogen (due to limited hydrogen solubility and transport), $C_{Lx} > C_{LH_2}$ and the liquid-solid transport of hydrogen is higher than xylose transport, $k_{LSH_2} > k_{LSX}$. Therefore, the right-hand side of Equation (64) is generally larger than 1, which implies that $1 - y_{H_2} > 1 - y_X$, thus, $y_{H_2} < y_X$ as it is observed. The axial trends follow directly. Close to the reactor inlet C_{L_X} is high, so r_v is high too, then according to Equation (62), y_{H_2} should decrease. This explains the initial drop in y_{H_2} . Downstream, as xylose is consumed, C_{L_X} and r_v decrease; the hydrogen bulk concentration $C_{L_{H_2}}$ recovers toward $C_{LH_2}^{sat}$, causing the progressive increase of y_{H_2} .

At the highest temperatures, the reaction rate r_v is significantly enhanced, leading to a lower average y_X across the reactor (see Equation (63)). As the reaction progresses axially, the consumption of xylose reduces C_{L_X} , which in turn lowers the reaction rate r_v . According to Equation (63), this causes a slight increase in y_X . Towards the reactor outlet, however, the increasing interfacial hydrogen concentration y_{H2} enhances the reaction rate again, leading to a modest decrease in y_X as the reactor outlet is approached.

Overall, these results confirm that mass transfer resistance exerts a dominant influence on the performance of foam-based reactors under the studied downflow conditions. While the open structure of foams suppresses the retarding effect of internal diffusion and reduces the pressure drop, external resistances — particularly at the liquid–solid interface — remain critical. Future work should focus on configurations that alleviate these limitations, such as upflow operation [86] or improved liquid distribution strategies, to assess the potential of foam catalysts for continuous sugar hydrogenation under conditions closer to the regime of intrinsic kinetics.

4. CONCLUSIONS AND FUTURE PERSPECTIVES

This work explored novel catalytic technologies for the production of sugar alcohols from monomeric sugars derived from biomass, molecules with high relevance in the alimentary industry. The emphasis was placed on structured catalysts, specifically solid foams, with the long-term objective of enabling the transition from conventional semi-batch operation toward continuous processing. Three catalytic systems were studied: Ru-supported mesoporous molecular sieves, Raney-type solid foams, and Ru/C solid foam catalysts.

Ru catalysts supported on mesoporous molecular sieves (MCM-41, SBA-15, and MCF), synthesized as silicates and aluminosilicates, were tested for xylose hydrogenation in semi-batch mode. These materials exhibited high surface areas (above 600 m²·g⁻¹ for MCM-41) and well-developed mesoporosity. In general, the aluminosilicates displayed superior performance due to enhanced Ru loading and dispersion, attributed to stronger interactions between Ru species and the acidic surface induced by aluminium. The most active catalyst of the series, Ru/Al-MCM-41, reached activity comparable to a benchmark Ru/C catalyst. However, stability decreased upon reuse, mainly due to Ru leaching. Temperature-programmed reduction (TPR) suggested weaker metal—support interactions in Ru/MCM-41 compared with Ru/C, while XPS analysis indicated that Ru remained in a lower oxidation state in Ru/C, accounting for its superior stability. Despite these limitations, the technology remains promising, as tuning the Al/Si ratio could enable additional functionalities, such as one-pot hydrolysis—hydrogenation of hemicelluloses to sugar alcohols.

Novel Raney-type solid foam catalysts were evaluated for selective xylose hydrogenation. Although active and selective, the materials showed the typical stability drawbacks of sponge nickel. The main causes of deactivation were identified as metal leaching and adsorption of organic compounds on the active sites. Incorporating Mo as a promoter significantly enhanced both activity and stability, yielding a catalyst with approximately double the activity and markedly improved durability. Kinetic modelling confirmed this promoting effect, which was associated with stabilization of Ni in a lower oxidation state and reduced susceptibility to leaching. Furthermore, the NiMo foam catalyst exhibited improved stability in continuous operation, likely due to reduced accumulation of surface poisons and less attrition stress compared with semi-batch operation.

Ru/C solid foam catalysts were synthesized using a carbon coating method based on the polymerization of furfuryl alcohol on Al foams, followed by pyrolysis. The degree of crosslinking of poly(furfuryl alcohol) proved to be critical to forming a stable carbon layer. The introduction of mesoporosity by

adding PEG as a pore-forming agent enhanced Ru dispersion and catalyst stability. The catalyst prepared with 5 wt.% PEG displayed the best performance and was employed in both semi-batch and continuous operation, showing high activity, excellent selectivity, and good stability.

Extensive kinetic data for xylose hydrogenation were modelled using rate expressions based on plausible mechanistic hypotheses. Both the non-competitive and the more realistic semi-competitive adsorption models described the data satisfactorily. The semi-competitive model yielded a competitiveness factor of $\alpha \approx 0.74$, consistent with the predominance of sugar adsorption on the active sites, while still leaving interstitial sites accessible for hydrogen. This value was well defined across the experimental window and provided a realistic representation of the adsorption. Experiments with sugar mixtures (galactose and arabinose) further corroborated the non-ideal adsorption behaviour inherent to sugar hydrogenation.

Continuous experiments were modelled using a coupled kinetic-transport framework, incorporating hydrodynamics and holdup data. The fitted gas-liquid mass transfer coefficient was of the same order of magnitude as the liquid-solid coefficient for hydrogen, confirming that both steps are relevant under the low-interaction regime characteristic of laboratory-scale trickle bed operation at low flow rates. The analysis of resistances indicated that the liquid-solid transport of hydrogen becomes the most influential factor under these conditions, particularly at higher sugar concentrations and flow rates where liquid viscosity and wetting efficiency play a decisive role.

In general, this work underscores that while solid foams overcome the key limitations of conventional catalyst pellets, such as internal diffusion resistance and pressure drop, external transport resistances remain significant under laboratory-scale low-flow operation and may influence the observed kinetics. To fully exploit the potential of foam catalysts, future research should focus on reactor configurations and operating modes that enhance wetting and interfacial transport, such as upflow operation, improved liquid distribution, or intensified contacting strategies. Looking forward, the combination of tailored catalyst design with optimized reactor engineering holds great promise to unlock the full advantages of foam catalytic systems, enabling their application in industrial three-phase hydrogenation processes.

REFERENCES

- [1] B. Mallesham, D. Raikwar, D. Shee, The role of catalysis in green synthesis of chemicals for sustainable future, Advanced Functional Solid Catalysts for Biomass Valorization (2020) 1–37. https://doi.org/10.1016/B978-0-12-820236-4.00001-5.
- [2] M. Besson, P. Gallezot, C. Pinel, Conversion of biomass into chemicals over metal catalysts, Chem Rev 114 (2014) 1827–1870. https://doi.org/10.1021/cr4002269.
- [3] M.S. Akhtar, M.T. Naseem, S. Ali, W. Zaman, Metal-Based Catalysts in Biomass Transformation: From Plant Feedstocks to Renewable Fuels and Chemicals, Catalysts 15 (2025). https://doi.org/10.3390/catal15010040.
- [4] Ruppert, K. Weinberg, R. Palkovits, Hydrogenolysis goes bio: From carbohydrates and sugar alcohols to platform chemicals, Angewandte Chemie International Edition 51 (2012). https://doi.org/10.1002/anie.201105125.
- [5] C.D. Pinales-Márquez, R.M. Rodríguez-Jasso, R.G. Araújo, A. Loredo-Treviño, D. Nabarlatz, B. Gullón, H.A. Ruiz, Circular bioeconomy and integrated biorefinery in the production of xylooligosaccharides from lignocellulosic biomass: A review, Ind Crops Prod 162 (2021) 113274. https://doi.org/10.1016/J.INDCROP.2021.113274.
- [6] B. Zada, M. Chen, C. Chen, L. Yan, Q. Xu, W. Li, Q. Guo, Y. Fu, Recent advances in catalytic production of sugar alcohols and their applications, Sci China Chem 60 (2017) 853–869. https://doi.org/10.1007/s11426-017-9067-1.
- [7] J. V. Rissanen, H. Grénman, S. Willför, D.Y. Murzin, T. Salmi, Spruce Hemicellulose for Chemicals Using Aqueous Extraction: Kinetics, Mass Transfer, and Modeling, Ind Eng Chem Res 53 (2014) 6341–6350. https://doi.org/10.1021/IE500234T.
- [8] M. Ramos-Andrés, B. Aguilera-Torre, J. García-Serna, Hydrothermal production of high-molecular weight hemicellulose-pectin, free sugars and residual cellulose pulp from discarded carrots, J Clean Prod 290 (2021) 125179. https://doi.org/10.1016/J.JCLEPRO.2020.125179.

- [9] D.Y. Murzin, A. Duque, K. Arve, V. Sifontes, A. Aho, K. Eränen, T. Salmi, Catalytic Hydrogenation of Sugars, in: D. Murzin, O. Simakova (Eds.), Biomass Sugars for Non-Fuel Applications, The Royal Society of Chemistry, 2015: p. 89-1330. https://doi.org/10.1039/9781782622079-00089.
- [10] A. Chollangi, M.M. Hossain, Separation of proteins and lactose from dairy wastewater, Chemical Engineering and Processing: Process Intensification 46 (2007) 398–404. https://doi.org/10.1016/J.CEP.2006.05.022.
- [11] S.I. Martínez-Monteagudo, M. Enteshari, L. Metzger, Lactitol: Production, properties, and applications, Trends Food Sci Technol 83 (2019) 181–191. https://doi.org/10.1016/J.TIFS.2018.11.020.
- [12] H. Schiweck, A. Bär, R. Vogel, E. Schwarz, M. Kunz, C. Dusautois, A. Clement, C. Lefranc, B. Lüssem, M. Moser, S. Peters, Sugar Alcohols, in: Ullmann's Encyclopedia of Industrial Chemistry, John Wiley & Sons, Ltd, 2012. https://doi.org/10.1002/14356007.a25 413.pub3.
- [13] K.K. Mäkinen, J. Olak, S. Russak, M. Saag, T. Seedre, R. Vasar, T. Vihalemm, M. Mikelsaar, P.-L. Mäkinen, Polyol-combinant saliva stimulants: a 4-month pilot study in young adults, Acta Odontol Scand 56 (1998) 90–94.
- [14] P.T. Mattila, M.J. Svanberg, K.K. Mäkinen, M.L.E. Knuuttila, Dietary Xylitol, Sorbitol and D-Mannitol but not Erythritol Retard Bone Resorption in Rats, J Nutr 126 (1996) 1865–1870. https://doi.org/10.1093/JN/126.7.1865.
- [15] J. Zabner, M.P. Seiler, J.L. Launspach, P.H. Karp, W.R. Kearney, D.C. Look, J.J. Smith, M.J. Welsh. The osmolyte xylitol reduces the salt concentration of airway surface liquid and may enhance bacterial killing, Proceedings of the National Academy of Sciences 97 (2000) 11614–11619.
- [16] J. Kuusisto, J.P. Mikkola, P.P. Casal, H. Karhu, J. Väyrynen, T. Salmi, Kinetics of the catalytic hydrogenation of d-fructose over a CuO-ZnO catalyst, Chem. Eng. J. 115 (2005) 93–102. https://doi.org/10.1016/J.CEJ.2005.09.020.
- [17] J.P. Mikkola, H. Vainio, T. Salmi, R. Sjöholm, T. Ollonqvist, J. Väyrynen, Deactivation kinetics of Mo-supported Raney Ni catalyst in the hydrogenation of xylose to xylitol, Appl Catal A Gen 196 (2000) 143–155. https://doi.org/10.1016/S0926-860X(99)00453-6.

- [18] B.W. Hoffer, E. Crezee, F. Devred, P.R.M. Mooijman, W.G. Sloof, P.J. Kooyman, A.D. Van Langeveld, F. Kapteijn, J.A. Moulijn, The role of the active phase of Raney-type Ni catalysts in the selective hydrogenation of d-glucose to d-sorbitol, Appl Catal A Gen 253 (2003) 437–452. https://doi.org/10.1016/S0926-860X(03)00553-2.
- [19] K. Van Gorp, E. Boerman, C. V. Cavenaghi, P.H. Berben, Catalytic hydrogenation of fine chemicals: sorbitol production, Catal Today 52 (1999) 349–361. https://doi.org/10.1016/S0920-5861(99)00087-5.
- [20] B.W. Hoffer, E. Crezee, P.R.M. Mooijman, A.D. Van Langeveld, F. Kapteijn, J.A. Moulijn, Carbon supported Ru catalysts as promising alternative for Raney-type Ni in the selective hydrogenation of d-glucose, Catal Today 79–80 (2003) 35–41. https://doi.org/10.1016/S0920-5861(03)00040-3.
- [21] A. Gianetto, V. Specchia, Trickle-bed reactors: state of art and perspectives, Chem Eng Sci 47 (1992) 3197–3213. https://doi.org/10.1016/0009-2509(92)85029-B.
- [22] P.H. Ho, M. Ambrosetti, G. Groppi, E. Tronconi, R. Palkovits, G. Fornasari, A. Vaccari, P. Benito, Structured Catalysts-Based on Open-Cell Metallic Foams for Energy and Environmental Applications, Stud Surf Sci Catal 178 (2019) 303–327. https://doi.org/10.1016/B978-0-444-64127-4.00015-X.
- [23] H. Shen, Q. Ye, G. Meng, The Simplified Analytical Models for Evaluating the Heat Transfer Performance of High-Porosity Metal Foams, Int J Thermophys 39 (2018) 87. https://doi.org/10.1007/s10765-018-2405-0.
- [24] P.W.A.M. Wenmakers, J. Van Der Schaaf, B.F.M. Kuster, J.C. Schouten, Comparative Modeling Study on the Performance of Solid Foam as a Structured Catalyst Support in Multiphase Reactors, Ind Eng Chem Res 49 (2010) 5353–5366. https://doi.org/10.1021/IE900644E.
- [25] F. Lali, S. Gärtner, S. Haase, R. Lange, Preparation Method for Ruthenium Catalysts Supported by Carbon-Coated Aluminum Foams, Chem Eng Technol 38 (2015) 1353–1361. https://doi.org/10.1002/ceat.201400676.
- [26] S. Schimpf, M. Bron, P. Claus, Carbon-coated microstructured reactors for heterogeneously catalyzed gas phase reactions: influence of coating procedure on catalytic activity and selectivity, Chem. Eng. J. 101 (2004) 11–16. https://doi.org/10.1016/J.CEJ.2003.11.009.

- [27] A. Najarnezhadmashhadi, K. Eränen, S. Engblom, A. Aho, D. Murzin, T. Salmi, Continuous Hydrogenation of Monomeric Sugars and Binary Sugar Mixtures on a Ruthenium Catalyst Supported by Carbon-Coated Open-Cell Aluminum Foam, Ind Eng Chem Res 59 (2020) 13450–13459. https://doi.org/10.1021/ACS.IECR.0C01565.
- [28] T.A. Nijhuis, A.E.W. Beers, T. Vergunst, I. Hoek, F. Kapteijn, J.A. Moulijn, Preparation of monolithic catalysts, Catalysis Reviews 43 (2001) 345–380. https://doi.org/10.1081/CR-120001807.
- [29] C. Moreno-Castilla, O.P. Mahajan, P.L. Walker, H.J. Jung, M.A. Vannice, Carbon as a support for catalysts—III glassy carbon as a support for iron, Carbon N Y 18 (1980) 271–276. https://doi.org/10.1016/0008-6223(80)90050-0.
- [30] T. Vergunst, F. Kapteijn, J.A. Moulijn, Preparation of carbon-coated monolithic supports, Carbon N Y 40 (2002) 1891–1902. https://doi.org/10.1016/S0008-6223(02)00034-9.
- [31] F. Lali, G. Böttcher, P.M. Schöneich, S. Haase, S. Hempel, R. Lange, Preparation and characterization of Pd/Al2O3 catalysts on aluminum foam supports for multiphase hydrogenation reactions in rotating foam reactors, Chemical Engineering Research and Design 94 (2015) 365–374. https://doi.org/10.1016/J.CHERD.2014.08.012.
- [32] R.B. Mason, Effect of Aluminum Sulfate in the Sulfuric Acid Electrolyte on Anodic Polarization, J Electrochem Soc 103 (1956) 425. https://doi.org/10.1149/1.2430373.
- [33] J. García-Serna, G. Gallina, P. Biasi, T. Salmi, Liquid Holdup by Gravimetric Recirculation Continuous Measurement Method. Application to Trickle Bed Reactors under Pressure at Laboratory Scale, Ind Eng Chem Res 56 (2017) 13294–13300. https://doi.org/10.1021/ACS.IECR.7B01810.
- [34] C. Schlumberger, M. Thommes, Characterization of Hierarchically Ordered Porous Materials by Physisorption and Mercury Porosimetry—A Tutorial Review, Adv Mater Interfaces 8 (2021). https://doi.org/10.1002/ADMI.202002181.
- [35] G. Araujo-Barahona, N. Shcherban, K. Eränen, I. Kopa, I. Bezverkhyy, M. Martínez-Klimov, Z. Vajglová, A. Aho, J. García-Serna, T. Salmi, D.Y. Murzin, Ruthenium supported on silicate and aluminosilicate mesoporous materials applied to selective sugar hydrogenation: Xylose to xylitol, Chem. Eng. J. 485 (2024) 150019. https://doi.org/10.1016/J.CEJ.2024.150019.

- [36] A. Aho, S. Roggan, K. Eränen, T. Salmi, D.Y. Murzin, Continuous hydrogenation of glucose with ruthenium on carbon nanotube catalysts, Catal Sci Technol 5 (2015) 953–959. https://doi.org/10.1039/C4CY01088D.
- [37] P.O.J. Koopman, A.P.G. Kieboom, H. Van Bekkum, Induction effects in liquid phase hydrogenation catalyzed by ruthenium on carbon, Colloids and Surfaces 3 (1981) 1–12. https://doi.org/10.1016/0166-6622(81)80030-3.
- [38] S. Scirè, R. Fiorenza, A. Gulino, A. Cristaldi, P.M. Riccobene, Selective oxidation of CO in H2-rich stream over ZSM5 zeolites supported Ru catalysts: An investigation on the role of the support and the Ru particle size, Appl Catal A Gen 520 (2016) 82–91. https://doi.org/10.1016/J.APCATA.2016.04.011.
- [39] V.A. Sifontes Herrera, O. Oladele, K. Kordás, K. Eränen, J.P. Mikkola, D.Y. Murzin, T. Salmi, Sugar hydrogenation over a Ru/C catalyst, Journal of Chemical Technology & Biotechnology 86 (2011) 658–668. https://doi.org/10.1002/JCTB.2565.
- [40] M.A. Ramzan, R. Wischert, S.N. Steinmann, C. Michel, Toward a Realistic Surface State of Ru in Aqueous and Gaseous Environments, J Phys Chem Lett 14 (2023) 4241–4246. https://doi.org/10.1021/ACS.JPCLETT.3C00313.
- [41] E. Crezee, B.W. Hoffer, R.J. Berger, M. Makkee, F. Kapteijn, J.A. Moulijn, Three-phase hydrogenation of d-glucose over a carbon supported ruthenium catalyst—mass transfer and kinetics, Appl Catal A Gen 251 (2003) 1–17. https://doi.org/10.1016/S0926-860X(03)00587-8.
- [42] T.N. Pham, A. Samikannu, A.R. Rautio, K.L. Juhasz, Z. Konya, J. Wärnå, K. Kordas, J.P. Mikkola, Catalytic Hydrogenation of d-Xylose Over Ru Decorated Carbon Foam Catalyst in a SpinChem® Rotating Bed Reactor, Top Catal 59 (2016) 1165–1177. https://doi.org/10.1007/S11244-016-0637-4.
- [43] T. Ennaert, S. Feys, D. Hendrikx, P.A. Jacobs, B.F. Sels, Reductive splitting of hemicellulose with stable ruthenium-loaded USY zeolites, Green Chemistry 18 (2016) 5295–5304. https://doi.org/10.1039/C6GC01439A.

- [44] G. Araujo-Barahona, M. De Simone, C. Brunberg, K. Eränen, A. Reinsdorf, M. Roos, J. García-Serna, V. Russo, D.Y. Murzin, T. Salmi, Solid Raney-type Ni foam catalysts for xylitol production: Continuous and batch operation, Appl Catal A Gen 701 (2025) 120324. https://doi.org/10.1016/j.apcata.2025.120324.
- [45] M. Besson, P. Gallezot, Deactivation of metal catalysts in liquid phase organic reactions, Catal Today 81 (2003) 547–559. https://doi.org/10.1016/S0920-5861(03)00153-6.
- [46] Z. Fang, H. Fan, X. Zhao, G. Lin, B. Li, J. Wang, X. Lu, W. Yang, M. Li, W. Song, J. Fu, Unveiling the nature of glucose hydrogenation over Raney Ni: DFT and AIMD simulations, Appl Catal A Gen 667 (2023) 119462. https://doi.org/10.1016/J.APCATA.2023.119462.
- [47] B. García, J. Moreno, J. Iglesias, J.A. Melero, G. Morales, Transformation of Glucose into Sorbitol on Raney Nickel Catalysts in the Absence of Molecular Hydrogen: Sugar Disproportionation vs Catalytic Hydrogen Transfer, Top Catal 62 (2019) 570–578. https://doi.org/10.1007/s11244-019-01156-3.
- [48] J.C. Klein, D.M. Hercules, Surface analysis by x-ray photoelectron spectroscopy and Auger electron spectroscopy of molybdenum-doped Raney nickel catalysts, Anal Chem 56 (1984) 685–689. https://doi.org/10.1021/ac00268a022.
- [49] H. Lei, Z. Song, D. Tan, X. Bao, X. Mu, B. Zong, E. Min, Preparation of novel Raney-Ni catalysts and characterization by XRD, SEM and XPS, Appl Catal A Gen 214 (2001) 69–76. https://doi.org/10.1016/S0926-860X(01)00481-1.
- [50] G. V Golubkova, I.N. Bazanova, V.P. Gostikin, L.G. Nischenkova, O.I. Lomovsky, Mechanochemical promotion with molybdenum and catalytic activity of skeletal nickel catalysts in hydrogenation reactions, Reaction Kinetics and Catalysis Letters 67 (1999) 169–175. https://doi.org/10.1007/BF02475844.
- [51] D.Yu. Murzin, T. Salmi, Dynamic Catalysis in Catalytic Kinetics. 497–587. Second Edition. Elsevier, Amsterdam, 2016. https://doi.org/10.1016/B978-0-444-63753-6.00009-9.
- [52] T. Salmi, D.Yu. Murzin, J. Wärnå, J.-P. Mikkola, J. Aumo, J. Kuusisto, Modeling and Optimization of Complex Three-Phase Hydrogenations and Isomerizations under Mass-Transfer Limitation and Catalyst Deactivation, in: S.R. Schmidt (Ed.), Catalysis of Organic Reactions, 1st ed., CRC Press, 2006: pp. 187–196. https://doi.org/10.1201/9781420007794-31.

- [53] J.P. Mikkola, T. Salmi, R. Sjöholm, Kinetic and Mass-transfer Effects in the Hydrogenation of Xylose to Xylitol, Stud Surf Sci Catal 122 (1999) 351–358. https://doi.org/10.1016/S0167-2991(99)80166-9.
- [54] A. Najarnezhadmashhadi, J. Wärnå, K. Eränen, H.L. Trajano, D. Murzin, T. Salmi, Modelling of kinetics, mass transfer and flow pattern on open foam structures in tubular reactors: Hydrogenation of arabinose and galactose on ruthenium catalyst, Chem Eng Sci 233 (2021) 116385. https://doi.org/10.1016/J.CES.2020.116385.
- [55] N. Burgos, M. Paulis, M. Montes, Preparation of Al₂O₃/Al monoliths by anodisation of aluminium as structured catalytic supports, J Mater Chem 13 (2003) 1458–1467.
- [56] G. Araujo-Barahona, K. Eränen, J.P. Oña, D. Murzin, J. García-Serna, T. Salmi, Solid Foam Ru/C Catalysts for Sugar Hydrogenation to Sugar Alcohols —Preparation, Characterization, Activity, and Selectivity, Ind Eng Chem Res 61 (2022) 2734–2747. https://doi.org/10.1021/acs.iecr.1c04501.
- [57] E.M. Cepollaro, D. Caputo, S. Cimino, N. Gargiulo, L. Lisi, Synthesis and Characterization of Activated Carbon Foam from Polymerization of Furfuryl Alcohol Activated by Zinc and Copper Chlorides, C (Basel) 6 (2020) 45. https://doi.org/10.3390/c6030045
- [58] A. Zaharopoulou, S.N. Yannopoulos, T. Ioannides, Carbon membranes prepared from poly (Furfuryl Alcohol–Furfural) precursors: effect of FeCl₃ additive, C (Basel) 6 (2020) 53. https://doi.org/10.3390/c6030053
- [59] E. Lorenc-Grabowska, P. Rutkowski, Tailoring mesoporosity of poly(furfuryl alcohol)-based activated carbons and their ability to adsorb organic compounds from water, J Mater Cycles Waste Manag 20 (2018) 1638–1647. https://doi.org/10.1007/s10163-018-0733-6.
- [60] V. Sricharoenchaikul, C. Pechyen, D. Aht-Ong, D. Atong, Preparation and Characterization of Activated Carbon from the Pyrolysis of Physic Nut (Jatropha curcas L.) Waste, Energy and Fuels 22 (2007) 31–37. https://doi.org/10.1021/EF700285U.
- [61] D.S. Lafyatis, J. Tung, H.C. Foley, Poly(furfuryl alcohol)-derived carbon molecular sieves: dependence of adsorptive properties on carbonization temperature, time, and poly (ethylene glycol) additives, Ind Eng Chem Res 30 (1991) 865–873.

- [62] M.S. Strano, H. Agarwal, J. Pedrick, D. Redman, H.C. Foley, Templated pyrolytic carbon: the effect of poly(ethylene glycol) molecular weight on the pore size distribution of poly(furfuryl alcohol)-derived carbon, Carbon N Y 41 (2003) 2501–2508. https://doi.org/10.1016/S0008-6223(03)00326-9.
- [63] I.L. Simakova, Y.S. Demidova, E. V Murzina, A. Aho, D.Yu. Murzin, Structure Sensitivity in Catalytic Hydrogenation of Galactose and Arabinose over Ru/C Catalysts, Catal Letters 146 (2016) 1291–1299. https://doi.org/10.1007/s10562-016-1752-3.
- [64] G. Araujo-Barahona, A. Goicoechea-Torres, K. Eränen, R.M. Latonen, T. Tirri, A. Smeds, D. Murzin, J. García-Serna, T. Salmi, Kinetic studies of solid foam catalysts for the production of sugar alcohols: Xylitol from biomass resources, Chem Eng Sci 281 (2023) 119130. https://doi.org/10.1016/J.CES.2023.119130.
- [65] S. Cattaneo, M. Stucchi, G.M. Veith, L. Prati, D. Wang, W. Wang, A. Villa, Ru supported on micro and mesoporous carbons as catalysts for biomass-derived molecules hydrogenation, Catal Today 357 (2020) 143–151. https://doi.org/10.1016/J.CATTOD.2019.05.009.
- [66] V.A. Sifontes Herrera, D.E. Rivero Mendoza, A.R. Leino, J.P. Mikkola, A. Zolotukhin, K. Eränen, T. Salmi, Sugar hydrogenation in continuous reactors: From catalyst particles towards structured catalysts, Chemical Engineering and Processing Process Intensification 109 (2016) 1–10. https://doi.org/10.1016/J.CEP.2016.07.007.
- [67] A. Najarnezhadmashhadi, J. Wärnå, K. Eränen, H.L. Trajano, D. Murzin, T. Salmi, Modelling of kinetics, mass transfer and flow pattern on open foam structures in tubular reactors: Hydrogenation of arabinose and galactose on ruthenium catalyst, Chem Eng Sci 233 (2021) 116385. https://doi.org/10.1016/J.CES.2020.116385.
- [68] J. Mikkola, T. Salmi, R. Sjöholm, Modelling of kinetics and mass transfer in the hydrogenation of xylose over Raney nickel catalyst, Journal of Chemical Technology & Biotechnology: International Research in Process, Environmental & Clean Technology 74 (1999) 655–662. https://doi.org/10.1002/(SICI)1097-4660(199907)74:7%3C655::AID-JCTB96%3E3.0.CO;2-G.
- [69] T. Salmi, D.Y. Murzin, J.P. Mikkola, J. Wärnå, P. Mäki-Arvela, E. Toukoniitty, S. Toppinen, Advanced kinetic concepts and experimental methods for catalytic three-phase processes, Ind Eng Chem Res 43 (2004) 4540–4550. https://doi.org/10.1021/ie0307481.

- [70] S. Willför, R. Sjöholm, C. Laine, B. Holmbom, Structural features of water-soluble arabinogalactans from Norway spruce and Scots pine heartwood, Wood Sci Technol 36 (2002). https://doi.org/10.1007/s00226-001-0137-x.
- [71] J.P. Wauquier, J.C. Jungers, Utilisation de la méthode de conjonction des réactions pour la comparaison des constantes cinétiques en catalyse hétérogène, Comptes Rendus 243 (1956) 1766–1768.
- [72] J.P. Wauquier, J.C. Jungers, La cinétique quantitative en catalyse hétérogène. L'influence du milieu sur l'activité et la sélectivité du catalyseur, Bull Soc Chim Fr 24 (1957) 1280–1288.
- [73] V. Sifontes Herrera, Hydrogenation of L-arabinose, D-galactose, D-maltose and L-rhamnose, Doctoral Thesis. Åbo Akademi University, 2012.
- [74] H. Fan, Z. Fang, X. Zhao, Y. Hu, B. Li, W. Yang, M. Li, J. Wang, X. Lu, W. Song, J. Fu, Continuous Hydrogenation of Maltose over Raney Ni in a Trickle-Bed Reactor, Ind Eng Chem Res 62 (2023)15395–15405. https://doi.org/10.1021/acs.iecr.3c01723.
- [75] C.R. Wilke, P. Chang, Correlation of diffusion coefficients in dilute solutions, AIChE Journal 1 (1955) 264–270. https://doi.org/10.1002/AIC.690010222.
- [76] National Institute of Standards and Technology, NIST Chemistry WebBook, SRD 69, (n.d.). https://webbook.nist.gov/chemistry/fluid/ (accessed August 17, 2025).
- [77] B.E. Poling, J.M. Prausnitz, J. P. O'Connell, R.C. Reid, The properties of gases and liquids, Mcgraw-Hill, New York, 2001.
- [78] J. Wisniak, M. Hershkowitz, R. Leibowitz, S. Stein, Hydrogen Solubility in Aqueous Solutions of Sugars and Sugar Alcohols, J Chem Eng Data 19 (1974) 247-249. https://doi.org/10.1021/je60062a008.
- [79] T.T. Huu, M. Lacroix, C. Pham Huu, D. Schweich, D. Edouard, Towards a more realistic modeling of solid foam: Use of the pentagonal dodecahedron geometry, Chem Eng Sci 64 (2009) 5131–5142. https://doi.org/10.1016/J.CES.2009.08.028.
- [80] A. Najarnezhadmashhadi, C.G. Braz, V. Russo, K. Eränen, H.A. Matos, T. Salmi, Modeling of three-phase continuously operating open-cell foam catalyst packings: Sugar hydrogenation to sugar alcohols, AIChE Journal 68 (2022) e17732. https://doi.org/10.1002/aic.17732.

- [81] L.A. Belfiore, Dimensional Analysis of the Equations of Change for Fluid Dynamics Within the Mass Transfer Boundary Layer, Transport Phenomena for Chemical Reactor Design (2003) 361–368. https://doi.org/10.1002/0471471623.CH12.
- [82] I. Mohammed, T. Bauer, M. Schubert, R. Lange, Liquid–solid mass transfer in a tubular reactor with solid foam packings, Chem Eng Sci 108 (2014) 223–232. https://doi.org/10.1016/J.CES.2013.12.016.
- [83] V. Russo, T. Kilpiö, M. Di Serio, R. Tesser, E. Santacesaria, D.Y. Murzin, T. Salmi, Dynamic non-isothermal trickle bed reactor with both internal diffusion and heat conduction: Sugar hydrogenation as a case study, Chemical Engineering Research and Design 102 (2015) 171–185. https://doi.org/10.1016/J.CHERD.2015.06.011.
- [84] D. Durante, T. Kilpiö, P. Suominen, V. Sifontes Herrera, J. Wärnå, P. Canu, T. Salmi, Modeling and simulation of a small-scale trickle bed reactor for sugar hydrogenation, Comput Chem Eng 66 (2014) 22–35. https://doi.org/10.1016/J.COMPCHEMENG.2014.02.025.
- [85] F. Turek, R. Lange, Mass transfer in trickle-bed reactors at low reynolds number, Chem Eng Sci 36 (1981) 569–579. https://doi.org/10.1016/0009-2509(81)80145-5.
- [86] J. Zalucky, M. Wagner, M. Schubert, R. Lange, U. Hampel, Hydrodynamics of descending gasliquid flows in solid foams: Liquid holdup, multiphase pressure drop and radial dispersion, Chem Eng Sci 168 (2017) 480–494. https://doi.org/10.1016/J.CES.2017.05.011.
- [87] R.R. Zapico, P. Marín, F. V. Díez, S. Ordóñez, Liquid hold-up and gas—liquid mass transfer in an alumina open-cell foam, Chem Eng Sci 143 (2016) 297–304. https://doi.org/10.1016/J.CES.2016.01.008.

NOTATION

Symbol	Description	Units	
A	Reactor cross-sectional area	m²	
a'	Asymptotic catalytic activity	-	
a	Catalyst activity factor	-	
$a_{ m GL}$	Gas-liquid interfacial area per reactor volume	m ² ·m ⁻³	
a_{LS}	Liquid-solid interfacial area per reactor volume	m ² ·m ⁻³	
as	Geometric external surface area of foam per	m²⋅m⁻³	
	volume	111 111	
C_{H_2}	Hydrogen concentration in the liquid phase	mol·m ⁻³	
$\mathrm{C}^{\mathrm{sat}}_{\mathrm{H}_2}$	Hydrogen solubility (saturation) in the liquid	mol⋅m ⁻³	
H_2	phase	morm °	
C _i	Concentration of species is in the liquid (bulk)	mol·m ⁻³	
C_{L_i}	Concentration of species i at the liquid-solid	mol⋅m-³	
	interface	morm °	
$C_{L_{X}}$	Xylose concentration	mol·m ⁻³	
D _{ax}	Axial dispersion coefficient (liquid phase)	m²⋅s⁻¹	
\mathfrak{D}_i	Molecular diffusivity of species i in water	m²⋅s⁻¹	
$\mathfrak{D}_{\mathrm{i},\mathrm{H_2O}}$	Diffusivity of i in water (explicit form)	m ² ·s ⁻¹	
d_{w}	Foam windows length	m	
E(t)	Residence time distribution (RTD) density		
	function		
$\mathbf{E}_{\mathbf{a}}$	Activation energy	J·mol⁻¹	
e	Skeletal density of Ni solid foams	-	
F(t)	Cumulative RTD function	-	
G'	Superficial gas velocity (as used in holdup	kg·m ⁻² ·s ⁻¹	
	correlations)	kg·IIIS	
${ m k}^{}_{ m GL}$	Gas-liquid mass transfer coefficient	m/s	
$k_{GL} \cdot a_{GL}$	Volumetric gas-liquid mass transfer coefficient	S^{-1}	
$\mathbf{K}_{\mathbf{H}_2}$	Hydrogen adsorption parameter	$m^3 \cdot mol^{-1}$	
k _{LS}	Liquid-solid mass transfer coefficient	m/s	
$k_{LS} \cdot a_{LS}$	Volumetric liquid-solid mass transfer coefficient	S^{-1}	
K _X	Xylose adsorption parameter	m³⋅mol⁻¹	
	100		

ℓ	Axial coordinate	m
L	Total reactor length	m
L_{c}	Characteristic length (e.g., for Peax)	m
	Superficial mass velocity of liquid (as used in	kg·m ⁻² ·s ⁻¹
	holdup correlations)	kg III 3
$ m M_{H_2O}$	Molar mass of water	g·mol⁻¹
m	Number of active sites for carbohydrate	_
Ш	adsorption (semi-competitive mode)	-
\mathbf{m}_0	Initial amount of water in bed	kg
m _L	Mass registered in scale during liquid holdup	kg
L	experiments	Kg.
n' _{i, in}	Molar flow rate of i reactor's inlet	mol·s ⁻¹
n' _{i, out}	Molar flow rate of i reactor's outlet	mol·s⁻¹
N_{GLi}	Molar flux of i across the G-L interface (towards	mol⋅m²⋅s⁻¹
GLi	liquid)	mor m 's
N _{LSi}	Molar flux of i across the L-S interface (towards	mol·m²·s ⁻¹
LSi	solid)	mor m 's
P	Pressure	Pa
Peax	Péclet number	-
P_{H_2}	Hydrogen pressure	Pa
Q	Objective function for parameter estimation	=
R	Universal gas constant	J·mol⁻¹·K⁻¹
Re	Reynolds number $Re = (\rho \cdot u \cdot L_c) / \mu$	_
r	Reaction rate per mass of Ru	mol·kg _{Ru} -l·s-l
$r_{_{ m V}}$	Volumetric reaction rate	mol·m ⁻³ ·s ⁻¹
s(t)	Tracer signal at reactor outlet	a.u.
Sc	Schmidt number $Sc = \mu / (\rho \cdot \mathfrak{D}_i)$	_
Sh	Sherwood number $Sh = (k_c \cdot L_c) / \mathfrak{D}_i$	_
STY	Space-time yield	kg _{xylitol} ·kg _{Ru} -1·h-1
s ₀	Baseline tracer signal (before step input)	a.u.
S _∞	Asymptotic tracer signal (after step input)	a.u.
T	Absolute temperature	K
\overline{T}	Reference temperature	K

ī	Mean residence time	S	
u _z	Superficial liquid velocity	m·s⁻¹	
V _{Bed}	Total packed-bed volume	m³	
V	Liquid hold-up volume (from holdup		
${ m V}^{}_{ m L}$	experiments)	m^3	
$V_{m,i}$	Molar volume (e.g., used in Wilke-Chang)	m³·mol-1	
X _s	Xylose weight fraction	wt.%	
X	Calculated conversion	_	
X _{Exp}	Experimental conversion	_	
	Dimensionless concentration of i in the L-S		
y_{i}	interface	_	
Z	Axial coordinate (dimensionless)	_	
α	Competitiveness factor	-	
β_0^{sat}	Baseline level of hydrogen solubility correlation	-	
β_1^{sat}	Main temperature (Arrhenius-like) effect in	K	
P ₁	hydrogen solubility correlation	K	
β_2^{sat}	Extra temperature curvature in hydrogen	-	
r 2	solubility correlation		
β_3^{sat}	Effect of xylose concentration in hydrogen	L·mol⁻¹	
, 3	solubility correlation		
β_4^{sat}	Temperature-concentration interaction in	L·K·mol-1	
4	hydrogen solubility correlation		
β_5^{sat}	Pressure non-ideality correction in hydrogen	1/bar	
	solubility correlation		
ε	Bed void fraction	_	
$\epsilon_{_{ m L}}$	Liquid holdup in the bed		
κ _{1,363 K}	Kinetic parameter for xylose hydrogenation to	mol∙kg _{Cat} -¹·min ⁻¹	
.,	xylitol at 363 K (Raney-type catalysts)		
κ _{2, 363 K}	Kinetic parameter for xylose isomerization to	mol·kg _{Cat} -¹·min⁻¹	
2, 303 K	xylulose at 363 K (Raney-type catalysts)		
K 2 262 V	Kinetic parameter for xylulose isomerization to	m³∙kg _{Cat} -¹∙min-¹	
K3, 363 K	xylose at 363 K (Raney-type catalysts)		
K4, 363 K	Kinetic parameter for xylulose hydrogenation to	m³·kg _{Cat} -¹·min-¹	
	arabitol at 363 K (Raney-type catalysts)		

Ve acar	Kinetic parameter for xylulose hydrogenation to	m³·kg _{Cat} -¹·min-¹	
K5, 363 K	xylitol at 363 K (Raney-type catalysts)		
к _{X, 363 К}	Kinetic parameter for xylose hydrogenation	$m^3 \cdot kg_{Ru}^{-1} \cdot s^{-1} \cdot Pa^{-1}$	
μ	Liquid viscosity	Pa·s	
$\mu_{\mathrm{H_2O}}$	Water viscosity	Pa·s	
$\rho_{ m B}$	Apparent bulk density of catalyst in the bed	kg _{Ru} ⋅m ⁻³	
$ ho_{ m G}$	Gas density	kg·m ⁻³	
$ ho_{ m L}$	Liquid density	kg·m ⁻³	
σ	Relative reactivity arabinose to galactose	-	
$\sigma_{ heta}^2$	Dimensionless RTD variance	-	
$ au_{ m L}$	Hydraulic residence time	S	
$\Phi_{\mathrm{H_2O}}$	Association factor of water (Wilke-Chang)	_	
φ	Wetting efficiency	_	
Ø	Reactor diameter	m	
A_{μ} , B_{μ} , F_{μ}	$, B_{\mu}, F_{\mu}$ Constants of viscosity correlation		
$A_{\rho}, B_{\rho}, \dots F_{\rho}$	Constants of density correlation	[66]	

Abbreviations

AO - Anodic Oxidation

NTP – Normal temperature and pressure (293.15 K and 101325 Pa)

PFA – Poly(furfuryl alcohol)

PEG – Poly(ethylene glycol)

ICP-OES – Inductively Coupled Plasma Optical Emission Spectroscopy

TPR - Temperature-Programmed Reduction

XPS - X-ray Photoelectron Spectroscopy

TGA – Thermogravimetric Analysis

HPLC - High-Performance Liquid Chromatography

RI – Refractive Index (detector)

BET-Brunauer-Emmett-Teller

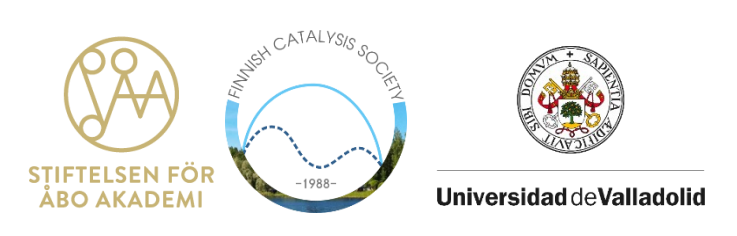
NLDFT - Non-Local Density Functional Theory

RTD - Residence Time Distributio

ACKNOWLEDGMENTS

The research presented in this doctoral thesis was made possible thanks to the financial support of several institutions. I gratefully acknowledge Åbo Akademi University for funding my doctoral research through Åbo Akademi University funded doctoral positions (Call 2021). I also acknowledge the Research Council of Finland for providing essential support for materials, supplies, and publication activities thought the Academy Professor's grants 319002, 320115, and 345053 (Tapio Salmi). I am thankful to Stiftelsen för Åbo Akademi (the Åbo Akademi University Foundation) and the Finnish Catalysis Society for awarding travel grants that enabled my participation in international conferences. Finally, I extend my gratitude to the University of Valladolid and the Erasmus+ Programme for supporting my continuous learning and participation in academic courses abroad.







Appendix I

Kinetic and Transport Modelling of Continuous Xylose Hydrogenation on Ru/C Solid Foam Catalysts

German Araujo-Barahona^{1,2}, Maria Ciaramella^{1,3}, Miriam Cavaliere^{1,3}, Guillaume Bricault^{1,4}, Kari Eränen¹ Juan García-Serna², Vincenzo Russo³, Dmitry Yu. Murzin¹, Tapio Salmi^{1,3}

ABSTRACT

Continuous hydrogenation of xylose to xylitol was studied on Ru/C solid foam catalysts in a trickle bed reactor. Laboratory-scale experiments revealed the effects of temperature, liquid flow rate, and feed concentration on xylose conversion, xylitol selectivity, and space-time yield (STY). Residence time distribution (RTD) and liquid holdup measurements were conducted to characterize the hydrodynamics of the reactor. The catalysts showed stable performance with xylitol selectivity exceeding 94 %. The xylose conversion increased with temperature, while increasing liquid flow enhanced the interfacial mass transfer but reduced the residence time, leading to trade-offs in the overall performance. Higher xylose concentrations lowered the conversion due to viscosity and reactant adsorption effects but raised the STY. A kinetic-transport model coupling a non-competitive adsorption rate expression with axial dispersion and external resistances reproduced the experimental trends well and quantified the gas-liquid and liquid-solid contributions. Both resistances were comparable in magnitude, confirming their relevance within the investigated low-interaction regime. These results underscore the need to include kinetics, mass transfer, and hydrodynamics when designing reactors based on solid foam catalysts to exploit their unique features.

Keywords: trickle bed reactor; solid foam; structured catalyst; xylose hydrogenation; xylitol; interfacial mass transfer; axial dispersion

¹Laboratory of Industrial Chemistry and Reaction Engineering (TKR), Johan Gadolin Process Chemistry Centre (PCC), Åbo Akademi University, FI-20500 Turku/Åbo Finland.

² Grupo de Tecnologías a Presión (PressTech), Instituto de Bioeconomía de la Universidad de Valladolid (BioEcoUVa), Departamento de Ingeniería Química y Tecnología del Medio Ambiente, Escuela de Ingenierías Industriales, Universidad de Valladolid.

³Chemical Sciences Department, Università di Napoli "Federico II", Complesso Universitario Monte S. Angelo, IT-80126, Napoli, Italy

⁴Université de Poitiers, CNRS UMR7285, Institut de Chimie des Milieux et Matériaux de Poitiers, B27, TSA 51106, 4 rue
Michel Brunet, 86073 Poitiers Cedex 9, France

1. Introduction

In the last decade, research activities in chemical reaction engineering have focused on developing efficient processes for biomass valorization, aiming at the production of platform chemicals, fine and specialty chemicals, food ingredients and fuels. Great progress has been achieved in two fields: (i) development of new catalytic systems to achieve high activity, selectivity, and stability despite the recalcitrant nature of biomass-derived feedstock, and (ii) novel reactor and separation technologies that allow catalytic processes to operate under industrially relevant conditions (Akhtar et al., 2025; Besson et al., 2014; Mallesham et al., 2020). Process intensification (PI), i.e. development of new structures and application of non-conventional forms of energy has a key role in this scientific and industrial revolution. Inefficient reactor technology leads to low substrate conversion or poor selectivity, which causes increasing separation costs, which has a negative impact on the process economy. For this reason, reaction intensification is a crucially important field of research and innovation.

Many biomass conversion processes involve three-phase reactions, where a substrate dissolved in the liquid phase reacts with a dissolved gaseous reagent at the surface of a solid catalyst, as typically observed in hydrogenation and oxidation processes. These systems involve several coupled steps: transfer of gas to the liquid surface, gas dissolution, mass transfer of molecules to the catalyst surface, adsorption of reactants, chemical reactions on active catalyst sites, and desorption of reaction products (Salmi et al., 2004). Because of these strongly interlinked phenomena, mass transfer limitations often strongly affect the reactor performance. A common industrial strategy to minimize the intraparticle diffusion resistance in catalyst pores is the use of finely dispersed catalyst particles (<100 µm) in slurry reactors, although it complicates the separation process and can cause catalyst attrition and enhance metal leaching (Gianetto and Specchia, 1992). Hydrogenation processes based on the use of molecular hydrogen as the reducing agent are frequently applied in pharmaceutical and alimentary industries as well as in the production of fuels and solvents. From the chemical viewpoint, these processes often include selective hydrogenation of double bonds and carbonyl groups in organic molecules. A representative case is the hydrogenation of sugars to sugar alcohols, such as hydrogenation glucose to sorbitol and xylose to xylitol, usually performed in semi batch mode in high-pressure autoclaves in the presence of sponge nickel (Raney-type nickel) catalysts(García et al., 2021). To increase productivity and to facilitate optimal integration with continuous downstream operations, there is growing interest in shifting hydrogenation processes to continuous mode (Araujo-Barahona et al., 2025, 2022; Fan et al., 2023a; Lali et al., 2015; Najarnezhadmashhadi et al., 2021). Such a transition requires catalytic systems that are active, selective, stable, mechanically robust, and capable of operating with low pressure drop in fixed-bed configurations.

Structured catalysts such as fibers, monoliths, open-cell foams, and 3D-printed structures meet these very acute needs in the development of new technology. The new structures provide high void fraction (up to 97 %), low pressure drop, and good mechanical strength in continuous operation (Ho et al., 2019). Metallic open-cell foams combine high thermal conductivity with large geometric surface areas (700–7000 m^2/m^3 depending on porosity), and thin catalyst layers (<100 \mu m) suppressing the internal diffusion resistance in the catalyst pores and open structures with a low pressure drop (Shen et al., 2018). In this way, the benefits of the conventional slurry and packed bed technologies are combined in the structured catalysts and reactors.

Among the currently available reactor configurations, trickle bed reactors (TBR) are particularly relevant for three-phase hydrogenation processes. In co-current downflow operation at low superficial velocities, the gas is the continuous phase while the liquid flows downwards as films and rivulets over the catalyst surface, known as the low-interaction regime (Al-Dahhan et al., 1997). Compared with slurry reactors, product separation is simpler in trickle beds, allowing higher operating pressures and temperatures, and approaching plug flow hydrodynamics, which is favorable for most types of reaction kinetics (Gianetto and Specchia, 1992). However, their performance depends on the hydrodynamics and transport phenomena, including liquid holdup, wetting efficiency, axial and radial dispersion, pressure drop, and gas-liquid and liquid-solid mass transfer resistances. Quantifying these effects in foam-packed beds under reactive conditions is a real challenge (Aguirre et al., 2020; Cognet et al., 1995; da Fonseca Dias and da Silva, 2022; Lali, 2016; Mohammed et al., 2014; Stemmet, 2008; Zalucky et al., 2017). While previous studies have characterized individual aspects of foam-packed TBRs, such as holdup, dispersion, pressure drop, and interfacial mass transfer, there is still a lack of integrated analyses to connect hydrodynamics and multiscale mass transfer to intrinsic reaction kinetics for sugar hydrogenation on foam-supported catalysts. Bridging this gap is essential to approach the maximal efficiency, i.e. intrinsic kinetic control and to rationally select the optimal operation regimes and reactor configurations.

In this work, the continuous hydrogenation of xylose to xylitol on Ru/C solid foam catalysts in cocurrent downflow parallelly coupled trickle beds was investigated. The reactor hydrodynamics was characterized by residence-time distribution and holdup measurements, and relevant reactor models — plug flow and axial dispersion models — were fitted to experimental data using a rate expression based on non-competitive adsorption of hydrogen and xylose molecules. The analysis quantified the contributions of gas-liquid and liquid-solid mass transfer resistances under the operating conditions and the implications for approaching intrinsic kinetic control in foam-based trickle bed reactors was discussed in detail.

2. Experimental section

2.1. Materials and reagents

D-xylose (\geq 99.0%), xylitol (\geq 99.0%), D-arabitol (99.0%), and D-xylulose (\geq 95%), Ruthenium(III) nitrosyl nitrate solution (1.4 wt.% Ru), furfuryl alcohol (98.0%), oxalic acid dihydrate (95.0%), poly(ethylene glycol) (8 kDa), and quartz sand (SiO₂, particle size 0.2–0.8 mm, \geq 40%) were purchased from Sigma-Aldrich. An aluminium foam sheet (40 PPI) was purchased from Goodfellow Cambridge Ltd.

2.2. Catalyst synthesis

Ru/C solid foam catalysts were synthesized according to the procedure described in a previous publication by our group (Araujo-Barahona et al., 2023). Briefly, aluminum foams (void fraction=0.93) cylindrical pieces (9 mm in diameter and 33 mm in length) and subjected to anodic oxidation and calcination to generate surface roughness. A thin carbon layer was deposited onto their surface via polymerization of furfuryl alcohol, using polyethylene glycol as a pore-forming agent and oxalic acid as polymerization catalyst, and subsequent pyrolysis (550°C). The resulting carbon layer was activated in an air stream (350°C) and functionalized using a 5 wt. % nitric acid solution. Ruthenium nanoparticles were deposited onto the carbon coating by impregnation with a Ru (III) nitrosyl nitrate solution, followed by drying. The catalysts were finally reduced in a hydrogen stream for 5 h at 300 °C for five hours under 100 mL/min hydrogen flow using a temperature ramp of 3 °C/min. The key catalyst properties are summarized in Table 1.

Table 1. Relevant characteristics of prepared Ru/C solid foam catalysts.

Catalyst property	Value
Catalyst mass (3 pieces)/ g	2.14
Carbon loading/ wt.%	35-40
Ru loading (based on carbon)/ wt.%	~1.0
Foam windows size /mm	1.21
Foam strut size/ mm	0.21
Carbon layer thickness/ µm	~10¹
Geometrical surface area/ m²/m³	2200 ²
Ru nanoparticle size/ nm	2.8 ± 1.0 nm
Void fraction/ %	91³

¹Based on scanning electron microscopy images.

Figure 1 displays the physical appearance of the prepared catalysts. As can be seen from Figure 1b, the structure remains open after carbon coating yielding a thin carbon layer with approximately 10 µm thickness (Figure 1c) and a narrow Ru nanoparticle size distribution with an average size of 3 nm.

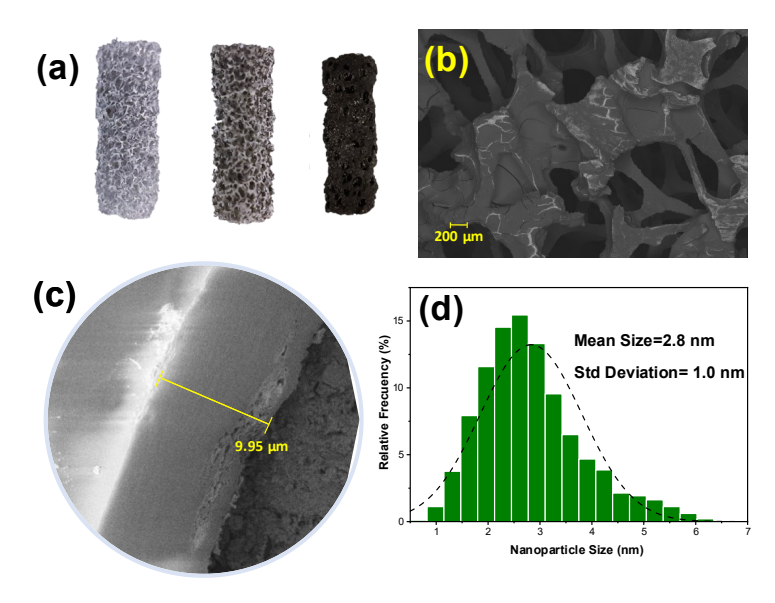


Figure 1. Key preparation parameters of Ru/C solid foam catalysts: (a) progression of the foam support through the synthesis sequence; (b) SEM image showing foam morphology; (c) thickness of the carbon coating measured on struts; (d) size distribution of Ru nanoparticles on the carbon layer.

² Estimate with the procedure described by Huu et al. (2009)

³Based on apparent density measurements.

2.3. Continuous hydrogenation experiments

Kinetic experiments were carried out in a laboratory-scale parallel screening reactor displayed in Figure 2. The reactor system consisted of six tubular beds (R1–R6; L = 23.1 cm, i.d. = 1 cm), each equipped with independent heating jackets, gas flow controllers, and HPLC pumps. Gas and liquid flowed co-currently through the beds, and samples were withdrawn via a small sampling loop (L = 2 cm, i.d. = 0.15 cm). The reactor effluents were cooled in heat exchangers (E-X) and collected in 1 L vessels (C-X). The pressure of the system was controlled with a backpressure valve installed on a shared outlet line; a 0.5 L overflow vessel (OC-1) protected the regulator from liquid carryover.

Each bed was packed as shown in Figure 2b: an initial layer of quartz sand to improve uniform gas-liquid distribution, followed by an uncoated aluminium foam to stabilize the velocity profile, and finally three Ru/C foam catalysts. A thermocouple embedded in the last quartz was in contact with the last Ru/C solid foam catalyst.

A standard hydrogenation experiment was performed in the following way.

- The reactor was filled with hydrogen with a gas flow rate of 100 mL·min⁻¹, NTP.
- The catalysts were reduced in-situ at 120 °C for 2 h.
- The system temperature adjusted to the desired setpoint.
- The sugar solution fed at the target liquid flow rate and the samples were withdrawn every ~30 min for 5 h.
- After the experiment, the reactor was stepwise depressurized and flushed with deionized water (1.00 mL/min) under 1 bar Ar (50 mL/min). The catalysts were stored under 1 bar Ar to prevent oxidation.
- HPLC analysis (HP 1100, RI detector) was performed with a Rezex RCM-Monosaccharide Ca^{2+} column at 70 °C using 1.2 mM $CaSO_4$ as the mobile phase (0.6 mL/min, 5 μ L injection volume).

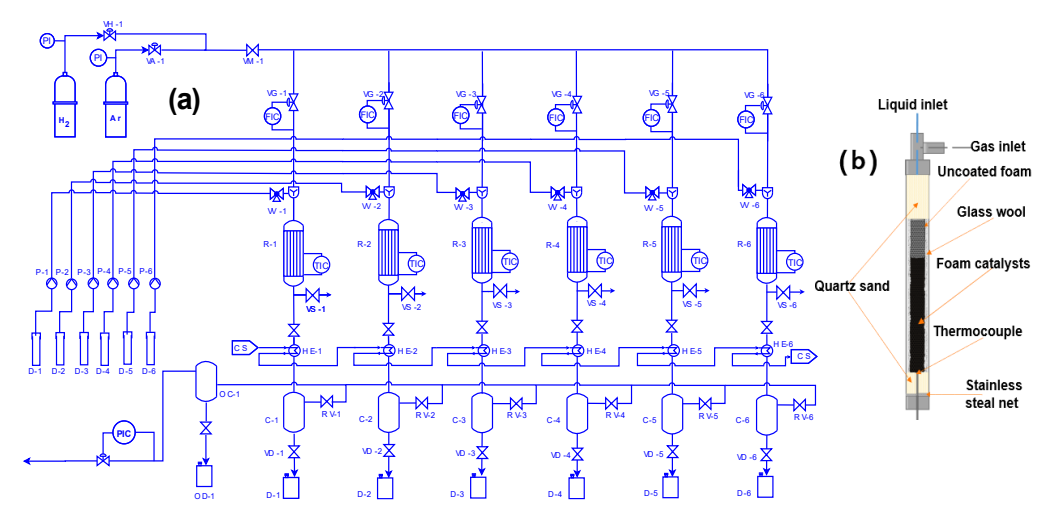


Figure 2. Parallel screening reactor system: (a) flow diagram and (b) packing of an individual reactor with solid foam catalysts.

2.4. Residence time distribution (RTD) experiments

The hydrodynamics of the packed bed was characterized through step-response experiments at liquid flow rates between 0.25 and 1.00 mL/min The reactor was first pressurized with hydrogen (100 mL min⁻¹, NTP) to 20 bar and heated to 120 °C. Water was pumped at the selected flow rate and allowed to stabilize for 1 h. Subsequently, the feed was switched to an inert tracer solution, consisting of 0.13 M xylitol, chosen to mimic the physical properties of the reaction mixture. Liquid samples were collected from the reactor outlet at intervals adjusted to the flow rate, and the tracer concentration was quantified by HPLC. The time delay introduced by the inlet tubing was determined in separate RTD experiments performed at the reactor inlet using three-way valves VV-X and the results were applied as a correction to the measured residence time distributions.

The cumulative residence time distribution F(t) was obtained from the tracer signal S(t) according to

$$F(t) = \frac{s(t) - s_0}{s_\infty - s_0}$$
 (1)

where s_0 and s_∞ correspond to the baseline and the asymptotic signals at long times, respectively. The residence time distribution E(t) was then computed as the time derivative of F(t)

$$E(t) = \frac{dF(t)}{dt}$$
 (2)

7

The mean residence time \bar{t} and the variance σ^2_{θ} of the RTD were calculated from the first and second moments of E(t):

$$\overline{t} = \varepsilon_L \cdot \tau_L = \int_0^\infty E(t) dt$$
 (3)

$$\sigma_{\theta}^{2} = \int_{0}^{\infty} \left(\frac{t}{\varepsilon_{L} \cdot \tau_{L}} - 1 \right)^{2} \cdot E(t) dt$$
 (4)

Using the non-reactive transient axial dispersion model (ADM), the dimensionless variance σ^2_{θ} of

 $Pe_{ax} = \frac{\vec{v}_z - \vec{v}_c}{D_z}$ the residence time distribution (RTD) is related to the axial Peclet number axial dispersion coefficient \vec{D}_z , the linear velocity \vec{v}_z , and the characteristic length L as:

$$\sigma_{\theta}^{2} = \frac{2}{Pe_{xx}^{2}} \left(Pe_{ax} - 1 + e^{-Pe_{ax}} \right)$$
 (5)

The experimental curves F(t) were fitted by nonlinear regression to a logistic function, which was differentiated analytically to compute the moments while avoiding noise amplification from numerical differentiation. Finally, Equation (5) was solved iteratively for $^{\text{Pe}}_{\text{ax}}$ using Brent's method implemented in Python.

2.5. Liquid Holdup Experiments

To determine the liquid holdup inside the reactor under the experimental conditions, a gravimetric recirculation method was employed, following the procedure described by García-Serna et al. (2017), as illustrated in Figure 3. The method is based on water mass balance: a fixed amount of water (200 g) is continuously recirculated at a constant liquid flow rate in a closed-loop system operating at fixed temperature, pressure, and gas flow rate. The change in water mass is continuously recorded until a steady state is achieved.

To determine the liquid holdup inside the reactor under the experimental conditions, a gravimetric recirculation method was employed, following the procedure described by García-Serna et al. (2017), as illustrated in Figure 3. The method is based on water mass balance: a fixed amount of water (200 g) is continuously recirculated at a constant liquid flow rate in a closed-loop system operating at fixed temperature, pressure, and gas flow rate. The change in water mass is continuously recorded until a steady state is achieved.

In a typical experiment, helium was continuously fed to the reactor at a controlled flow rate through valve VG-H-1, which served as the main gas inlet. A small auxiliary flow (5 mL/min STP) was introduced via VG-H-2 to improve the pressure stability. The system pressure was maintained with a backpressure controller (EquilibarU3L Ultra Low Flow Back Pressure Regulator). Prior to

each run, the liquid line was pre-filled with water up to the reactor inlet by setting the three-way valve VV-H-1 to close the path to the reactor and open the outlet to the atmosphere. Once the target temperature and pressure were reached, the scale was tared. At t=0, the HPLC pump (P-H-1) was started, and the scale continuously recorded the water retained in the reactor. Mass measurement data were collected every minute until stabilization, enabling the determination of the liquid holdup at the steady state.

Key process parameters—liquid flow rate (0.1–2 mL/min), pressure (1–30 bar), and gas flow rate (50–200 mL NTP/min)— were varied systematically, while the temperature was fixed at 90 °C to represent the hydrogenation conditions and to prevent water evaporation. The liquid holdup was measured using the same packing employed in the continuous kinetic studies (Section 2.3). Independent measurements were carried out with the reactor packed only with Ru/C solid foams to determine the holdup specific to the catalytic section.

The liquid holdup (ϵ L) is defined by Equation (6), where V_L and V_{Bed} are the retained liquid volume and total bed volume, respectively. Here, m_L is the measured mass of water retained in the reactor at a given time point, m_0 is the initial water mass in the bed, and \emptyset and L are the reactor diameter and length, respectively.

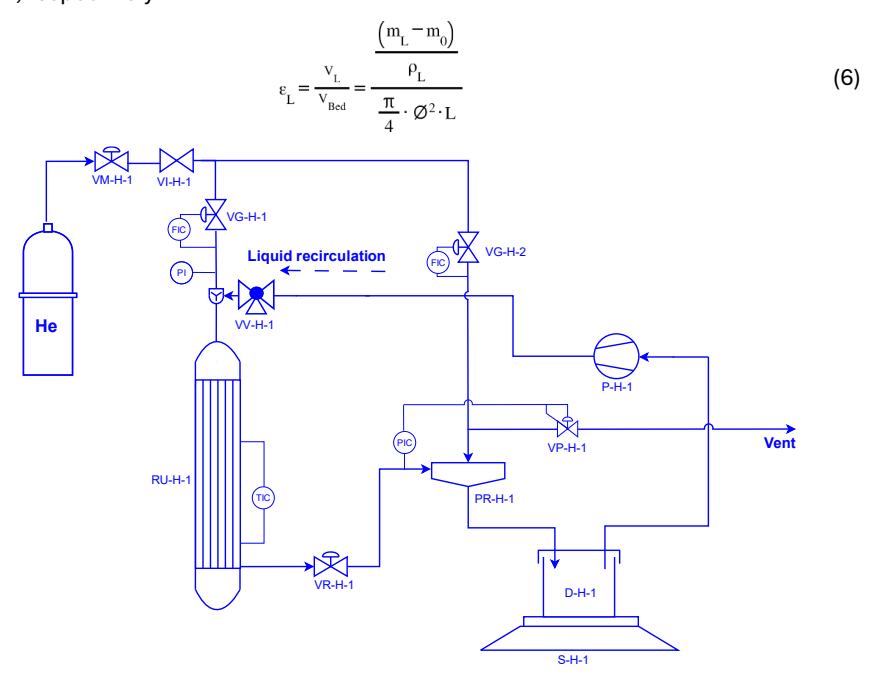


Figure 3. Experimental setup for liquid holdup measurement using the gravimetric recirculation method.

3. Kinetic and transport modeling

3.1. Physical properties

The following physical properties were used to describe the experimental data obtained for the continuous xylose hydrogenation on Ru/C solid foam catalysts.

The correlation proposed by Sifontes Herrera et al. (2016a) was used to estimate the viscosity of aqueous sugar solutions as a function of the weight fraction (x_s) and temperature ($T/^{\circ}C$). The coefficients reported for arabinose were adopted because of its structural similarity to its epimer, xylose.

$$\ln(\mu_{L}) = A_{\mu} \cdot \frac{x_{s}}{(T/^{\circ}C)} + B_{\mu} \cdot x_{s}^{2} + C_{\mu} \cdot x_{s} + D_{\mu} + \frac{E_{\mu}}{(T/^{\circ}C)} + \frac{F_{\mu}}{(T/^{\circ}C)^{2}}$$
(7)

The densities of the solutions under different experimental conditions were determined using Equation (8). As in the previous case, the coefficients estimated for arabinose were used.

$$\rho_{L} = -A_{o} \cdot T(^{\circ}C) \cdot x_{s} + B_{o} \cdot x_{s}^{2} + C_{o} \cdot x_{s} + D_{o} - E_{o} \cdot T(^{\circ}C) + F_{o} \cdot T(^{\circ}C)^{2}$$
(8)

The diffusion coefficients of xylose and hydrogen in water were calculated using the Wilke-Chang correlation (Wilke and Chang, 1955).In Equation (9), \mathfrak{D}_{i, H_2O} is the diffusion coefficient of the species i in water, $\phi_{H_2O}=2.6$ is the association factor for water, M_{H_2O} is the molar mass of water, μ_{H_2O} is the water viscosity and V_{mi} is the normal boiling molar volume for hydrogen (National Institute of Standards and Technology, n.d.) or the effective molar volume for xylose, which was estimated using the atomic group increments of Le Bas, as reported by Poling et al. (Poling et al., 2001).

$$\mathfrak{D}_{i, H_2O} = 7.4 \times 10^{-12} \cdot \frac{\left(\Phi_{H_2O} \cdot M_{H_2O}\right)^{0.5} \cdot T}{\mu_{H_2O} \cdot V_{mi}^{0.6}}$$
(9)

The solubility of hydrogen in aqueous xylose solutions was calculated using the data collected by Wisniak et al. (1974) (Equation (10)). The pressure exerts the strongest influence on the hydrogen solubility, while the concentration effect is moderate and the effect of temperature is comparatively less pronounced but increases slightly with increasing temperature. The values of the constants are: $\beta_0^{\text{sat}} = -1.45 \times 10^3$, $\beta_1^{\text{sat}} = 6.47 \times 10^3$ K, $\beta_2^{\text{sat}} = 20.30$, $\beta_3^{\text{sat}} = 4.72 \times 10^2$ K·L/mol, $\beta_4^{\text{sat}} = -3.2 \times 10^{-3}$ bar⁻¹.

$$\left(\frac{C_{H_2}^{\text{sat}}}{L}\right) = \left(\frac{P}{\text{bar}}\right) \cdot e^{\left(\beta_0 + \frac{\beta_1^{\text{sat}}}{T} + \beta_2^{\text{sat}} \cdot \text{LnT} + \beta_3^{\text{sat}} \cdot C_x + \beta_4^{\text{sat}} \cdot \frac{\left(C_x / \frac{\text{mol}}{L}\right)}{T} + \beta_5^{\text{sat}} \cdot \left(\frac{P}{\text{bar}}\right)\right)} \tag{10}$$

3.2. General model hypothesis

The general hypotheses adopted for the formulation of the model are the following:

- Internal mass transfer limitations are negligible compared to external mass transfer resistances, due to the thin catalyst layer, as supported by previous simulations(Najarnezhadmashhadi et al., 2022).
- The axial dispersion coefficient is assumed to be common to all species in the liquid phase and is taken as the value determined from step-response RTD studies.
- The liquid holdup in the catalytically active section is equal to the value measured by the gravimetric recirculation method.
- Radial concentration and velocity gradients were neglected due to the small reactor diameter.

3.3. Reaction kinetics

The reaction kinetics of xylose hydrogenation over the tested Ru/C solid foam catalyst was taken from our previous work and are expressed by Equation (14), which is based on a non-competitive adsorption model between xylose and hydrogen. The kinetic parameters were obtained through non-linear regression of an extensive batch experimental dataset (Mikkola et al., 1999). This model assumes that the size difference between xylose and hydrogen molecules justifies, from a physical standpoint, that they adsorb distinct types of active sites, , thereby implying negligible competition for surface adsorption. The Ru cluster size of the solid foams used in the continuous experiments matched the average size of the catalysts employed in the batch studies (Figure 1 Consequently, the same kinetic model and parameters can be applied.

$$r = \frac{\kappa_{X, 363 \text{ K}} \cdot e^{\frac{E_a}{R} \cdot \left(\frac{1}{T} - \frac{1}{T}\right)} \cdot C_X \cdot C_{H_2}}{\left(1 + K_X \cdot C_X\right) \cdot \left(1 + \sqrt{K_{H_2} \cdot C_{H_2}}\right)^2}$$
(11)

Alternative approaches, such as the semi-competitive adsorption model, provide a more realistic description by considering that the catalyst surface is predominantly covered by sugar molecules, with hydrogen adsorbing mainly on accessible interstitial sites(Araujo-Barahona et al., 2023; Mikkola et al., 1999; Salmi et al., 2004). However, for the purposes of this work, the simplified non-competitive model was adopted to reduce the mathematical complexity, given the inherently high nonlinearity of the coupled mass transfer and reaction phenomena in the system.

Parameter	Value	Units	Relative error (%)
к _{х, 363 К}	7.39x10 ⁻⁴	m ⁶ /(kg _{Ru} ·mol·s)	11.0
K _x	9.13x10 ⁻³	m³/mol	0.9
K_{H_2}	1.77x10 ⁻¹	m³/mol	16.2
$\mathbf{E}_{\mathbf{a}}$	4.18x10 ⁴	J/mol	3.8
\mathbb{R}^2	98.85 %	-	-

Table 1. Kinetic parameters for the non-competitive adsorption model.

3.4. Liquid-phase mass balance

The general mass balance for a control volume of species i in the liquid phase, including convection, axial dispersion, diffusion into the solid catalyst, and gas-liquid transfer, is given in Equation (12). In this Equation, n'_{in} and n'_{out} are the convective molar flow rates of i entering and

leaving the control volume, respectively. The terms $\left(-D_z \cdot \frac{dC_{Li}}{d\ell} \cdot A \cdot \varepsilon_L\right)_{in}$ and $\left(-D_z \cdot \frac{dC_{Li}}{d\ell} \cdot A \cdot \varepsilon_L\right)_{out}$ account for the dispersive fluxes at the inlet and outlet faces. The quantity N_{GLi} denotes the interfacial flux of i from the liquid to the solid catalyst, and ΔA_{LS} is the diffusion area through the catalyst. The transport of component i from the gas phase to the liquid bulk phase is represented by the product $N_{GLi} \cdot a_{GL}$. While A is the reactor cross-sectional area and ε_L is the liquid holdup.

$$n'_{i, in} + \left(-D_z \cdot \frac{dC_{Li}}{d\ell} \cdot A \cdot \varepsilon_L\right)_{in} + N_{GLi} \cdot \Delta A_{GL} = N_{LSi} \cdot \Delta A_{LS} + n'_{i, out} + \left(-D_z \cdot \frac{dC_{Li}}{d\ell} \cdot A \cdot \varepsilon_L\right)_{out} + \frac{dn_{Li}}{dt}$$
(12)

Introducing the terminology $\Delta=$ out - in, as well as $n_{Li}=C_{Li}\cdot\Delta \ V\cdot \varepsilon_{Li}$ and $\Delta \ n'_{i}=\Delta \ C_{Li}\cdot u_{z}\cdot A$ the Equation can be rewritten as:

$$D_{z} \cdot A \cdot \varepsilon_{L} \cdot \Delta \left(\frac{dC_{Li}}{d\ell} \right) - \Delta C_{Li} \cdot u_{z} \cdot A + N_{GLi} \cdot \Delta A_{GL} = N_{LSi} \cdot \Delta A_{LS} + \frac{dC_{Li}}{dt} \cdot \Delta V \cdot \varepsilon_{L}$$
 (13)

The area-to-volume ratio of the external catalyst surface and gas- liquid surface are introduced as $a_{LS} = \frac{\Delta A_{LS}}{\Delta V}$ and $a_{GL} = \frac{\Delta A_{GL}}{\Delta V}$, respectively. As well as $\Delta V = A \cdot \Delta I$, giving:

$$\frac{D_{i}}{\Delta \ell} \cdot \Delta \left(\frac{dC_{Li}}{d\ell} \right) - \frac{\Delta C_{Li} \cdot u_{z}}{\Delta l \cdot \varepsilon_{L}} + \frac{N_{GLi} \cdot a_{GL}}{\varepsilon_{L}} = \frac{N_{LSi} \cdot a_{LS}}{\varepsilon_{L}} + \frac{dC_{Li}}{dt}$$
(14)

Subsequently, the dimensionless axial coordinate $z = \frac{\ell}{L}$, the axial Peclet number $Pe_{ax} = \frac{u_z \cdot L}{D_z}$ and

the residence time $\tau_L = \frac{\ell}{u_z}$ are introduced, giving Equation (15).

$$\frac{1}{\text{Pe}_{\text{ax}} \cdot \tau_{\text{L}} \cdot \Delta z} \cdot \Delta \left(\frac{\text{dC}_{\text{Li}}}{\text{dz}}\right) - \frac{\Delta C_{\text{Li}}}{\varepsilon_{\text{L}} \cdot \tau_{\text{L}} \cdot \Delta z} + \frac{N_{\text{GLi}} \cdot a_{\text{GL}}}{\varepsilon_{\text{L}}} = \frac{N_{\text{LSi}} \cdot a_{\text{LS}}}{\varepsilon_{\text{L}}} + \frac{\text{dC}_{\text{Li}}}{\text{dt}}$$
(15)

By letting $\Delta z \rightarrow 0$, the final form of Equation (15) is obtained,

$$\frac{1}{\text{Pe}_{\text{av}} \cdot \tau_{\text{I}}} \cdot \frac{\text{d}^{2}\text{C}_{\text{Li}}}{\text{d}z^{2}} - \frac{1}{\tau_{\text{I}} \cdot \epsilon_{\text{I}}} \cdot \frac{\text{dC}_{\text{Li}}}{\text{d}z} + \frac{N_{\text{GLi}} \cdot a_{\text{GL}}}{\epsilon_{\text{I}}} = \frac{N_{\text{LSi}} \cdot a_{\text{LS}}}{\epsilon_{\text{I}}} + \frac{\text{dC}_{\text{Li}}}{\text{dt}}$$
(16)

At steady state the accumulation term is zero. The gas-to-liquid transfer of species i is represented by the volumetric term, $\mathbf{k}_{\mathrm{GLi}} \cdot \mathbf{a}_{\mathrm{GL}} \cdot \left(\mathbf{C}_{\mathrm{Li}}^{\mathrm{sat}} - \mathbf{C}_{\mathrm{Li}} \right)$ where $\mathbf{C}_{\mathrm{Li}}^{\mathrm{sat}}$ is the liquid-phase concentration of the species (i) at gas-liquid equilibrium under the local interfacial temperature (T) and pressure (P), i.e., the equilibrium solubility. In our system, hydrogen is the only gas-phase component, and its saturation concentration is obtained from the selected solubility correlation as a function of temperature, pressure, and liquid composition.

$$\frac{\varepsilon_{L}}{Pe_{ax}} \cdot \frac{d^{2}C_{Li}}{dz^{2}} - \frac{dC_{Li}}{dz} + k_{GLi} \cdot a_{GL} \cdot \left(C_{Li}^{sat} - C_{Li}\right) \cdot \tau_{L} = N_{LSi} \cdot a_{LS} \cdot \tau_{L}$$
(17)

If $Pe_{ax} \rightarrow \infty$, Equation (17) reduces to the plug flow reactor model as shown by Equation (18), with initial condition $C_{Lx} = C_{sln}$ and $C_{LH_{\gamma}} = C_{sln}^{sat}$ at z = 0.

$$-\frac{dC_{Li}}{dz} + k_{GLi} \cdot a_{GL} \cdot \left(C_{Li}^{sat} - C_{Li}\right) \cdot \tau_{L} = N_{LSi} \cdot a_{LS} \cdot \tau_{L}$$
(18)

3.5. External mass transfer: Liquid-solid interface

The mass balance for a component i in the solid-liquid interface of the catalyst is given by Equation (19), assuming steady-state conditions at the interface. Under this hypothesis, all the reactants that cross the liquid–solid interface are immediately consumed by the reaction, and the flux of product from to the liquid phase is equal to the reaction rate.

$$v_{i} \cdot r \cdot \Delta m_{cat} + N_{LSi} \cdot \Delta A_{LS} = 0$$
 (19)

The definitions of catalyst bulk density ($\rho_B = \frac{m_{Ru}}{V_L}$), which corresponds to the ratio between the mass of active metal (m_{Ru}) and the total liquid volume (V_L), along with surface area-to-volume ratio are introduced, yielding the relation,

$$v_i \cdot r \cdot \rho_B + N_{LSi} \cdot a_{LS} = 0 \tag{20}$$

Based on film theory and Fick's first law, the flux of species i (here N_{LSi}) through the stagnant liquid film can be expressed as Equation (21). The liquid-phase mass transfer coefficient is denoted as k_{LSi} representing the rate at which the species is transported from the bulk liquid to the solid–liquid interface,

$$N_{LSi} = k_{LSi} \cdot \left(C_{Li} - C_i \right) \tag{21}$$

Combining (20) and (21) gives,

$$v_{i} \cdot r \cdot \rho_{B} + k_{LSi} \cdot a_{LS} \cdot \left(C_{Li} - C_{i} \right) = 0$$
(22)

The dimensionless concentration y_i for species i is defined as the ratio between the concentration at the catalyst liquid interface, C_i , and the concentration in the bulk liquid phase, C_{Li} as $y_i = \frac{C_i}{C_{Li}}$.

Accordingly, Equation (22) can be expressed in the dimensionless form

$$y_{i} - \frac{v_{i} \cdot r \cdot \rho_{B}}{k_{LSi} \cdot a_{LS} \cdot C_{Li}} = 1$$
 (23)

Therefore, Equations for xylose and hydrogen ($\nu_i = -1$)in the interface can be expressed by Equations (24) and (25), respectively.

$$y_{X} + \frac{\rho_{B} \cdot \kappa_{X,363 \text{ K}} \cdot e^{\frac{E_{a}}{R} \cdot \left(\frac{1}{T} - \frac{1}{T}\right)} \cdot y_{X} \cdot C_{L_{H_{2}}} \cdot y_{H_{2}}}{\left(1 + K_{X} \cdot C_{L_{X}} \cdot y_{X}\right) \cdot \left(1 + \sqrt{C_{L_{H_{2}}} \cdot y_{H_{2}}}\right)^{2}} \cdot \frac{1}{k_{LSX} \cdot a_{LS}} = 1$$
(24)

$$y_{H_{2}} + \frac{\rho_{B} \cdot \kappa_{X, 363 \text{ K}} \cdot e^{\frac{E_{a}}{R} \cdot \left(\frac{1}{T} - \frac{1}{T}\right)} \cdot C_{L_{x}} \cdot y_{X} \cdot y_{H_{2}}}{\left(1 + K_{x} \cdot C_{L_{X}} \cdot y_{X}\right) \cdot \left(1 + \sqrt{C_{L_{H_{2}}} \cdot y_{H_{2}}}\right)^{2}} \cdot \frac{1}{k_{LSH_{2}} \cdot a_{LS}} = 1$$
(25)

The liquid–solid mass-transfer coefficient is inversely related to the thickness of the stagnant boundary layer, which is commonly expressed with the Sherwood number (Belfiore, 2003). Mohammed et. al. (Mohammed et al., 2014) developed an effective liquid–solid correlation for foam packings in three-phase reactors (Equation (25)), using a modified electrochemical limiting-current method. Their formulation defines an effective Sherwood number based on the foam window diameter, d_w as the characteristic length and explicitly embeds foam geometry of the foam structure through the product $a_{geo} \cdot d_w \cdot \frac{1-\epsilon}{\epsilon}$ as well as gas hydrodynamics via a gas Reynolds term (Re_G). Importantly, the wetting efficiency ϕ is intrinsic to this correlation. Consequently, the effective volumetric liquid–solid coefficient can be estimated directly from Equation (27). With values of the constants: a=0.13, b=0.805, c=-0.89, d=-1.34.

$$\varphi \cdot \operatorname{Sh} = a \cdot \operatorname{Re}_{L}^{b} \cdot \operatorname{Re}_{G}^{c} \left(a_{\operatorname{geo}} \cdot d_{\operatorname{w}} \cdot \frac{1 - \varepsilon}{\varepsilon} \right)^{d}$$
(26)

$$k_{LS} \cdot a_{LS} = \varphi \cdot k_{LS} \cdot a_{geo} = \varphi \cdot Sh \cdot \frac{\mathfrak{D}_{AB}}{d} \cdot a_{geo}$$
 (27)

3.6. External mass transfer: gas-liquid interface

Dedicated correlations for the gas–liquid (GL) mass-transfer coefficient on solid open-cell foams are scarce and often unreliable in the low-interaction domain under reactive conditions (Durante et al., 2014; Russo et al., 2015). We therefore adopt semi-empirical scaling that preserves key hydrodynamic dependences while avoiding out-of-range correlations. The volumetric gas-liquid coefficient relates to the Sherwood number as $k_{\rm GLi} = {\rm Sh} \cdot \mathfrak{D}_{\rm i,\,B}/{\rm L_c}$. Consistent with boundary-layer/penetration theory, Equation (28) is used.

$$Sh_{\text{average}} \approx d \cdot Re_L^e \cdot Sc^f$$
 (28)

The expression (28) does not include the gas-phase Reynolds number (Re $_{\rm G}$), since gas-liquid mass transfer in packed/foam beds shows weak sensitivity to gas hydrodynamics in the low-interaction regime (Turek and Lange, 1981; Zalucky et al., 2017; Zapico et al., 2016). Therefore, it is possible to establish a relationship between the liquid solid volumetric mass transfer coefficient of a given condition, $\binom{k_{\rm GLi} \cdot a_{\rm GL}}{j}$ with that of a reference $\binom{k_{\rm GLi} \cdot a_{\rm GL}}{k_{\rm REF}}$ using the exponents predicted by the boundary layer theory for the gas-liquid interface with zero shear, and perfect Slip (Belfiore, 2003), $e=\frac{1}{2},\ f=\frac{1}{2},$

$$\left(k_{GLi} \cdot a_{LG}\right)_{j} = \left(\frac{u_{j}}{u_{REF}}\right)^{\frac{1}{2}} \cdot \left(\frac{\mathfrak{D}_{j}}{\mathfrak{D}_{REF}}\right)^{\frac{1}{2}} \cdot \left(k_{GLi} \cdot a_{GL}\right)_{REF}$$
(29)

3.7. Solution strategy

The Danckwerts' closed boundary condition (Equation (30)) is applied at the inlet of the catalyst bed for the liquid-phase mass balance. This condition establishes that the net convective inflow at z=0 is equal to the sum of the convective and dispersive fluxes at the same position,

$$C_{\text{feed}} = C_{\text{L0}} - \frac{1}{\text{Pe}_{\text{ax}}} \cdot \frac{\text{d}C_{\text{Li}}}{\text{dz}}$$
(30)

At the outlet of the reactor (z=1), it is assumed that the concentration gradient vanishes, leading to the condition

$$\frac{\mathrm{dC}_{\mathrm{N}}}{\mathrm{dz}} = 0 \tag{31}$$

The first- and second-order spatial derivatives of the concentration are approximated using finite differences, as expressed in Equations (32) and (33):

$$\frac{dC_{Li}}{dz} = \frac{C_{L_{i+1}} - C_{L_{i-1}}}{2 \cdot \Delta z}$$
 (32)

$$\frac{d^{2}C_{Li}}{dz^{2}} = \frac{C_{L_{i+1}} - 2 \cdot C_{L_{i}} + C_{L_{i-1}}}{\Delta z^{2}}$$
(33)

The axial coordinate z is discretized into N nodes, and Equation (20) is rewritten accordingly, applying the corresponding boundary conditions.

The interface reaction rate in each node is approximated using a first-order Taylor expansion around the value at iteration k:

$$r\left(C_{j}\right) \approx r\left(C_{j}^{k}\right) + \frac{dr\left(C_{j}^{k}\right)}{dC} \left(C_{j}^{k+1} - C_{j}^{k}\right) \tag{34}$$

With the experimental steady-state xylose conversions, the value of $\left(k_{LGi} \cdot a_{LG}\right)_{REF}$ can be computed by minizine the objective function:

$$Q = \sum_{j=1}^{M} (X_{Exp} - X_{Calc})^{2}$$
 (35)

Where X_{Exp} and X_{Calc} are the experimental and calculated xylose conversion, respectively.

The general algorithmic structure for solving the system was implemented following the steps below.

- 1. Initialize matrices and vectors
 - Read input conditions for each experiment j: T, P, feed concentrations, liquid flow rate, Pe, residence time.
 - Calculate liquid holdup ε_{τ} from developed correlation
 - Initialize concentration profiles $C_i(z)$ along the reactor for each condition j.
 - Give an initial guess for the volumetric gas-liquid mass ($k_{LGi} \cdot a_{LG}$)
 - Calculate $\left(k_{LGi} \cdot a_{LG}\right)_{i}$ with Equation (29).
 - Calculate $(k_{LS} \cdot a_{LS})_{i}$ with Equation (27)
- 2. Node by node calculation for each experimental condition

For each node:

- 1. Compute the hydrogen saturation concentration from Equation (10).
- 2. Solve the interface balances to obtain the dimensionless concentrations y_x and $y_{\rm H_2}$ using Equations (24) and (25)).
- 3. Calculate the reaction rate using y_x and y_{H_x} .

- 4. Estimate the rate derivative with respect to concentration for the Jacobian which is needed in the finite-difference assembly.
- 5. Assemble the finite-difference equations: dispersion term + convection term + reaction term (Equation (17)).

3. Solve linear system

Update the liquid-phase concentrations along the reactor.

4. Convergence check

If the profiles are not converged, repeat the iteration.

5. Conversion

- Calculate the outlet conversion for each condition *j*.
- Evaluate the objective function (Equation 34).
- • Change ($k_{LGi} \cdot a_{LG})_{_{RFF}}$, steps 2-4, until the optimum is reached.

For the sake of comparison, also the plug flow model (18) was implemented.

4. Results and discussion

4.1. Continuous hydrogenation results: effect of process parameters

Different process parameters such as temperature, liquid flow rate, and feed concentration were systematically evaluated to determine the performance of the Ru/C foam catalysts in continuous xylose hydrogenation. Overall, the catalyst displayed a good stability on the time-on-stream and reusability as reflected by repeating experiments with the same catalyst.

The influence of temperature (60–120 °C) on xylose conversion and space-time yield (STY) is shown in Figure 4. Higher temperatures accelerate the intrinsic reaction rate, slightly increase the reactant diffusivity, and decrease the viscosity of the aqueous phase. Together, these effects enhance the transport of reactants to the catalyst surface, resulting in a steady rise in the STY with increasing temperature.

Because the experiments were conducted at a low liquid flow rate (0.25 mL/min), external mass-transfer resistance was significant, which explains the lower conversions compared to those expected in the intrinsic kinetic regime. The xylitol selectivity ranged from 99 % to 94 %, with arabitol as the main by-product and xylulose found in small concentrations at the higher temperatures (≤1%). The xylitol selectivity improved at lower temperatures, which is consistent with the higher activation energy for the by-product formation. The near-neutral pH (5–7) and

hydrogen-saturated conditions also suppressed the side reactions, favoring xylitol production (Araujo-Barahona et al., 2025; Fan et al., 2023b).

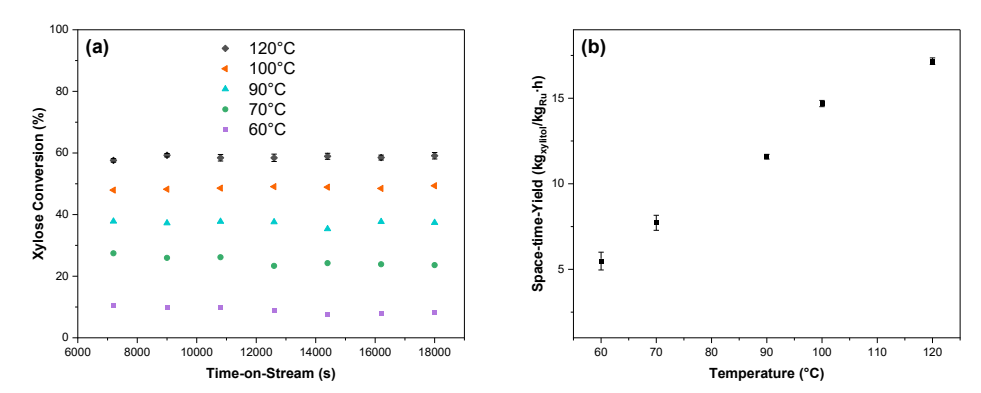


Figure 5. Effect of temperature on continuous xylose hydrogenation (0.13 M xylose, 0.25 mL/min, 6.6 mL/min H_2 at 20 bar): (a) xylose conversion vs. time-on-stream and (b) space–time yield (STY) at different temperatures.

Increasing the flow rate generally resulted in a lower conversion (Figure 4a). Higher liquid velocities reduce the residence time in the catalytic bed, which is critical for relatively slow reactions such as sugar hydrogenation, where a sufficient contact time is required to achieve high single-pass conversions. In addition, higher flow rates increase the liquid holdup in the bed, effectively reducing the catalyst-to-liquid ratio.

Conversely, higher flow rates improve the liquid-solid mass transfer by increasing the Reynolds number and enhancing the wetting of the foam catalyst. The combination of these effects explains the behavior observed in Figure 4b:

- STY rises as the flow rate increases from 0.25 to 0.75 mL min⁻¹, reflecting better catalyst utilization due to enhanced mass transfer.
- Beyond 0.75 mL/min, the STY reaches plateaus because the residence time becomes too short, and maldistribution or partial channeling in the shallow, narrow bed might limit the effective catalyst use.
- At 1.25 mL/min, the STY shows less stable behavior over time-on-stream.

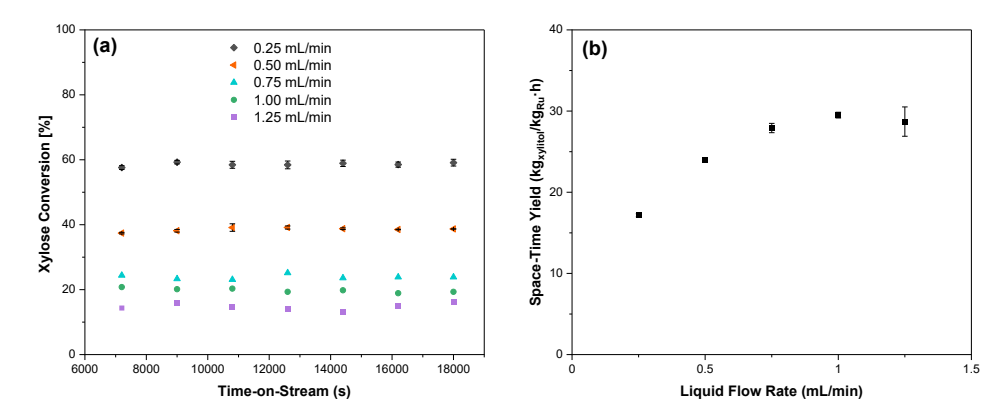


Figure 6. Effect of liquid flow rate on continuous xylose hydrogenation (120 °C , 0.13M, 0.25mL/min, 6.6 mL/min H_2 at 20 bar): (a) xylose conversion vs Time-on-stream and (b) Space-Time yield (STY) at different liquid flow rates.

The effect of the feed concentration on xylose hydrogenation is presented in Figure 5. The conversion decreased with an increasing inlet concentration of xylose. This trend can be attributed to stronger product adsorption, which hinders the reactant access to active sites, and to increased liquid viscosity at higher concentrations. The increase in viscosity lowers the Reynolds number and therefore reduces the liquid–solid mass transfer. Additional contributing factors may include a decrease in hydrogen solubility.

Despite the lower conversion, the space-time yield (STY) increased as the feed concentration rose from 0.13 M to 0.26 M, reflecting the higher inlet throughput. At the feed concentration 0.39 M, the STY remained approximately constant, likely due to the combined effects of mass transfer limitations, reduced solubility, and reactant adsorption.

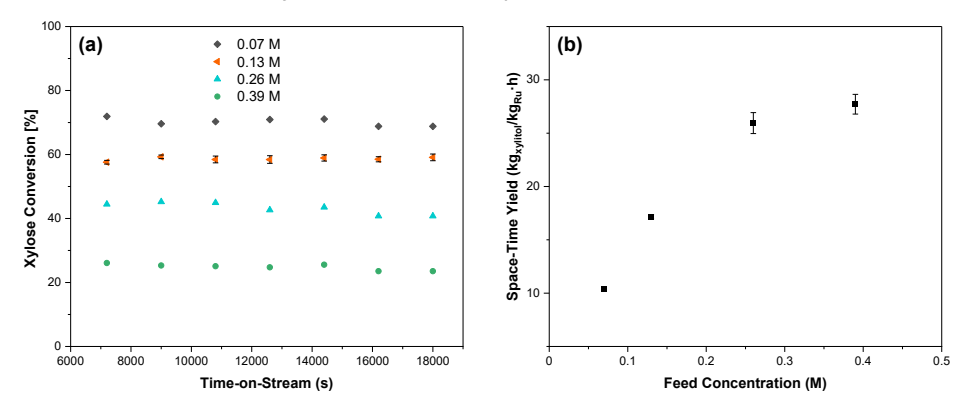


Figure 7. Effect of feed concentration on continuous xylose hydrogenation (120 °C, 0.25 mL/min, 6.6 mL/min $\rm H_2$ at 20 °C): (a) xylose conversion vs. time-on-stream and (b) space-time yield (STY) at different concentrations.

It can be concluded that temperature, feed concentration, and liquid flow rate are the key parameters governing the performance of xylose hydrogenation on Ru/C foam catalysts in the trickle bed configuration. Their effects arise from the interplay of intrinsic kinetics, mass transfer limitations, and hydrodynamics. Higher temperatures enhance the reaction rates, and diffusivity, but slightly decrease the product selectivity, while increased flow rates improve the liquid-solid mass transfer but reduce the residence time and effective catalyst concentration per liquid volume. The feed concentration directly affects both the kinetics and mass transfer by altering the viscosity, solubility, and adsorption. The combination of these factors determines the conversion, selectivity, and space-time yield. Efficient operation of foam-based trickle bed reactors therefore requires balancing temperature, liquid velocity, and feed concentration to minimize the mass-transfer limitations while maintaining a sufficiently long residence time and efficient catalyst utilization. In addition to the favorable performance metrics, the catalyst demonstrated remarkable stability under the operating conditions studied. The activity remained nearly constant during extended time-on-stream experiments, with no noticeable deactivation trends, and the selectivity was preserved across multiple runs. Overall, the prepared catalyst displayed excellent stability on the time-on-stream as is reflected by the conversion profiles displayed in this section (Figures 5-7) and reusability as can be observed by the error bar of the repeated experiments.

4.2. Modelling results

4.2.1. Flow pattern characterization

The residence time distribution (RTD) experiments displayed a clear evolution of the bed hydrodynamics with an increasing liquid flow rate. At $0.25\,\mathrm{mL/min}$ (Figure 8 (a)), the reactor displayed the longest mean residence time (1344 s) and the broadest RTD (variance = 1641 s²), with an effective axial Péclet number of 35.7, indicative a relatively high axial dispersion. Increasing the flow rate to $0.50\,\mathrm{mL\,min^{-1}}$ and $0.75\,\mathrm{mL\,min^{-1}}$ (Figures 6(b)-(c)) sharply reduced both the mean residence time (731 s and 504 s) and variance (396 s² and 198 s²), while raising the Péclet number to 43.9 and 41.5. These conditions correspond to a narrower residence time distribution and lower relative dispersion, as convective transport dominates over axial diffusion. At 1 ml/min (Figure 8(d)), the mean residence time dropped to 360 s and the variance reached its minimum (120 s²), but the Péclet number decreased again to 35.4. This result reflects that, despite the narrow absolute RTD, the short residence time amplifies the relative influence of local maldistribution or bypassing, making axial dispersion comparatively more significant. Overall, the RTD analysis shows a transition from a broad, more dispersive flow pattern at low flow rates to

convectively dominated behavior at intermediate rates, followed by a high-flow regime where the reduced residence time increases the sensitivity to axial mixing.

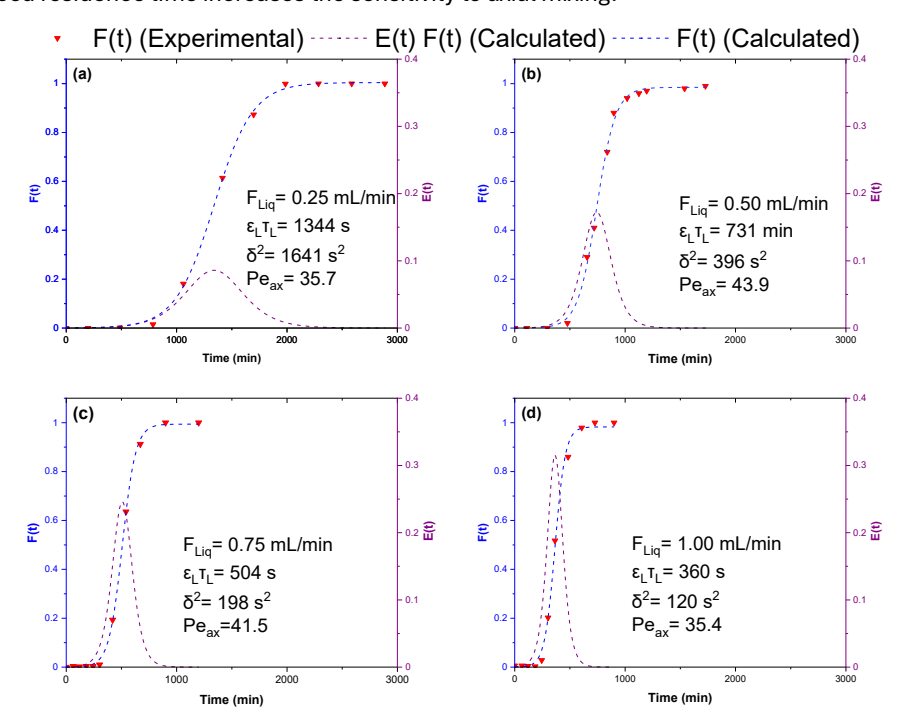


Figure 8. Step-response experiments at different liquid flow rates using xylitol as tracer. Conditions: 120 °C, 6.6 ml H₂/min (20 bar).

4.2.1. Liquid holdup

The liquid holdup in the reactor packing, as described in Section 2.3, as well as in a bed exclusively filled with Ru/C solid foam, was evaluated by a gravimetric water recirculation method (Section 2.5). The retained water at different liquid flow rates is presented in Figure 9a. For the highest liquid flow rate (2.00 mL/min), the bed was allowed to stabilize for a longer time to promote wetting. As the flow rate decreased, a progressive reduction in retained water was observed for both configurations. Among the parameters studied, the liquid flow rate was the most decisive factor influencing the liquid holdup. In general, increasing pressure tends to increase the liquid holdup (see Supplementary Data).

The solid foam catalyst bed retained more water than the mixed bed of sand and foams, which is expected because of the higher void fraction of the solid foams (~0.91) compared to quartz sand (~0.40), the latter reducing the overall liquid holdup. Nevertheless, both beds displayed similar variations with the process parameters.

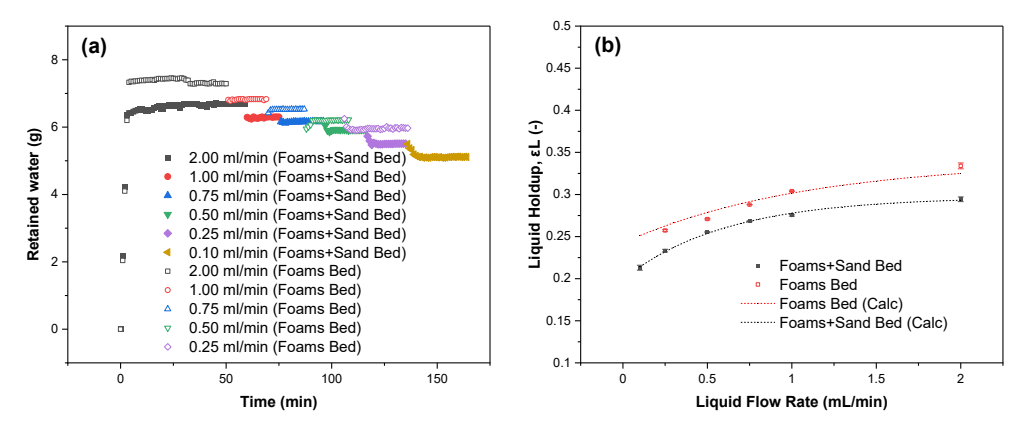


Figure 9. Liquid holdup in the total bed and in the Ru/C bed at 90 °C under 6.6 mL/min He flow at 20 bar: (a) effect of liquid flow rate on retained water, and (b) effect of liquid flow rate on the liquid holdup.

The experimental data were fitted using the correlation proposed by García-Serna et al. (2017), Equation (36), which accounts for the negative influence of increasing gas mass velocity (G') and the positive effects of pressure (P) and liquid mass velocity (L') on the liquid holdup. The fitting provided good agreement with the experiments, and the obtained parameters were consistent with those reported in the literature (listed in Table 2).

$$\varepsilon_{L} = \left[a_{\varepsilon_{L}} + b_{\varepsilon_{L}} \left(1 - e^{-c_{\varepsilon_{L}} \cdot L'} \right) \right] \cdot \left(\frac{P}{G'} \right)^{d_{\varepsilon_{L}}}$$
(36)

Table 2. Fitting parameters for the liquid holdup.

Reactor bed type Parameter		Value	
	a_{ϵ_L}	0.032	
	b_{ϵ_L}	0.013	
Foams bed	$c_{\epsilon_{L}}$	4.53	
	d_{ϵ_L}	0.100	
	R^2	95.8%	
	a_{ϵ_L}	0.012	
	b_{ϵ_L}	0.006	
Foam + Sand bed	$c_{\epsilon_{L}}$	7.95	
	d_{ϵ_L}	0.140	
	R^2	99.7%	

4.2.2. Modeling reactor results

The experimental data were fitted with the methodology described in Section 3.7 to quantify the roles of gas-liquid (G-L) and liquid-solid (L-S) mass transfer using both the axial-dispersion model (ADM) and the plug flow model (PFR). The overall agreement is illustrated in Figure 10. Both models capture the experimental trends well. Because the dispersion effect on this system is significant but not dominant, including axial dispersion changes the predicted conversions only modestly; its impact becomes even less relevant at lower temperatures, where the Langmuir–Hinshelwood-type rate tends towards zero-order in xylose, so axial mixing has modest leverage on the outlet composition. Under the low-conversion conditions, the adsorption terms and thus interfacial transport become more influential.

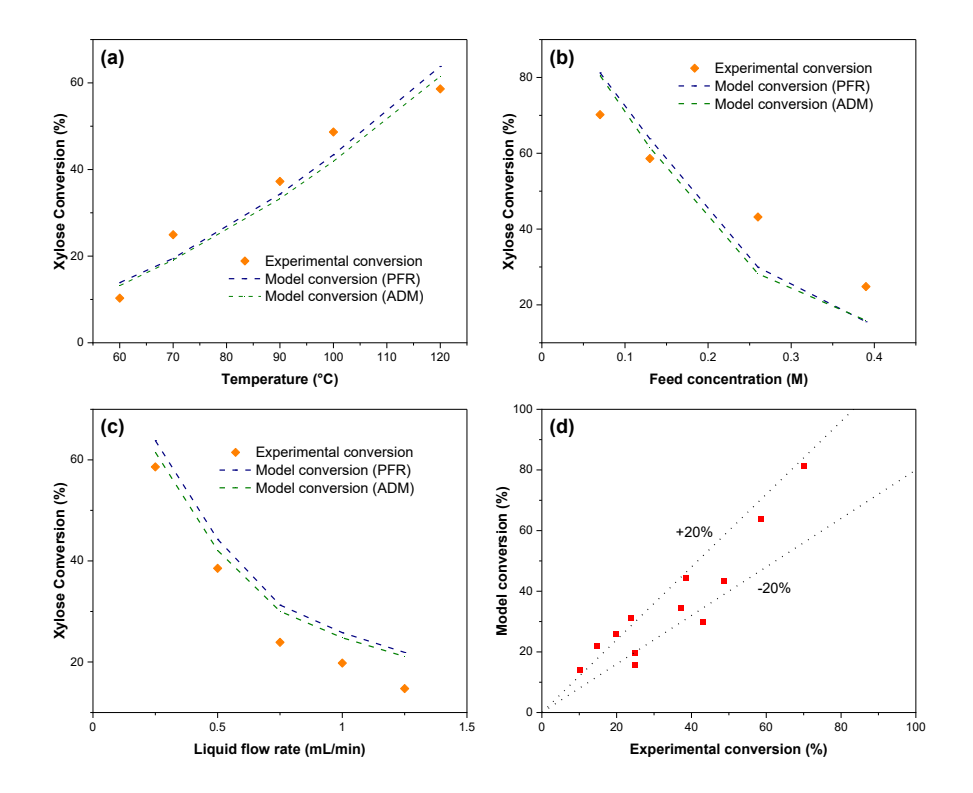


Figure 10. Experimental conversion data and model predictions (PFR and ADM), both including external G-L and L-S mass-transfer resistances: (a) temperature effect (0.13 M xylose, 0.25 mL/min liquid, 6.6 mL/min H2, 20 bar); (b) liquid-flow-rate effect (120 °C, 0.13 M xylose, 6.6 mL/min H2, 20 bar); (c) feed-concentration effect (120 °C, 0.25 mL/min liquid, 6.6 mL/min H2, 20 bar); and (d) parity plot of experimental versus predicted conversions.

The single fitted parameter in the PFR framework — taken as a reference the gas-liquid volumetric mass transfer coefficient ($k_{GLH_2} \cdot a_{GL}$) at the reference state (100 °C, 0.25 mL/min and 0.13M xylose) appears in Table 3. The estimate is 0.022 s⁻¹ (95% CI: 0.014–0.049 s⁻¹). This value is of the same order as the liquid-solid volumetric mass transfer coefficient for hydrogen $k_{LSH_2} \cdot a_{LS}$ predicted by the used correlation (Equation 27), indicating that the gas-liquid mass transfer resistance is comparable to, and often slightly more limiting than, the liquid-solid mass transfer resistance for H_2 in this system. Similar observations have been reported previously for packed bed reactors operating at the low-interaction regime for sugar hydrogenation (Durante et al., 2014; Russo et al., 2015).

Table 3. Fitting parameter for the axial dispersion model considering gas-liquid and liquid-gas mass transfers.

Parameter	Value	95% CI	Units
$\left(\left. \mathrm{k}_{\mathrm{GLH}_2} \cdot \mathrm{a}_{\mathrm{GL}} \right)_{\mathrm{REF}} \right.$	0.022	[0.014,0.049]	S ⁻¹
RMSE	6.60	-	%
R^2	85.63	-	-

To interpret the mass transfer effect across various process conditions, Table 4 reports the resistances $\lambda = \frac{1}{k_i \cdot a_p}$ [s] for L-S xylose (λ_{LSX}), L-S hydrogen (λ_{LSH_2}), and G-L hydrogen (λ_{GLH_2}). From

those values several trends can be deducted:

At a fixed flow rate, the mass transfer resistances increase as the temperature decreases, which is consistent with reduced diffusivities and lower Reynolds numbers (higher viscosity). However, the impact of the resistances on the overall reactor performance is less pronounced at lower temperatures because the reaction rate and interfacial driving forces are smaller, so even large resistances generate small fluxes as can be observed in the superficial concentration profiles displayed in Figure 11.

The mass transfer resistance shows a viscosity-driven trend: increasing the concentration raises the viscosity, which lowers the Reynolds and, therefore, Sherwood number, which reduces the overall mass transfer coefficient. In the present dataset this effect is non-monotonic (a decrease at 0.26 M followed by an increase at 0.39 M), suggesting competing effects of viscosity, wetting/area utilization, and changes in local driving forces.

Increasing the liquid flow rate enhances convection and typically reduces the film thickness, which increases the mass transfer coefficient but also can influence the effective wetting of the catalyst. Recent research on solid foams has shown that in co-current downflow, the wetting efficiency of the foam can be compromised by several hydrodynamic and design factors such as initial flow distribution, foam morphology and pre-wetting methods. It is expected that under the screened conditions the wetness efficiency could have played an important role in the observed mass transfer limitations. Further research is necessary to separate the effects under reacting conditions.

Table 4. Mass transfer resistances for the different experimental conditions predicted with the PFR model.

T (°C)	F (mL/min)	C _{feed} (M)	$\lambda_{\mathrm{LSX}}(s)$	$\lambda_{\mathrm{LSH}_2}(\mathbf{s})$	$\lambda_{\mathrm{GLH}_2}(\mathbf{s})$
60	0.25	0.13	117.5	57.5	62.1
70	0.25	0.13	94.3	46.1	56.9
90	0.25	0.13	62.9	30.8	48.8
100	0.25	0.13	52.4	25.6	45.6
120	0.25	0.13	37.3	18.3	40.3
120	0.5	0.13	21.4	10.5	28.5
120	0.75	0.13	15.4	7.5	23.3
120	1.00	0.13	12.2	6.0	20.2
120	1.25	0.13	10.2	5.0	18.0
120	0.25	0.07	34.2	16.7	40.3
120	0.25	0.26	43.1	21.1	40.3
120	0.25	0.39	48.1	23.5	40.3

Figure 11 displays the dimensionless concentration of the reacting species in the liquid-solid interface at different temperatures. In all cases the hydrogen interfacial fraction $y_{\rm H2}$ is lower than the xylose fraction $y_{\rm x}$. While the xylose profile remained relatively flat across the reactor length—with a slight decreasing trend near the outlet at higher temperatures, the hydrogen interfacial concentration showed a more complex behavior: it initially decreased in the vicinity of the reactor inlet, followed by a gradual increase toward the outlet.

These trends can be explained by the form of the interfacial mass balances at the liquid-solid boundary and the liquid-gas mass transfer limitations. First, since the gas-liquid transfer of

hydrogen is finite, the amount of dissolved hydrogen does not necessarily reach the maximal solubility, $C_{1\,i}^{sat}$ as shown below,

$$C_{L_{H_{2}}} = C_{L_{H_{2}}}^{\text{sat}} - \frac{r_{v}}{k_{GL_{H_{2}}} \cdot a_{LG}}$$
(37)

Then, the balances in the liquid-solid interface, as described by Equations (23) and (24) can be rearranged substituting $r_{\nu} = r \cdot \rho_{R}$ and $\nu_{i} = -1$,

$$y_{H_{2}} = 1 - \frac{r_{v}}{k_{LSH_{2}} \cdot a_{LS} \cdot \left(C_{LH_{2}}^{sat} - \frac{r_{v}}{k_{GLH_{2}} \cdot a_{GL}}\right)}$$
(38)

$$y_{X} = 1 - \frac{r_{v}}{k_{LSX} \cdot a_{LS} \cdot C_{L_{X}}}$$
(39)

Then, dividing Equations (36) and (37) and rearranging gives the ratio

$$\frac{1 - y_{H_2}}{1 - y_X} = \frac{k_{LSX} \cdot C_{L_X}}{k_{LSH_2} \cdot \left(C_{LH_2}^{\text{sat}} - \frac{r_v}{k_{GLH_2} \cdot a_{GL}}\right)}$$
(40)

Since the bulk concentration of xylose generally is higher than that of hydrogen (due to limited hydrogen solubility and transport), $C_{Lx} >> C_{LH_2}$ and the liquid-solid transport of hydrogen is higher than xylose transport, $k_{LSH_2} > k_{LSX}$. Therefore, the right-hand side of Equation (40) is generally larger than 1, which implies that $1-y_{H_2} > 1-y_X$, thus, $y_{H_2} < y_X$ as it is observed. The axial trends follow directly. Close to the reactor inlet C_{L_X} is high, so r_v is high too, then according to Equation (38) y_{H_2} should decrease. This explains the initial drop in y_{H_2} . Downstream, as xylose is consumed, C_{L_X} and r_v decrease; the hydrogen bulk concentration $C_{L_H_2}$ recovers toward $C_{LH_2}^{sat}$, causing the progressive increase of y_{H_2} .

At the highest temperatures, the reaction rater is significantly enhanced, leading to a lower average y_X across the reactor (see Equation (38)). As the reaction progresses axially, the consumption of xylose reduces C_{L_X} , which in turn lowers the reaction rate r_v . According to Equation (39), this causes a slight increase in y_X . Towards the reactor outlet, however, the increasing interfacial hydrogen concentration y_{H2} enhances the reaction rate again, leading to a modest decrease in y_X as the reactor outlet is approached.

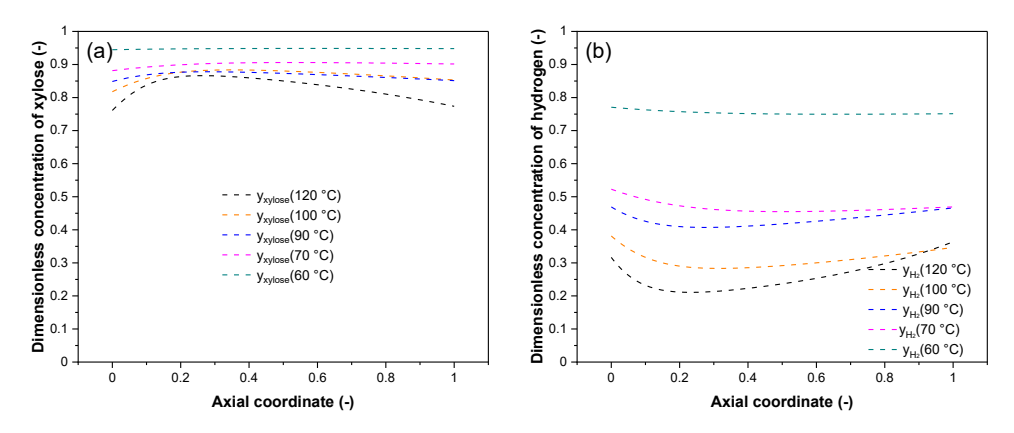


Figure 11. Dimensionless axial concentration profiles for xylose (a) and hydrogen (b) in the liquid-solid interface.

Overall, these results confirm that mass transfer resistance exerts a dominant influence on the performance of foam-based reactors under the studied downflow conditions. While the open structure of foams suppresses the retarding effect of internal diffusion and reduces the pressure drop, external resistances — particularly at the liquid–solid interface — remain critical. Future work should focus on configurations that alleviate these limitations, such as upflow operation (Zalucky et al., 2017) or improved liquid distribution strategies, to assess the potential of foam catalysts for continuous sugar hydrogenation under conditions closer to the regime of intrinsic kinetics.

5. Conclusions and future perspectives

This work demonstrates the feasibility of using Ru/C solid foam catalysts for the continuous hydrogenation of xylose to xylitol under trickle-bed conditions, while providing a comprehensive analysis of the hydrodynamic and transport phenomena that govern reactor performance. The prepared foam catalysts remain active and selective over repeated operation in a parallel screening reactor, with xylitol selectivity consistently above 94 %.

Residence time distribution and liquid holdup studies revealed that reactor hydrodynamics evolve significantly with flow rate. At low liquid velocities, broad RTDs and relatively high dispersion coefficients reflect considerable back mixing, whereas intermediate flows reduced relative dispersion and brought the system closer to plug-flow behavior. At high velocities, however, the short residence time amplified the impact of local maldistribution, indicating that reactor configuration and liquid distribution strategies remain critical for reliable scale-up.

The kinetic-transport model, based on the non-competitive adsorption concept coupled with axial dispersion and interfacial resistances, successfully reproduced the experimental trends. The fitted gas-liquid mass transfer coefficient was of the same order as the liquid-solid transfer coefficient for hydrogen, demonstrating that both steps are of comparable importance under the low-interaction regime characteristic of trickle bed operation in laboratory scale. The analysis of resistances highlighted that the liquid-solid transport of hydrogen represents a prevalent limitation, particularly at higher concentrations and flow rates where the liquid viscosity and wetting efficiency play a decisive role.

In general, the study underscores that while solid foams overcome the key limitations of conventional catalyst pellets, such as internal diffusion resistance and pressure drop, the external transport resistances remain significant and can overshadow intrinsic kinetics. To fully exploit the potential of foam catalysts, future research should focus on various reactor configurations and operating modes that enhance wetting and interfacial transport, such as upflow operation and the use of improved liquid distributors. These insights provide a framework for guiding the design of structured catalysts in three-phase sugar hydrogenation as well as other catalytic three-phase processes and contribute to bridging the gap between laboratory studies and industrial applications.

References

Aguirre, A., Chandra, V., Peters, E.A.J.F., Kuipers, J.A.M., Neira D'Angelo, M.F., 2020. Open-cell foams as catalysts support: A systematic analysis of the mass transfer limitations. Chemical Engineering Journal 393, 124656. https://doi.org/10.1016/J.CEJ.2020.124656

Akhtar, M.S., Naseem, M.T., Ali, S., Zaman, W., 2025. Metal-Based Catalysts in Biomass Transformation: From Plant Feedstocks to Renewable Fuels and Chemicals. Catalysts 2025, Vol. 15, Page 40 15, 40. https://doi.org/10.3390/CATAL15010040

Al-Dahhan, M.H., Larachi, F., Dudukovic, M.P., Laurent, A., 1997. High-Pressure Trickle-Bed Reactors: A Review. Ind Eng Chem Res 36, 3292–3314. https://doi.org/10.1021/ie9700829

Araujo-Barahona, G., De Simone, M., Brunberg, C., Eränen, K., Reinsdorf, A., Roos, M., García-Serna, J., Russo, V., Murzin, D.Y., Salmi, T., 2025. Solid raney-type Ni foam catalysts for xylitol production: Continuous and batch operation. Appl Catal A Gen 701, 120324. https://doi.org/10.1016/j.apcata.2025.120324

Araujo-Barahona, G., Eränen, K., Oña, J.P., Murzin, D., García-Serna, J., Salmi, T., 2022. Solid Foam Ru/C Catalysts for Sugar Hydrogenation to Sugar Alcohols-Preparation, Characterization, Activity, and Selectivity. Ind Eng Chem Res 61, 2734–2747. https://doi.org/10.1021/acs.iecr.1c04501

Araujo-Barahona, G., Goicoechea-Torres, A., Eränen, K., Latonen, R.M., Tirri, T., Smeds, A., Murzin, D., García-Serna, J., Salmi, T., 2023. Kinetic studies of solid foam catalysts for the production of sugar alcohols: Xylitol from biomass resources. Chem Eng Sci 281. https://doi.org/10.1016/j.ces.2023.119130

Belfiore, L.A., 2003. Dimensional Analysis of the equations of Change for Fluid Dynamics Within the Mass Transfer Boundary Layer. Transport Phenomena for Chemical Reactor Design 361–368. https://doi.org/10.1002/0471471623.CH12

Besson, M., Gallezot, P., Pinel, C., 2014. Conversion of biomass into chemicals over metal catalysts. Chem Rev 114, 1827–1870. https://doi.org/10.1021/cr4002269

Cognet, P., Berlan, J., Lacoste, G., Fabre, P.L., Jud, J.M., 1995. Application of metallic foams in an electrochemical pulsed flow reactor Part I: Mass transfer performance. J Appl Electrochem 25, 1105–1112. https://doi.org/10.1007/BF00242537

da Fonseca Dias, V., da Silva, J.D., 2022. An experimental investigation of gas-liquid-solid transfer and external wetting efficiency on open-cell foam in a three-phase packed bed reactor: validation and parameter estimation. Brazilian Journal of Chemical Engineering 39, 87–104. https://doi.org/10.1007/s43153-021-00217-z

Durante, D., Kilpiö, T., Suominen, P., Herrera, V.S., Wärnå, J., Canu, P., Salmi, T., 2014. Modeling and simulation of a small-scale trickle bed reactor for sugar hydrogenation. Comput Chem Eng 66, 22–35. https://doi.org/10.1016/J.COMPCHEMENG.2014.02.025

Fan, H., Fang, Z., Zhao, X., Hu, Y., Li, B., Yang, W., Li, M., Wang, J., Lu, X., Song, W., Fu, J., 2023a. Continuous Hydrogenation of Maltose over Raney Ni in a Trickle-Bed Reactor. Ind Eng Chem Res 62, 15395–15405. https://doi.org/10.1021/acs.iecr.3c01723

García, B., Orozco-Saumell, A., López Granados, M., Moreno, J., Iglesias, J., 2021. Catalytic Transfer Hydrogenation of Glucose to Sorbitol with Raney Ni Catalysts Using Biomass-Derived Diols as Hydrogen Donors. ACS Sustain Chem Eng 9, 14857–14867. https://doi.org/10.1021/acssuschemeng.1c04957

García-Serna, J., Gallina, G., Biasi, P., Salmi, T., 2017. Liquid Holdup by Gravimetric Recirculation Continuous Measurement Method. Application to Trickle Bed Reactors under Pressure at Laboratory Scale. Ind Eng Chem Res 56. https://doi.org/10.1021/acs.iecr.7b01810

Gianetto, A., Specchia, V., 1992. Trickle-bed reactors: state of art and perspectives. Chem Eng Sci 47, 3197–3213. https://doi.org/10.1016/0009-2509(92)85029-B

Ho, P.H., Ambrosetti, M., Groppi, G., Tronconi, E., Palkovits, R., Fornasari, G., Vaccari, A., Benito, P., 2019. Structured Catalysts-Based on Open-Cell Metallic Foams for Energy and Environmental Applications. Stud Surf Sci Catal 178, 303–327. https://doi.org/10.1016/B978-0-444-64127-4.00015-X

Huu, T.T., Lacroix, M., Pham Huu, C., Schweich, D., Edouard, D., 2009. Towards a more realistic modeling of solid foam: Use of the pentagonal dodecahedron geometry. Chem Eng Sci 64, 5131–5142. https://doi.org/10.1016/J.CES.2009.08.028

Lali, F., 2016. Characterization of foam catalysts as packing for tubular reactors. Chemical Engineering and Processing: Process Intensification 105, 1–9. https://doi.org/10.1016/J.CEP.2016.04.001 Lali, F., Gärtner, S., Haase, S., Lange, R., 2015. Preparation Method for Ruthenium Catalysts Supported by Carbon-Coated Aluminum Foams. Chem Eng Technol 38, 1353–1361. https://doi.org/10.1002/ceat.201400676

Mallesham, B., Raikwar, D., Shee, D., 2020. The role of catalysis in green synthesis of chemicals for sustainable future. Advanced Functional Solid Catalysts for Biomass Valorization 1–37. https://doi.org/10.1016/B978-0-12-820236-4.00001-5

Mikkola, J.P., Salmi, T., Sjöholm, R., 1999. Kinetic and Mass-transfer Effects in the Hydrogenation of Xylose to Xylitol. Stud Surf Sci Catal 122, 351–358. https://doi.org/10.1016/S0167-2991(99)80166-9

Mogi, N., Sugai, E., Fuse, Y., Funazukuri, T., 2007. Infinite dilution binary diffusion coefficients for six sugars at 0.1 MPa and temperatures from (273.2 to 353.2) K. J Chem Eng Data 52. https://doi.org/10.1021/je0601816

Mohammed, I., Bauer, T., Schubert, M., Lange, R., 2014. Liquid–solid mass transfer in a tubular reactor with solid foam packings. Chem Eng Sci 108, 223–232. https://doi.org/10.1016/J.CES.2013.12.016

Najarnezhadmashhadi, A., Braz, C.G., Russo, V., Eränen, K., Matos, H.A., Salmi, T., 2022. Modeling of three-phase continuously operating open-cell foam catalyst packings: Sugar hydrogenation to sugar alcohols. AIChE Journal 68, e17732. https://doi.org/10.1002/aic.17732

Najarnezhadmashhadi, A., Wärnå, J., Eränen, K., Trajano, H.L., Murzin, D., Salmi, T., 2021. Modelling of kinetics, mass transfer and flow pattern on open foam structures in tubular reactors: Hydrogenation of arabinose and galactose on ruthenium catalyst. Chem Eng Sci 233, 116385. https://doi.org/10.1016/J.CES.2020.116385

National Institute of Standards and Technology, n.d. NIST Chemistry WebBook, SRD 69 [WWW Document]. URL https://webbook.nist.gov/chemistry/fluid/ (accessed 8.17.25).

B.E. Poling, J.M. Prausnitz, J. P. O'Connell, R.C. Reid, The properties of gases and liquids, Mcgraw-Hill, New York, 2001.

Russo, V., Kilpiö, T., Di Serio, M., Tesser, R., Santacesaria, E., Murzin, D.Y., Salmi, T., 2015. DynamicAl non-isothermal trickle bed reactor with both internal diffusion and heat conduction: Sugar hydrogenation as a case study. Chemical Engineering Research and Design 102, 171–185. https://doi.org/10.1016/J.CHERD.2015.06.011

Salmi, T., Murzin, D.Y., Mikkola, J.P., Wärnå, J., Mäki-Arvela, P., Toukoniitty, E., Toppinen, S., 2004. Advanced kinetic concepts and experimental methods for catalytic three-phase processes. Ind Eng Chem Res 43, 4540–4550. https://doi.org/10.1021/ie0307481

Shen, H., Ye, Q., Meng, G., 2018. The Simplified Analytical Models for Evaluating the Heat Transfer Performance of High-Porosity Metal Foams. Int J Thermophys 39, 1–14. https://doi.org/10.1007/S10765-018-2405-0 Sifontes Herrera, V.A., Rivero Mendoza, D.E., Leino, A.R., Mikkola, J.P., Zolotukhin, A., Eränen, K., Salmi, T., 2016a. Sugar hydrogenation in continuous reactors: From catalyst particles towards structured catalysts. Chemical Engineering and Processing - Process Intensification 109, 1–10. https://doi.org/10.1016/J.CEP.2016.07.007

Stemmet, C.P., 2008. Gas-liquid solid foam reactors: hydrodynamics and mass transfer. https://doi.org/10.6100/IR635735

Turek, F., Lange, R., 1981. Mass transfer in trickle-bed reactors at low reynolds number. Chem Eng Sci 36, 569–579. https://doi.org/10.1016/0009-2509(81)80145-5

Wisniak, J., Hershkowitz, M., Leibowitz, R., Stein, S., 1974. Hydrogen Solubility in Aqueous Solutions of Sugars and Sugar Alcohols. J Chem Eng Data 19. https://doi.org/10.1021/je60062a008

Zalucky, J., Wagner, M., Schubert, M., Lange, R., Hampel, U., 2017. Hydrodynamics of descending gas-liquid flows in solid foams: Liquid holdup, multiphase pressure drop and radial dispersion. Chem Eng Sci 168, 480–494. https://doi.org/10.1016/J.CES.2017.05.011

Zapico, R.R., Marín, P., Díez, F. V., Ordóñez, S., 2016. Liquid hold-up and gas–liquid mass transfer in an alumina open-cell foam. Chem Eng Sci 143, 297–304. https://doi.org/10.1016/J.CES.2016.01.008

Acknowledgement

This work was funded by the Research Council of Finland through the Academy Professor grant 319002 (Tapio Salmi) and Åbo Akademi University GSCE 2022 (German Araujo Barahona).

Notation

Symbol	Description	Units	
A	Reactor cross-sectional area	m²	
$a_{ m GL}$	Gas–liquid interfacial area per reactor volume	m²/m³	
a _{LS}	Liquid–solid interfacial area per reactor volume	m²/m³	
as	Geometric external surface area of foam per volume	m²/m³	
C_{H_2}	Hydrogen concentration in the liquid phase	mol/m³	
$\mathrm{C}^{\mathrm{sat}}_{\mathrm{H}_2}$	Hydrogen solubility (saturation) in the liquid phase	mol/m³	
C _i	Concentration of species is in the liquid (bulk)	mol/m³	
C_{L_i}	Concentration of species i at the liquid–solid interface	mol/m³	
C_{L_X}	Xylose concentration	mol/m³	
D _{ax}	Axial dispersion coefficient (liquid phase)	m²/s	
\mathfrak{D}_i	Molecular diffusivity of species i in water	m²/s	
\mathfrak{D}_{i,H_2O}	Diffusivity of i in water (explicit form)	m²/s	
E(t)	Residence time distribution (RTD) density function	-	
E _a	Activation energy	J/mol	
F(t)	Cumulative RTD function	_	
G'	Superficial gas velocity (as used in holdup correlations)	kg/(m²⋅s)	
k _{GL}	Gas–liquid mass transfer coefficient	m/s	
$k_{GL} \cdot a_{GL}$	Volumetric gas–liquid mass transfer coefficient	s ⁻¹	
K_{H_2}	Hydrogen adsorption parameter	m³⋅mol ⁻¹	
k _{LS}	Liquid–solid mass transfer coefficient	m/s	
$k_{LS} \cdot a_{LS}$	Volumetric liquid–solid mass transfer coefficient	s ⁻¹	
K _X	Xylose adsorption parameter	m³⋅mol ⁻¹	
ℓ	Reactor length	m	
L	Total Reactor length	m	
L _c	Characteristic length (e.g., for Pe)	m	
L'	Superficial mass velocity of liquid (as used in holdup	kg/(m²·s)	
	correlations)	NB/ (111 3 <i>)</i>	
M _{H2} O	Molar mass of water	g/mol	
m ₀	Initial amount of water in bed	kg	
m _L	Mass registered in scale during liquid holdup experiments	kg	
n _{i, in}	Molar flow rate of i reactor's inlet	mol/s	

n i, out	Molar flow rate of i reactor's outlet	mol/s
N_{GLi}	Molar flux of i across the G–L interface (towards liquid)	mol/(m²·s)
N _{LSi}	Molar flux of i across the L–S interface (towards solid)	mol/(m²·s)
P	Pressure	Pa
Pe	Péclet number	-
Q	Objective function for parameter estimation	-
R	Universal gas constant	J/(mol·K)
Re	Reynolds number $\operatorname{Re} = \left(\rho \cdot u \cdot L_{c} \right) / \mu$	_
r	Reaction rate per mass of Ru	mol/(kg _{Ru} ⋅s)
r _v	Volumetric reaction rate	mol/(m³·s)
s(t)	Tracer signal at reactor outlet	a.u.
Sc	Schmidt number $Sc = \mu / (\rho \cdot \mathfrak{D}_i)$	_
Sh	Sherwood number $Sh = (k_c \cdot L_c) / \mathfrak{D}_i$	_
STY	Space–time yield	Kg _{xylitol} /(kg _{Ru} ·h)
s ₀	Baseline tracer signal (before step input)	a.u.
S _∞	Asymptotic tracer signal (after step input)	a.u.
T	Absolute temperature	K
T	Reference temperature	K
ŧ	Mean residence time	S
uz	Superficial liquid velocity	m⋅s ⁻¹
V_{Bed}	Total packed-bed volume	m³
V_L	Liquid hold-up volume (from holdup experiments)	m³
$V_{m,i}$	Molar volume (e.g., used in Wilke–Chang)	m³/(mol)
X _s	Xylose weight fraction	wt.%
X _{Calc}	Calculated conversion	
X_{Exp}	Experimental conversion	
y _i	Dimensionless interfacial concentration of i in the L-S	_
1	interface	
Z	Axial coordinate (dimensionless)	
β_0^{sat}	Baseline level of hydrogen solubility correlation	-
β_1^{sat}	Main temperature (Arrhenius-like) effect in hydrogen	K

βsat	Extra temperature curvature in hydrogen solubility		
β_2^{sat}		_	
	correlation		
β_3^{sat}	Effect of xylose concentration in hydrogen solubility	L/mol	
Ρ ₃	correlation		
β_4^{sat}	Temperature–concentration interaction in hydrogen	L·K/mol	
Ρ ₄	solubility correlation		
β_5^{sat}	Pressure non-ideality correction in hydrogen solubility	1/bar	
P ₅	correlation	i/bai	
ε	Bed void fraction	-	
$\epsilon_{ m L}$	Liquid holdup in the bed	-	
к _{х, 363 к}	Kinetic parameter (non-competitive adsorption model)	m ⁶ /(kg _{Ru} ·mol·s)	
μ	Liquid viscosity	Pa·s	
$\mu_{\mathrm{H_2O}}$	Water viscosity	Pa·s	
ρ_{B}	Apparent bulk density of catalyst in the bed	kg _{Ru} /m³	
ρ_{G}	Gas density	kg/m³	
$ ho_{ m L}$	Liquid density	kg/m³	
σ^2	RTD variance (dimensional)	s ²	
σ_{θ}^2	Dimensionless RTD variance	-	
$ au_{ m L}$	Hydraulic residence time	S	
$\Phi_{\mathrm{H_2O}}$	Association factor of water (Wilke–Chang)	-	
φ	Wetting efficiency	-	
Ø	Reactor diameter	m	
A_{μ}, B_{μ}, \dots	Constants of viscosity correlation	(Sifontes Herrera et al.,	
μ', - μ', · · ·]		2016b)	
	Constans of density correlation	(Sifontes Herrera et al.,	
$A_{\rho}, B_{\rho}, \ldots$	Constant of donaity correlation		

Abbreviation/Term	Definition
ADM	Axial-Dispersion Model
CI	Confidence Interval
G-L	Gas–Liquid
L-S	Liquid–Solid
NTP	Normal temperature and pressure: 293.15 K and 101.325 kPa
PFR	Plug-Flow Reactor
RTD	Residence Time Distribution

Electronic Supporting information

Kinetic and Transport Modelling of Continuous Xylose Hydrogenation on Ru/C Solid Foam Catalysts

German Araujo-Barahona^{1,2}, Maria Ciaramella^{1,3}, Miriam Cavaliere^{1,3}, Guillaume Bricault^{1,4}, Kari Eränen¹ Juan García-Serna², Vincenzo Russo³, Dmitry Yu. Murzin¹, Tapio Salmi^{1,3}

¹ Laboratory of Industrial Chemistry and Reaction Engineering (TKR), Johan Gadolin Process

Chemistry Centre (PCC), Åbo Akademi University, FI-20500 Turku/Åbo Finland

² Grupo de Tecnologías a Presión (PressTech), Instituto de Bioeconomía de la Universidad de Valladolid (BioEcoUVa), Departamento de Ingeniería Química y Tecnología del Medio Ambiente, Escuela de Ingenierías Industriales, Universidad de Valladolid.

³ Chemical Sciences Department, Università di Napoli "Federico II", Complesso Universitario Monte S.

Angelo, IT-80126, Napoli, Italy

⁴Université de Poitiers, CNRS UMR7285, Institut de Chimie des Milieux et Matériaux de Poitiers, B27, TSA 51106, 4 rue Michel Brunet, 86073 Poitiers Cedex 9, France

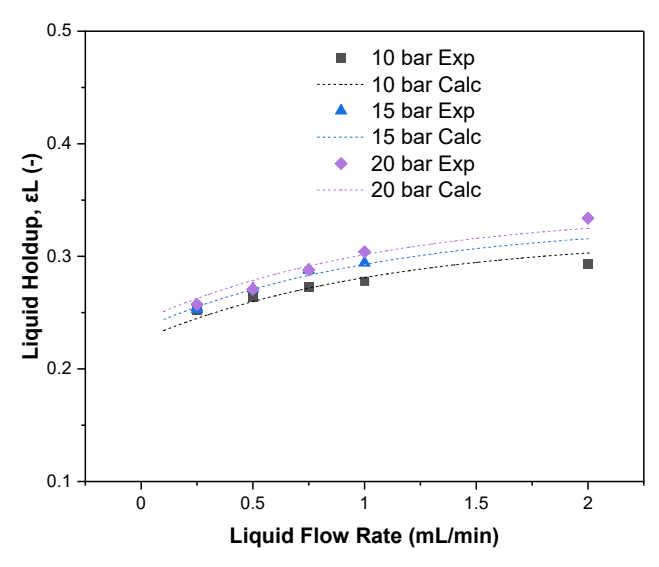


Figure S1. Effect of pressure on liquid holdup on foam bed at 90 °C under 100 mL/min He, NTP.

Published Articles

ARTICLE I

Araujo-Barahona, G., Eränen, K., Oña, J. P., Murzin, D.Y., García-Serna, J., & Salmi, T. (2022). Solid Foam Ru/C Catalysts for Sugar Hydrogenation to Sugar Alcohols— Preparation, Characterization, Activity, and Selectivity. Industrial & Engineering Chemistry Research, 61(7), 2734-2747. DOI: https://doi.org/10.1021/acs.iecr.1c04501.

Abstract

Sugar alcohols are obtained by hydrogenation of sugars in the presence of ruthenium catalysts. The research effort was focused on the development of solid foam catalysts based on ruthenium nanoparticles supported on active carbon. This catalyst was used in kinetic experiments on the hydrogenation of l-arabinose and d-galactose at three temperatures (90, 100, and 120 °C) and two hydrogen pressures (20 and 40 bar). Kinetic experiments were carried out with binary sugar mixtures at different d-galactose-to-l-arabinose molar ratios to study the interactions of these sugars in the presence of the prepared solid foam catalyst. The solid foam catalyst preparation comprised the following steps: cutting of the open-cell foam aluminum pieces, anodic oxidation pretreatment, carbon coating, acid pretreatment, ruthenium incorporation, and ex situ reduction. The carbon coating method comprised the polymerization of furfuryl alcohol, followed by a pyrolysis process and activation with oxygen. Incorporation of ruthenium on the carbon-coated foam was done by incipient wetness impregnation (IWI), using ruthenium(III) nitrosyl nitrate as the precursor. By applying IWI, it was possible to prepare an active catalyst with a ruthenium load of 1.12 wt %, which gave a high conversion of the sugars to the corresponding sugar alcohols. The catalysts were characterized by SEM, HR-TEM, TPR, and ICP-OES to interpret the catalyst behavior in terms of activity, durability, and critical parameters for the catalyst preparation. Extensive kinetic experiments were carried out in an isothermal laboratory-scale semibatch reactor to which gaseous hydrogen was constantly added. High selectivities toward the sugar alcohols, arabitol and galactitol, exceeding 98% were obtained for both sugars, and the sugar conversions were within the range of 53-97%, depending on temperature. The temperature effect on the reaction rate was very strong, while the effect of hydrogen pressure was minor. Regarding the sugar mixtures, in general, l-arabinose presented a higher reaction rate, and an acceleration of the hydrogenation process was observed for both sugars as the ratio of d-galactose to l-arabinose increased, evidently because of competitive interactions on the catalyst surface.

ARTICLE II

Araujo-Barahona, G., Eränen, K., Murzin, D.Y., García-Serna, J., & Salmi, T. (2022). Reaction mechanism and intrinsic kinetics of sugar hydrogenation to sugar alcohols on solid foam Ru/C catalysts–From arabinose and galactose to arabitol and galactitol. Chemical Engineering Science, 254, 117627. DOI: https://doi.org/10.1016/j.ces.2022.117627.

Abstract

Solid foam catalysts have two great benefits: thin catalyst layers guaranteeing a high effectiveness factor and a low pressure drop in continuous operation. The ability of ruthenium-based solid foam catalysts in the hydrogenation of monomeric sugars was illustrated with extensive experiments of L-arabinose and D-galactose hydrogenation at 90-120°C and 20 bar hydrogen pressure. Kinetic experiments were carried out with individual sugars and binary sugar mixtures at different D-galactose-to-L-arabinose molar ratios to reveal the molecular interactions in the presence of the solid foam catalyst. High conversion of sugars and high selectivity to sugar alcohols were achieved in the isothermal and isobaric laboratory-scale reactor which operated under intrinsic kinetic control.

The sugar hydrogenation process was considered from a viewpoint of elementary steps on the catalyst surface. By assuming plausible surface reaction mechanisms, it was possible to derive rate equations for the formation of sugar alcohols, both in case of individual sugars and binary sugar mixtures. The kinetic model based on the non-competitive adsorption of sugars and hydrogen on the ruthenium surface gave a very good description of the hydrogenation kinetics and product distribution on the solid foam catalysts.

The work opens a perspective to the selective and very effective hydrogenation of several sugars to valuable sugar alcohols in the presence of open foam Ru/C catalysts, both in batch and continuous operation modes.

ARTICLE III

Araujo-Barahona, G., Goicoechea-Torres, A., Eränen, K., Latonen, R. M., Tirri, T., Smeds, A., Murzin, D.Y., García-Serna, J., & Salmi, T. (2023). Kinetic studies of solid foam catalysts for the production of sugar alcohols: Xylitol from biomass resources. Chemical Engineering Science, 281, 119130. DOI: https://doi.org/10.1016/j.ces.2023.119130.

Abstract

Structured catalysts, such as solid foams, represent a very promising technology for continuous and stable production of high-value compounds derived from biomass, traditionally produced with batch and semibatch technologies using suspended catalysts. However, the synthesis of structured catalysts presents additional challenges related to their structure and the generation of porous coatings with suitable properties for dispersing the catalytically active phase on the support.

This work was focused on synthesizing a Ru/C solid foam catalyst and investigating its activity in the selective hydrogenation of xylose to xylitol under different operational conditions. The carbon coating, the key step of preparation, was based on the formation and pyrolysis of poly(furfuryl alcohol) in the presence of different amounts of poly(ethylene glycol) (PEG; M=8 kDa) as a pore former, which enabled tuning the support porosity. Thus, the catalyst prepared with 5 wt% PEG presented a micro-to-mesopores volume ratio of 1, and a good dispersion of Ru nanoparticles, as well as a better stability compared to the catalyst prepared without PEG.

The extensive kinetic data collected in this work were mathematically modelled using three different approaches to elucidate the reactant adsorption mode: a non-competitive adsorption model, a non-competitive adsorption model considering the effect of temperature, and a semi-competitive adsorption model. The non-competitive temperature-dependent model displayed better performance in terms of fitting and reliability of the estimated parameters and predicted the adsorption of xylose as an endothermic process. On the other hand, the semi-competitive model gave similar results in terms of fitting and a value for the competitiveness factor of 0.74, which matches the hypothesis that the larger molecules, sugars, can occupy most of the active sites, while some interstitial sites remain accessible for hydrogen adsorption. The modelling results revealed a complex mode of sugar adsorption on the catalyst surface. This modelling concept can be applied to any system in which the molecule sizes are very different.

ARTICLE IV

Araujo-Barahona, G., Shcherban, N., Eränen, K., Kopa, I., Bezverkhyy, I., Martínez-Klimov, M., Vajglová, Z., Aho, A., García-Serna, J., Salmi, T., & Murzin, D. Y. (2024). Ruthenium supported on silicate and aluminosilicate mesoporous materials applied to selective sugar hydrogenation: Xylose to xylitol. Chemical Engineering Journal, 485, 150019. DOI: https://doi.org/10.1016/j.cej.2024.150019.

Abstract

A series of ruthenium-based catalysts supported on a set of silicate and aluminosilicate mesoporous molecular sieves was synthesized and tested in xylose hydrogenation. The materials were characterized in terms of morphology, textural properties, acidity, as well as ruthenium loading, dispersion, and oxidation state. In general, the aluminosilicates-based catalysts displayed a higher activity compared to their respective silicate supports, which can be ascribed to a higher Ru content and dispersion, enhanced by a higher acidity. The most active synthesized catalyst (Ru/Al-MCM-4) displayed an improved performance compared to a commercial Ru/C catalyst due to a better xylitol selectivity. Two modelling approaches were implemented to describe the kinetic rate. The first model was based on the hypothesis that xylose molecules and hydrogen are adsorbed in different active sites on the catalyst surface, while the second model supposes the formation of an intermediate on the catalyst surface that reacts to form xylitol. Both models gave a very good description of the experimental data.

ARTICLE V

Salmi, T., **Araujo-Barahona, G.**, Najarnezhadmashhadi, A., Braz, C., Goicoechea-Torres, A., Ciaramella, M., Ares, M., Russo, V., García-Serna, J., Eränen, K., Wärnå, J., Matos, H. & Murzin, D. Y. (2024). Process Intensification via Structured Catalysts: Production of Sugar Alcohols. Chemie Ingenieur Technik, 96(12), 1642-1656. DOI: https://doi.org/10.1002/cite.202400087.

Abstract

With the aid of structured catalysts and reactors, such as monoliths, solid foams, and 3D printed structures, the limitations of conventional slurry and packed-bed reactors can be surmounted. Multiphase mathematical models were presented for solid foam structures and the models were verified for the hydrogenation of arabinose, galactose, and xylose to the corresponding sugar alcohols. High product selectivities were obtained in batch and continuous experiments. Three kinetic models were considered: a competitive adsorption model, a semi-competitive adsorption model as well as a non-competitive adsorption model for sugar monomers and hydrogen. The models gave a good reproduction of the data, but the semi-competitive adsorption model was the most plausible one because of the size difference between adsorbed sugar and hydrogen molecules.

ARTICLE VI

Araujo-Barahona, G., De Simone, M., Brunberg, C., Eränen, K., Reinsdorf, A., Roos, M., García-Serna, J., Russo, V., Murzin, D. Y., Salmi, T. Solid Raney-type Ni Foam Catalysts for Xylitol Production: Continuous and Batch Operation. Applied Catalysis A: General, 701, 120324. DOI: https://doi.org/10.1016/j.apcata.2025.120324.

Abstract

Solid activated metal foam catalysts represent a promising alternative for the continuous production of valuable sugar alcohols. Traditionally, sugar alcohols are produced industrially in batch mode using finely dispersed Raney-type nickel catalysts. In this study, novel solid foam Raney-type Ni catalysts (activated metal foam catalysts) were used for the hydrogenation of xylose to xylitol in both batch and continuous operation. Two types of catalysts were investigated: Raney-type Ni foam (Metalyst® MC 911 by Evonik Operations GmbH, Ev-F-Ni) and Raney-type Ni foam promoted with molybdenum (Metalyst® MC 981 by Evonik Operations GmbH, Ev-F-NiMo). Catalyst deactivation was primarily attributed to the accumulation of strongly adsorbed organic species on the active sites and to Ni and Al leaching, which reduced the availability of catalytically active sites. Ev-F-NiMo demonstrated a superior stability and activity compared to Ev-F-Ni, attributed to electronic interactions between Mo and Ni, which stabilize Ni in a lower oxidation state and reduce metal leaching under reaction conditions. In continuous operation, the catalysts exhibited reduced deactivation, likely due to enhanced desorption of poisons under the continuous flow of fresh feed. Although the exposure to xylonic acid, a potential poison forming on the catalyst surface, temporarily reduced the xylitol yield in continuous mode, the Ev-F-NiMo catalyst demonstrated good resilience, recovering its activity after the removal of the poisoning species. These results highlight the very attractive technical solution for the continuous production of sugar alcohols from sugar monomers, utilizing promoted Raney-type Ni catalyst that is highly active, selective and cost-effective.